



*Ministero dell'Istruzione,
dell'Università e della Ricerca*



DIPARTIMENTO DI INGEGNERIA CIVILE

***Dottorato di Ricerca in Ingegneria delle Strutture e del
Recupero Edilizio e Urbano***

XIII Ciclo N.S. (2012-2014)

**ON THE MECHANICAL MODELING AND THE
OPTIMAL DESIGN OF TENSEGRITY STRUCTURES**

Gerardo Carpentieri

Il Tutor

Prof. Fernando Fraternali

Il Coordinatore

Prof. Ciro Faella

Co-Tutor

***Prof. Robert E. Skelton
(UCSD – San Diego)***

Abstract

In this thesis, we investigate the use of the most fundamental elements; cables for tension and bars for compression, in the search for the most efficient bridges. Stable arrangements of these elements are called tensegrity structures. We show herein the minimal mass arrangement of these basic elements to satisfy both yielding and buckling constraints. We show that the minimal mass solution for a simply-supported bridge subject to buckling constraints matches Michell's 1904 paper which treats the case of only yield constraints, even though our boundary conditions differ. The necessary and sufficient condition is given for the minimal mass bridge to lie totally above (or below) deck. Furthermore this condition depends only on material properties. If one ignores joint mass, and considers only bridges above deck level, the optimal complexity (number of elements in the bridge) tends toward infinity (producing a material continuum). If joint mass is considered then the optimal complexity is finite. The optimal (minimal mass) bridge below deck has the smallest possible complexity (and therefore cheaper to build), and under reasonable material choices, yields the smallest mass bridge.

We also study a design for a minimal mass, deployable support structure for a solar panel covering of water canals. The results are based upon the minimal mass properties of tensegrity structures. The efficient structure is a tensegrity system which has an optimal complexity for minimal mass. This optimal complexity is derived in this thesis, along with deployable schemes which are useful for construction, repairs, for sun following, and for servicing. It is shown that the minimal structure naturally has deployable features so that extra mass is not needed to add the multifunctional features. The design of bridge structures with tensegrity architecture will show an optimal complexity depending only on material choices and external loads. The minimization problem considers a distributed load (from weight of solar panels and wind loads), subject to buckling and yield constraints. The result is shown to be a Class 1 Tensegrity *substructure* (support structure only below the deck).

These structures, composed of axially-loaded members (tension and compressive elements), can be easily deployable and have many portable applications for small spans, or they can be easily assembled for prefabricated component parts for large spans. The focus of this work is an application of these minimal mass tensegrity concepts to design shading devices to prevent or reduce evaporation loss, while generating electric power with solar panels as the cover.

While the economics of the proposed designs are far from finalized, this document shows a technical solution that uses the smallest material resources, and shows the technical feasibility of the concept.

Moreover, we formulate and discuss the relationship between polyhedral stress functions and tensegrity structures in 2D, and a two-mesh technique for the prediction of the stress field associated with such systems. We generalize classical results concerned with smooth Airy stress functions to polyhedral functions associated with arbitrary triangulations of a simply-connected domain. We also formulate a regularization technique that smoothly projects the stress function corresponding to an unstructured force network over a structured triangulation. The thesis includes numerical examples dealing with a benchmark problem of plane elasticity, and the stress fields associated with tensegrity models of a cantilever beam and an arch bridge.

Keywords

Tensegrity structures, form-finding, minimum mass, bridges, parametric design, multiscale complexity, force networks, polyhedral stress functions, Cauchy stress.

Publications

The research work carried out by the candidate during his Ph.D. career originated a collection of publications related to subjects of the mechanics of solids and structures. Such publications related to the present thesis work and other publications, as specified in what follows.

Publications related to the presente thesis work

Refereed Journal Articles

- (P1) R.E. Skelton, F. Fraternali, G. Carpentieri, A. Micheletti, Minimum mass design of tensegrity bridges with parametric architecture and multiscale complexity, *Mechanics Research Communications*, Volume 58, June 2014, Pages 124-132, ISSN 0093-6413, <http://dx.doi.org/10.1016/j.mechrescom.2013.10.017>.
- (P2) F. Fraternali, I. Farina, G. Carpentieri, A discrete-to-continuum approach to the curvatures of membrane networks and parametric surfaces, *Mechanics Research Communications*, Volume 56, March 2014, Pages 18-25, ISSN 0093-6413, <http://dx.doi.org/10.1016/j.mechrescom.2013.10.015>.
- (P3) A. Amendola, G. Carpentieri, M. de Oliveira, R.E. Skelton, F. Fraternali, Experimental investigation of the softening-stiffening response of tensegrity prisms under compressive loading, *Composite Structures*, Volume 117, November 2014, Pages 234-243, ISSN 0263-8223, <http://dx.doi.org/10.1016/j.compstruct.2014.06.022>.
- (P4) F. Fraternali, G. Carpentieri, A. Amendola, On the mechanical modeling of the extreme softening/stiffening response of axially loaded tensegrity prisms, *Journal of the Mechanics and Physics of Solids*, Volume 74, January 2015, Pages 136-157, ISSN 0022-5096, <http://dx.doi.org/10.1016/j.jmps.2014.10.010>.

-
- (P5) F. Fraternali, G. Carpentieri, On the correspondence between 2D force networks, tensegrity structures and polyhedral stress functions, *International Journal of Space Structures*, Volume 29, October 2014, Pages 145-159, ISSN 0266-3511.
- (P6) G. Carpentieri, R.E. Skelton, F. Fraternali, Minimum Mass and Optimal Complexity of Tensegrity Bridges, *Cable Structures: Dynamics, Control, and Monitoring*. Manuscript ID: 857128. In review.
- (P7) G. Carpentieri, R.E. Skelton, F. Fraternali, A Minimal Mass Deployable Structure for Solar Energy Harvesting on Water Canals. In press.

Refereed Conferences Proceedings

- (C1) F. Fraternali, G. Carpentieri, R.E. Skelton, A. Micheletti, Architetture tensegrity parametriche per ponti di massa minima, (In italian), XXIV C.T.A. Congress "The Italians steel days", September 30th, 2013, October 2nd, 2013, Turin (Italy). Volume: 2, Pages: 890-897. ISBN: 978-88-905870-0-9.

Book Chapters

- (B1) G. Carpentieri, F. Fraternali, A. Micheletti, R.E. Skelton, Ottimizzazione di architetture parametriche per strutture tensegrity, (In italian), in: *Sulla Ricerca di Forma delle Strutture*, F. Fraternali, G. Rocchetta. Department of Civil Engineer, University of Salerno, (In Italian).
- (B2) G. Carpentieri, R.E. Skelton, F. Fraternali, Analytic aspects of the parametric design of minimal mass tensegrity bridges, in: *Sulla Ricerca di Forma delle Strutture*, F. Fraternali, G. Rocchetta. Department of Civil Engineer, University of Salerno.

Internal Reports

- (R1) G. Carpentieri, R.E. Skelton, F. Fraternali, Parametric design of minimal mass tensegrity bridges under yielding and buckling constraints, 2014. Eprint: arXiv: 1411.7966 [cond-mat.mtrl-sci].

Other Publications in Refereed Journal Articles

- (O1) F. Fraternali, B. Palazzo, G. Carpentieri, Multiaxial prestress of reinforced concrete I-beams, *International Journal of Earthquake Engineering*, Volume 1, January 2014, Pages 17-30, ISSN 0393-1420.
- (O2) G. Carpentieri, F. Tornabene, L. Ascione, F. Fraternali, An accurate one-dimensional theory for the dynamics of laminated composite curved beams, *Journal of Sound and Vibration*, Volume 336, 3 February 2015, Pages 96-105, ISSN 0022-460X, <http://dx.doi.org/10.1016/j.jsv.2014.09.041>.
- (O3) F. Fraternali, G. Carpentieri, A. Amendola, R.E. Skelton, V.F. Nesterenko, Multiscale tunability of solitary wave dynamics in tensegrity metamaterials, *Applied Physics Letters*, Volume 105, November 2014, Pages 201903, ISSN 0003-6951 , <http://dx.doi.org/10.1063/1.4902071>.



To my Family

Acknowledgement

The author wishes to thank:

Fernando Fraternali (University of Salerno),

Robert E. Skelton (University of California San Diego),

Vitali Nesterenko, Mauricio de Oliveira, Gianmario Benzoni (University of California San Diego),

Paul Anzel, Chiara Daraio, Marc Serra Garcia, Ludovica Lattanzi, Mythili Ramathasan, Thevamaran Ramathasan (Caltech, Pasadena and ETH, Zurich),

Francesce Tornabene, Fabrizio Carpentieri (Alma Mater Studiorum, University of Bologna),

Ada Amendola, Maurizio Angelillo, Francesco Ascione, Luigi Ascione, Salvatore Barba, Bruno Bisceglie, Paolo Castaldo, Rosaria Chechile, Vincenzo Ciancia, Rino Conte, Pierpaolo D'Agostino, Giuseppe Damone, Antonio D'Imperio, Elena De Chiara, Annalisa Di Palma, Giuseppe Di Palma, Angelo Esposito, Ciro Faella, Ilenia Farina, Luciano Feo, Antonio Fortunato, Alessandro Graziano, Antonella Iannaccone, Luciana Iannaccone, Massimo Latour, Carmine Lima, Geminiano Mancusi, Enzo Martinelli, Rosario Montuori, Elide Nastri, Bruno Palazzo, Rosa Penna, Marco Pepe, Giuseppe Rocchetta, Cristian Santomauro, Lucia Senatore, Saverio Spadea, Lucia Taglianetti, Paolo Villani (University of Salerno)

for their precious advices, collaboration, support and solidarity during the course of the present work.

Thanks you all, Grazie mille!

Contents

List of Figures	xiv
List of Tables	xxii
1 Motivation and Background	1
1.1 On the Historical Evolution of Bridges	2
1.2 Basic Notions of Tensegrity Structures	6
1.3 Tensegrity Bridges	9
1.4 Research Goals	12
2 Analytic Results on the Optimal Design of Tensegrity Bridges	15
2.1 Introduction	16
2.2 Properties of Tensile and Compressive Components of the Tensegrity Structure	17
2.3 Planar Topologies of the Tensegrity Bridges Under Study	19
2.4 Analysis of the Basic Modules ($n = 1, p = 1$ or $0, q = 1$ or 0)	21
2.4.1 Nominal Bridges under Yielding Constraints	26
2.4.2 Nominal Bridges under Buckling Constraints	32
2.5 Mass of Bridges of Complexity $(n, p, q) = (1, p, q)$, Under Yielding and Buckling Constraints	39
2.5.1 <i>Superstructure</i> Bridge with Complexity $(n, p, q) = (1, 0, q > 1)$	40

CONTENTS

2.5.2	<i>Substructure</i> Bridge with Complexity $(n, p, q) = (1, p > 1, 0)$	46
2.6	Mass of Bridges of Complexity $(n, p, q) = (n, 1 \text{ or } 0, 1 \text{ or } 0)$	50
2.6.1	<i>Substructure</i> Bridge with Complexity $(n, p, q) = (n, 1, 0)$	51
2.6.2	<i>Superstructure</i> Bridge with Complexity $(n, p, q) = (n, 0, 1)$	57
2.7	Introducing Deck and Joint Masses	62
2.7.1	Including Deck Mass	62
2.7.2	Adding Deck Mass for A <i>Substructure</i> Bridge with Complexity $(n, p, q) = (n, 1, 0)$	64
2.7.3	Adding Deck Mass for A <i>Superstructure</i> Bridge with Complexity $(n, p, q) = (n, 0, 1)$	69
2.7.4	Penalizing Complexity with cost considerations: Adding Joint Mass	74
2.8	Discussion of the results	76
3	Numerical Results on the Optimal Design of Tensegrity Bridges	79
3.1	Introduction	80
3.2	First bridge model without deck	80
3.2.1	Mass minimization algorithm	83
3.2.2	Numerical results	88
3.2.3	Minimum mass design for $n = 1$, and variable p , α , and β	89
3.2.3.1	Minimum mass design for variable n , p , α , and β	90
3.2.3.2	Minimum mass design for $n = 5$, $\alpha = 40$ deg, $\beta = 60$ deg, and variable p	94
3.3	Second bridge model without deck	95
3.3.1	Nominal Bridges	99
3.3.2	Substructures	102
3.3.3	Superstructures	106
3.4	Bridge model with deck	109

CONTENTS

3.4.1	Substructures	110
3.4.2	Superstructures	110
3.5	Bridge constrained with a fixed hinge and rolling hinge (<i>HR</i>)	113
3.6	Discussion	115
4	Optimal Design of Solar Energy Harvesting Bridge Structures	120
4.1	Introduction	121
4.2	Description of the Model	123
4.3	Description of the Deployment Scheme	124
4.4	Analytical Results	131
4.5	Numerical Results	135
4.5.1	Minimal Mass Design	135
4.6	Remarks	138
5	On the Continuum Limits of Tensegrity Structures	140
5.1	Introduction	141
5.2	Internally self-equilibrated tensegrity structures and polyhedral stress functions	143
5.2.1	Internally self-equilibrated framework associated with a given polyhedral stress function	143
5.2.2	Polyhedral stress function associated with a given, internally self-equilibrated framework	147
5.3	Stress field associated with a tensegrity structure	149
5.4	Numerical results	152
5.4.1	Convergence Study	152
5.4.2	Cantilever Tensegrity Structure	154
5.4.3	Tensegrity bridges	159
5.5	Discussion	165
6	Concluding Remarks and Future Work	167
7	Appendix	170

CONTENTS

Bibliography

175

List of Figures

1.1	Some examples of ancient roman bridges: (a) Tiberius bridge, Rimini, Italy; (b) Alcántara bridge, Spain; (c) Fabricio bridge on Tiver river, Rome, Italy; (d) Roman bridge in Chaves, Portugal. Source: (www.wikipedia.it).	2
1.2	Examples of arch bridges with above deck road: (a) viaduct on Merizzano river, Autostrada del Sole, Italy; (b) bridge on Fiumarella river, Catanzaro, Italy; (c) Paderno bridge, Italy; (d) Blera bridge, Italy. Source: [8].	3
1.3	Examples of suspended bridges (a-b) and cable-stayed bridges (c-d): (a) Golden Gate, San Francisco, United States; (b) Akashi Kaikyo bridge, Kobe, Japan; (c) Rion Antirion bridge, Greece; (d) Polcevera viaduct, Geneve, Italy. Source: (www.wikipedia.it).	4
1.4	Collapse of the Takoma bridge, USA, 1940 (total span 1810.2 m): (a-c) views of the suspended deck under big deformations due to the resonance under wind load; (d) failure of the bridge. Source: (www.wikipedia.it).	5
1.5	Examples of beam bridges (a-b) and truss bridges (c-d): (a) Pistoletsa viaduct, Mosso, Italy; (b) Costanzo bridge on the Irminio river, Italy; (c) truss bridge in Ivrea, Italy; (d) truss bridge on Po river, Italy. Source: (www.wikipedia.it).	6

LIST OF FIGURES

1.6	Illustration of some basic building blocks of tensegrity structures: (a): minimal tensegrity prism; (b): tensile unit, (c) T-bar unit; (d) D-bar unit; (e): Michell truss; (f) cylindrical unit; (g) bridge unit. Source: ([141, 136, 137]).	7
1.7	Presentation of a concept for tensegrity bridge in London. Source: (Boeck, 2013, p. 19, [1]).	9
1.8	Bridge in Purmerend. Source: (Boeck, 2013, p. 19, [1]).	10
1.9	Tor Vergata footbridge: a), b) Two views of the footbridge module, c) Side view of the footbridge structure. Source: (Micheletti, 2012, p. 5, 10, [2])	10
1.10	Kurilpa bridge. Source: (http://tensegrity.wikispaces.com/Kurilpa + Bridge)	11
1.11	Tensegrity "hollow rope" pedestrian bridge. Source: (Barbarigos et al., 2010, p. 1159, [11])	11
1.12	Tensegrity footbridge with an arch deck. Source: (Briseghella et al., 2010, p. 288, [5])	12
1.13	Jan De Boeck's tensegrity bridge: a) Front view of a rotated model of a 3 strut tensegrity module, b) Sketch illustrating how a 3 strut tensegrity module is multiplied and connected to a bridge like structure. Source: (Jan De Boeck, 2013, p. 65, 67, [1])	12
1.14	Suspended Tensegrity Bridge: a) Vertical cross section, b) Model of two tensegrity modules, c) Sketch illustrating the whole tensegrity bridge. Source: (http://tensegrity.wikispaces.com/Suspended + Bridge + by + Paradiso)	13
1.15	Tim Tyler's conceptual project for a twisting hexagonal bridge: a), b) Different views of the model. Source: (http://hexdome.com/bridges)	13
2.1	Adopted notation for bars and cables of a tensegrity system.	21

LIST OF FIGURES

2.2 Basic modules of the tensegrity bridge with: a) nominal bridge: $n = q = p = 1$; b) superstructure: $n = q = 1$; c) substructure: $n = p = 1$ 22

2.3 Exemplary geometries of the nominal bridges for different values of the complexity parameters n (increasing downward) and q (increasing leftward). 23

2.4 Exemplary geometries of the substructures for different values of the complexity parameters n (increasing downward) and p (increasing leftward). 24

2.5 Exemplary geometries of the superstructures for different values of the complexity parameters n (increasing downward) and q (increasing leftward). 25

2.6 Dimensionless masses of the substructure (continuous curves) and superstructure (dashed curves) for different values of the aspect angles (respectively β or α) and for values of the coefficient $\varrho > 1$ (left) and $\varrho < 1$ (right) under yielding constraints. 29

2.7 Mass $\mu_B(t_1, t_2)$ (Eq. 2.47) for different values of the aspect angles β assuming steel bars and cables, $F = 1\text{ N}$, $L = 1\text{ m}$ ($\eta = 857.71$), $t_1 = 0$ and $t_2 = 0$. The minimum value is $\mu_B^* = 5.0574$ at $\beta_B^* = 4.25\text{ deg}$ 34

2.8 Dimensionless masses of the substructure (left) and superstructure (right) under buckling constraints for different values of the aspect angles (respectively β or α) and different values of the parameter η 37

2.9 Contour plots of the functions $\bar{\eta}_{\alpha\beta}$, (left, Eq. 2.64) and $\eta_{\alpha\beta}$, (right, Eq. 2.65) for different values of the aspect angles α and β 39

2.10 Notations for forces and lengths of bars and cables for a *superstructure* with complexity $n = 1$ and $q > 1$ 40

LIST OF FIGURES

2.11 Optimal topologies of *superstructure* bridges with complexity $(n, p, q) = (1, 0, q \rightarrow \infty)$ under yielding constraints (left) and buckling constraints (right) for different q , (steel for bars and cables, $F = 1 N, L = 1 m$). 41

2.12 Mass curves under yielding constraints of *substructures* (left) and *superstructures* (right) vs. aspect angle β (left) and α (right) for different complexity p (left) and q (right), ($F = 1 N, L = 1 m$). 42

2.13 Mass curves under buckling constraints of *substructures* (left) and *superstructures* (right) vs. aspect angle β (left) and α (right) for different complexity p (left) and q (right), (steel bars and cables, $F = 1 N, L = 1 m$). 43

2.14 Notations for forces and lengths of bars and cables for a *substructure* with complexity $n = 1$ and $p > 1$ 44

2.15 Optimal topologies of *substructure* bridges with $n = 1$ under yielding constraints (left) and buckling constraints (right) for different p , (steel for bars and cables, $F = 1 N, L = 1 m$). 46

2.16 Minimal mass bridges under (a) yielding constrained *nominal* bridges, (b) buckling constrained *superstructure* bridge and (c) buckling constrained *substructure* bridge. 50

2.17 Adopted notations for forces and lengths of bars and cables for a substructure with generic complexity n and $p = 1$ 51

2.18 Adopted notations for forces and lengths of bars and cables for a *superstructure* with complexity $(n, p) = (n, 1)$ 51

2.19 a) schematic deck system for a *substructure* with complexity $n = 3$ and $p = 1$. b) detail of a single deck module. 63

2.20 Optimal masses under yielding of the *substructures* (left) and *superstructure* (right) without deck (solid curves) and with deck (dashed curves) for different values of the complexity n and for different values of ρ , ($F = 1 N, w_d = 1 m$, steel deck). 69

LIST OF FIGURES

2.21	Optimal masses under buckling of the <i>substructures</i> (left) and <i>superstructure</i> (right) without deck (solid curves) and with deck (dashed curves) for different values of the complexity n and for different values of η , ($F = 1$ N, $L = w_d = 1$ m, steel deck).	70
2.22	Optimal masses under yielding of the substructures (left) and superstructure (right) (red curve) and total optimal mass with deck and different joint factors (dashed and dotted curves) for different values of the complexity n (steel for bars, cables, deck, $F = 1$ N, $L = w_d = 1$ m).	74
2.23	Optimal masses under buckling of the substructures (left) and superstructure (right) (red curves) and total optimal masses with deck and different joint factors (dashed and dotted curves) for different values of the complexity n (steel for bars, cables, deck, $F = 1$ N, $L = w_d = 1$ m).	75
3.1	Michell frames for a centrally loaded beam.	83
3.2	Basic module of the tensegrity bridge ($n = 1$, $p = 1$).	83
3.3	Exemplary geometries of the tensegrity bridge for different values of the complexity parameters n and $p = q$	84
3.4	Optimal bridge topologies under combined yielding and buckling constraints, for $n = 1$, $\alpha \in (0, 90)$ deg, $\beta \in (0, 90)$ deg, and $p \in [1, 50]$	95
3.5	Optimal topologies under yielding constraints (left) and combined yielding and buckling constraints (right) for different values of n and $p = 1$	96
3.6	Optimal topologies under combined yielding and buckling constraints for different values of n , $p = 3$ (left), and $p = 7$ (right).	97
3.7	Optimal topologies under buckling constraints for $n = 5$, fixed angles $\alpha = 40$ deg and $\beta = 60$ deg, and different values of p	98

LIST OF FIGURES

3.8 Total masses ($\mu_{B,tot}^*$, black curves) for different values of the joint factor Ω and structural masses ($\mu_{B,S}^*$, red curves) under buckling constraints for $p = q = 1$ and different n 112

3.9 Total masses ($\mu_{B,tot}^*$, black curves) for different values of the joint factor Ω and structural masses ($\mu_{B,s}^*$, red curve) under buckling constraints for $n = 5$ vs q for superstructure. 115

4.1 Different configurations of a deployable solar roof for water canals: (a) open onfiguration, (b) transition between open/closed configurations, (c) closed configuration. 126

4.2 Adopted notations for forces and lengths of bars and cables for a substructure with generic complexity $(n, p, q) = (n, 1, 0)$ 126

4.3 Schematic of a deployable tensegrity system with solar panel. 127

4.4 Exemplary geometries of the substructures for different values of the complexity parameters n (increasing downward) and p (increasing leftward). 128

4.5 Details of the canal structure: (a) deck system, (b) deformed shape of the deck cross cables subjected to the solar panel force. 130

4.6 Dimensionless mass μ_B (4.27) vs. aspect angle β_B for: solution with steel bars and cables (left, $\eta = 238.65$), steel bars and Spectra cables (right, $\eta = 7569.04$). 135

4.7 Dimensionless total mass μ_{tot} (4.30) vs. complexity n for: solution with steel bars and cables (left, $\eta = 238.65$), steel bars and Spectra cables (right, $\eta = 7569.04$) and different joint factors Ω . 136

5.1 Illustration of a triangulated force network and the associated polyhedral stress function $\hat{\varphi}_h$ (red: tensile forces, blue: compressive forces). 143

5.2 Details of an inner node (left) and a boundary node (right) of Π_h 144

5.3 2D view of the force network in Fig. 5.1 (red: tensile forces, blue: compressive forces). 148

LIST OF FIGURES

5.4 Illustration of K_n and $\tilde{\Omega}_n$ 151

5.5 Flamant solution for for the problem of a half plane loaded by a perpendicular point load (left), and examined simulation region (right). 153

5.6 Illustrations of selected unstructured (left) and structured (right) force networks approximating the Flamant problem in Fig. 5.5 (blue: compressive forces; red: tensile forces). 155

5.7 Root Mean Square Deviations of the examined approximations to the radial stress $T_{rr}^{(0)}$ of the Flamant problem. 156

5.8 Density plots of the examined approximations to the radial stress $T_{rr}^{(0)}$ of the Flamant problem for different meshes and interpolation schemes. 157

5.9 Michell truss example. Top: ordered (right) and unstructured (left) configurations. Center: details of the force networks near the tip (blue: compressive forces; red: tensile forces). Bottom: Airy stress functions associated with ordered (left) and unstructured (right) force networks. 158

5.10 Density plots of different approximations to the stress components T_{11} (top:longitudinal normal stresses) and T_{12} (bottom:tangential stresses) associated with the Michell truss. . . . 159

5.11 LSM truss example. Top: ordered (left) and unstructured (right) force networks (blue: compressive forces; red: tensile forces). Center and bottom: ordered and unstructured approximations to the stress field of the background domain. 160

5.12 LSM bridge with complexities $n = p = q = 3$: (a) structural scheme, (b) deformed shape, (c) force network. 162

5.13 LSM bridge with complexities $n = p = q = 3$: (a) T_{11} stresses, (b) T_{22} stresses, (c) T_{12} stresses. 163

5.14 LSM bridge with complexities $n = p = q = 5$: (a) structural scheme, (b) deformed shape, (c) force network. 164

LIST OF FIGURES

5.15 LSM bridge with complexities $n = p = q = 5$: (a) T_{11} stresses,
(b) T_{12} stresses. 165

7.1 Illustration of a doubly-connected domain Ω 172

7.2 Subdivision of a a doubly-connected domain Ω into two simply-
connected domains Ω_1 and Ω_2 173

List of Tables

3.1	Selected results for the example in Sect. 3.2.3.	90
3.2	Selected results for the example in Sect. 3.2.3.1.	91
3.3	Selected results for the example in Sect. 3.2.3.2.	92
3.4	Material properties.	99
3.5	Numerical results of nominal bridge with complexities $n = 1$ and different $p = q$ under yielding (Y) and combined yielding and buckling constraints (B), ($F = 1 N$; $L = 1 m$; steel bars and steel strings).	101
3.6	Numerical results of nominal bridges with different complexities n and p under yielding (Y) and combined yielding and buckling constraints (B), ($F = 1 N$; $L = 1 m$; steel bars and steel strings).	103
3.7	Numerical results of substructures with complexities $n = 1$ and different p under yielding (Y) and combined yielding and buck- ling constraints (B), ($F = 1 N$; $L = 1 m$; steel bars and steel cables).	104
3.8	Numerical results of substructures with different complexities n and p under yielding (Y) and combined yielding and buckling constraints (B), ($F = 1 N$; $L = 1 m$; steel bars and steel cables).	105
3.9	Numerical results of superstructures with complexities $n = 1$ and different q under yielding (Y) and combined yielding and buckling constraints (B), ($F = 1 N$; $L = 1 m$; steel bars and steel cables).	107

LIST OF TABLES

3.10 Numerical results of superstructures with different complexities n and p under yielding (Y) and combined yielding and buckling constraints (B), ($F = 1 N$; $L = 1 m$; steel bars and steel cables). 108

3.11 Numerical results of substructures with deck for different complexities n and p under buckling constraints (B), ($F = 450 kN$; $L = 30 m$; $w_d = 3 m$, steel bars and deck, Spectra[®]- UHMWPE cables). 111

3.12 Numerical results of superstructures with deck for different complexities n and q under buckling constraints (B), ($F = 450 kN$; $L = 30 m$; $w_d = 3 m$, steel bars and deck, Spectra[®]- UHMWPE cables). 113

3.13 Numerical results of superstructures with deck for $n = 5$ and different complexities q under buckling constraints (B), ($F = 450 kN$; $L = 30 m$; $w_d = 3 m$, steel bars and deck, Spectra[®]- UHMWPE cables). 114

3.14 Numerical results of nominal bridges constrained with a fixed hinge and a rolling hinge (HR) and with complexities $n = 1$ and different $p = q$ under yielding (Y) and combined yielding and buckling constraints (B), ($F = 1 N$; $L = 1 m$; steel bars and steel cables). 116

3.15 Numerical results of substructures constrained with a fixed hinge and a rolling hinge (HR) with different complexities n and p under yielding (Y) and combined yielding and buckling constraints (B), ($F = 1 N$; $L = 1 m$; steel bars and steel cables). 117

3.16 Numerical results of superstructures constrained with a fixed hinge and a rolling hinge (HR) with different complexities n and q under yielding (Y) and combined yielding and buckling constraints (B), ($F = 1 N$; $L = 1 m$; steel bars and steel cables). 118

4.1 Material properties. 134

LIST OF TABLES

4.2 Optimal masses μ_B^* (4.20) and μ_{tot}^* (4.30) and optimal aspect angles β_B^* (4.21) of *substructure* bridges with steel bars and cables, under combined yielding and buckling constraints (B), for different complexities n 134

4.3 Optimal masses μ_B^* (4.20) and μ_{tot}^* (4.30) and optimal aspect angles β_B^* (4.21) of *substructure* bridges with steel bars and Spectra[®]cables, under combined yielding and buckling constraints (B), for different complexities n 135

4.4 Properties of the members for the minimal mass design of the *substructure* bridge with steel bars and cables and complexity $n = 5$, ($\beta = 7.00$ deg). 137

4.5 Properties of the members for the minimal mass design of the *substructure* bridge with steel bars and Spectra[®]cables and complexity $n = 3$, ($\beta = 2.18$ deg). 138

1

Motivation and Background

1.1 On the Historical Evolution of Bridges

Bridge structures have attracted the interest of Engineers throughout the history because they represent the attempt of men to overcome obstacles. These structures are used wherever there is a river, a canyon or any road. Bridges allow easier connections between two different points and faster displacements of goods and people. In this thesis, we have studied the different typologies and analysis methods of bridge structures that were developed in the history. We also present and compare several ancient and modern exemplars of bridges and we study the most important problems regarding their structures. Then, we develop a new design method that minimizes the total cost of the structure using "tensegrity" structures.

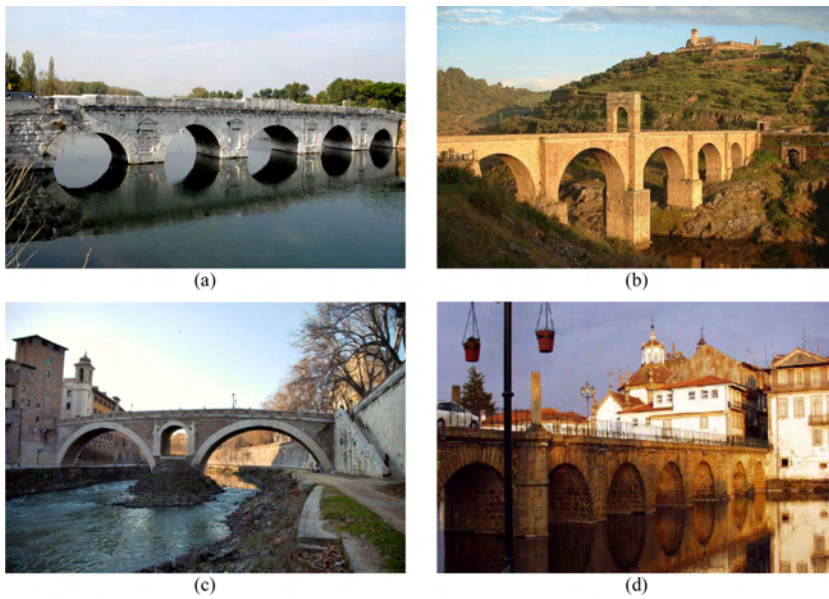


Figure 1.1: Some examples of ancient roman bridges: (a) Tiberius bridge, Rimini, Italy; (b) Alcántara bridge, Spain; (c) Fabricio bridge on Tiver river, Rome, Italy; (d) Roman bridge in Chaves, Portugal. Source: (www.wikipedia.it).

The first bridge structures were made during Greek and Roman periods.

1. MOTIVATION AND BACKGROUND

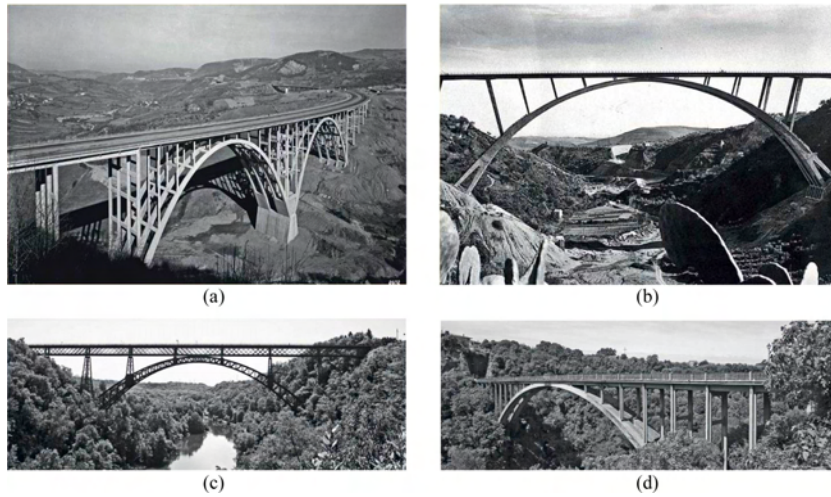


Figure 1.2: Examples of arch bridges with above deck road: (a) viaduct on Merizzano river, Autostrada del Sole, Italy; (b) bridge on Fiumarella river, Catanzaro, Italy; (c) Paderno bridge, Italy; (d) Blera bridge, Italy. Source: [8].

In particular, Romans made wide use of masonry arches. Nowadays, some ancient Roman arch bridges are still in service. Typically those structures serve as roads for goods and people, or as aqueducts for drinking water (see Fig. 1.1). After Roman period there was an improvement of the structural capacity of bridges due to the introduction of fast and heavy vehicles such as trains and cars. Then, the performance of bridges were increased both in terms of load capacity and span and there was a smaller allowable maximum slope of the roads (required by new vehicles). Prestressed concrete, in place of steel, was widely used for bridges in Italy during 20th century because the idea that concrete is a very durable material also without great maintenance (Fig. 1.2). These choices led to build several prestressed concrete bridges which nowadays are often collapsed or seriously damaged [9]. However, prestressed concrete is still widespread in Italy and its technology has been improved a lot. Cable-stayed and suspended bridges are largely used in other countries, such as United States, and they are usually made of steel and allow very big spans (Fig. 1.3). Moreover, suspended bridges required new theories to study the dynamics of such structures. In particular, they can be affected

1. MOTIVATION AND BACKGROUND

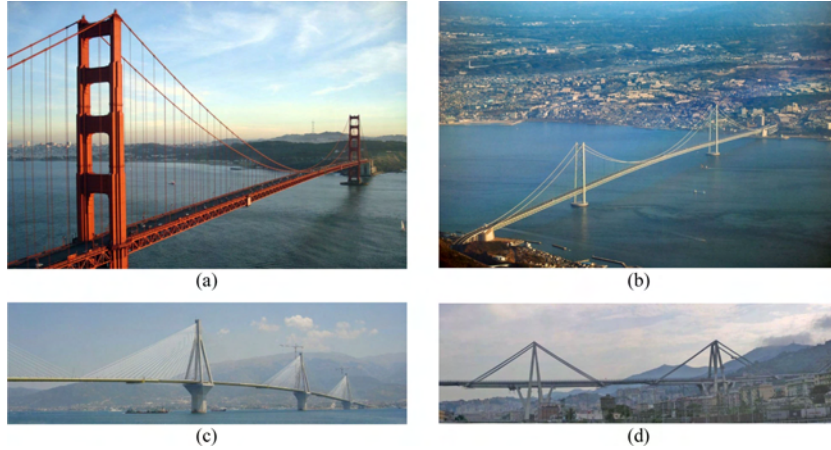


Figure 1.3: Examples of suspended bridges (a-b) and cable-stayed bridges (c-d): (a) Golden Gate, San Francisco, United States; (b) Akashi Kaikyo bridge, Kobe, Japan; (c) Rion Antirion bridge, Greece; (d) Polcevera viaduct, Geneve, Italy. Source: (www.wikipedia.it).

by dynamic instabilities because of their low stiffness, as shown eg. in the famous structural collapse of Takoma bridge (Fig. 1.4). Engineers employed several kinds of bridge structures suited to span obstacles and they are now available powerful computational tools that make possible detailed analysis of such structures, both in statics and dynamics, also investigating possible instabilities (eg. flutter).

The modern design approaches are the result of the experience accrued from the numerous failures of the past (eg. the Takoma bridge, Fig. 1.4). Several theories were developed for different type of bridge structures, from the classic Roman arch bridges to the modern suspended bridges. In particular, from the structural point of view, the following types of bridges can be identified [9, 10]:

- arch bridges: they consist of one or more arch structures, pushing each horizontally at both side; they can allow an above or below deck level (respectively substructure or superstructure) (Fig. 1, Fig. 1.2);

1. MOTIVATION AND BACKGROUND

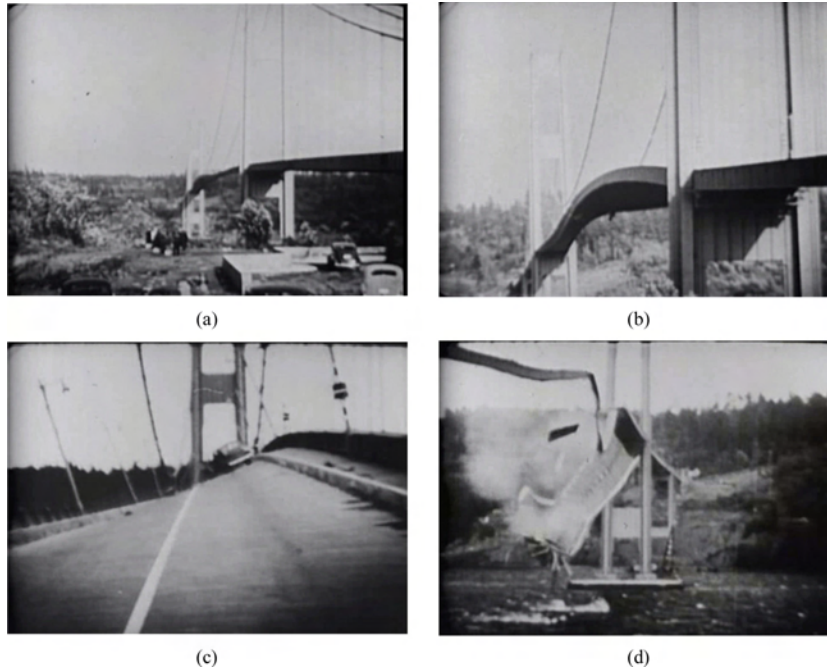


Figure 1.4: Collapse of the Takoma bridge, USA, 1940 (total span 1810.2 m): (a-c) views of the suspended deck under big deformations due to the resonance under wind load; (d) failure of the bridge. Source: (www.wikipedia.it).

- suspended bridges: they typically consist of two compressive towers and a net of tensile cables in the longitudinal and vertical directions, that directly support the deck (Fig. 1.3a,b);
- cable-stayed bridges: they work similarly to suspended bridges but in this case there is a system of inclined secondary cables that prestress the deck in compression (Fig. 1.3c,d).
- beam bridges: the main structure is made of one or more beams in bending, typically each beam is simply supported to allow rigid deformations (eg. in case of earthquake) without stresses (Fig. 1.5a,b);
- truss bridges: they are made of members in compression (struts) and in tension (tie) connected with ball joints, so each member is not in bending (Fig. 1.5c,d).

1. MOTIVATION AND BACKGROUND

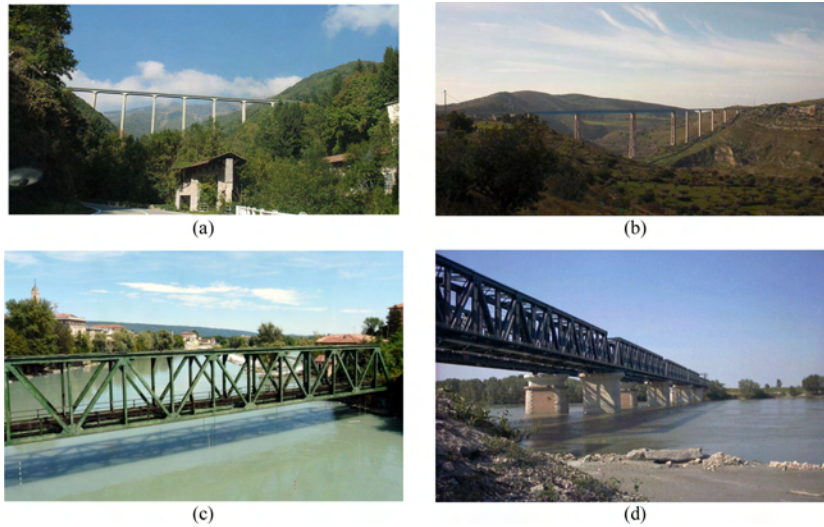


Figure 1.5: Examples of beam bridges (a-b) and truss bridges (c-d): (a) Pistoletta viaduct, Mosso, Italy; (b) Costanzo bridge on the Irminio river, Italy; (c) truss bridge in Ivrea, Italy; (d) truss bridge on Po river, Italy. Source: (www.wikipedia.it).

The type of bridges described above are still used nowadays. Usually beam bridges, working in bending, are often made of prestressed or reinforced concrete and they are very massive and stiff. Efficient materials in compression like masonry are used to build arch bridges (Fig. 1.2). Indeed, metallic materials are typically used for truss bridges (Fig. 1.5) or suspended and cable-stayed bridges (Fig. 1.3) because of their high performance in both compression and tension.

1.2 Basic Notions of Tensegrity Structures

Tensegrity structures are prestressable truss structures, which are obtained by connecting compressive members (bars or struts) through pre-stretched tensile elements (cables or strings). Motivated by nature, where tensegrity concepts appear in every cell, in the molecular structure of the spider fiber, and in the

1. MOTIVATION AND BACKGROUND

arrangement of bones and tendons for control of locomotion in animals and humans, engineers have only recently developed efficient analytical methods to exploit tensegrity concepts in engineering design. Previous attempts to judge the suitability of tensegrity for engineering purposes have often evaluated the tensegrity produced as art-forms, and then judged them according to a different (engineering) criteria. The development of "tensegrity engineering" methods is one of the main goal of the present thesis.

Designing tensegrity for engineering objectives has produced minimal mass solutions for five fundamental problems in engineering mechanics (Fig. 1.6). Minimal mass for tensile structures, (subject to stiffness constraints) was motivated by the molecular structure of spider fiber, and may be found in Fig. 1.6b. Minimal mass structures for compressive loads (Fig. 1.6c,d), cantilevered bending loads (Fig. 1.6e), torsional loads (Fig. 1.6f), and distributed loads on simply-supported span (Fig. 1.6g) have also been recently designed.

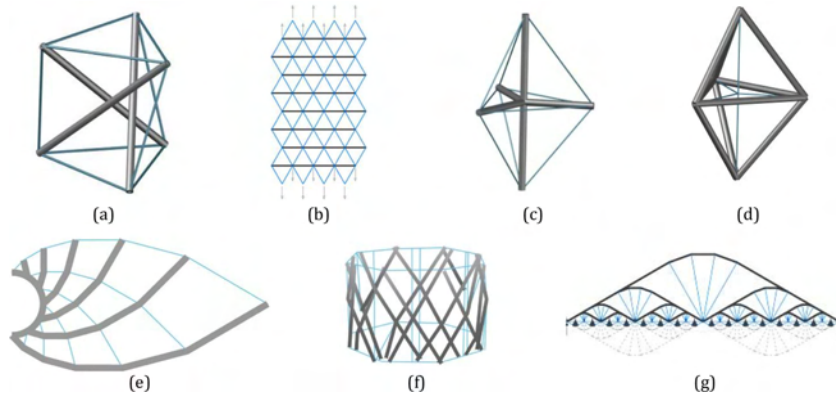


Figure 1.6: Illustration of some basic building blocks of tensegrity structures: (a): minimal tensegrity prism; (b): tensile unit, (c) T-bar unit; (d) D-bar unit; (e): Michell truss; (f) cylindrical unit; (g) bridge unit. Source: ([141, 136, 137]).

The subject of form-finding of tensegrity structures has attracted the attention of several researchers in recent years, due to the special ability of such structures to serve as controllable systems (geometry, size, topology and pre-stress control), and also because it has been recognized that the tensegrity

1. MOTIVATION AND BACKGROUND

architecture provides minimum mass structures for a variety of loading conditions, including structures subject to cantilevered bending load; compressive load; tensile load (under given stiffness constraints); torsion load; and simply supported boundary conditions (e.g. a bridge), without yielding and buckling (refer, e.g., to [25, 26, 27, 28], and references therein). Other additional advantages of tensegrity structures over more conventional control systems are related to the possibility to integrate control functions within the design of the structure: in controlled tensegrity systems the mechanics of the controller and the structure can naturally cooperate, through the change of the configurational equilibrium of the structure, as opposed to traditional control systems, where often the control pushes against the equilibrium of the structure. It is also worth noting that it is possible to look at a tensegrity structure as a multiscale sensor/actuator, which features highly nonlinear dynamical behavior (geometrical and/or mechanical nonlinearities), and can be controlled in real time [27, 18].

Particularly interesting is the use of fractal geometry as a form-finding method for tensegrity structures, which is well described in [25, 26, 27]. Such an optimization strategy exploits the use of fractal geometry to design tensegrity structures, through a finite or infinite number of self-similar subdivisions of basic modules. It looks for the optimal values of suitable complexity parameters, according to given mechanical performance criteria, and generates admirable *tensegrity fractals*. The self-similar tensegrity design presented in [25, 26, 27] is primarily focused on the generation of *minimum mass* structures, which are of great technical relevance when dealing, e.g., with tensegrity bridge structures (refer, e.g., to [13]). The ‘fractal’ approach to tensegrity form-finding paves the way to an effective implementation of the tensegrity paradigm in *parametric architectural design* [23, 22, 21].

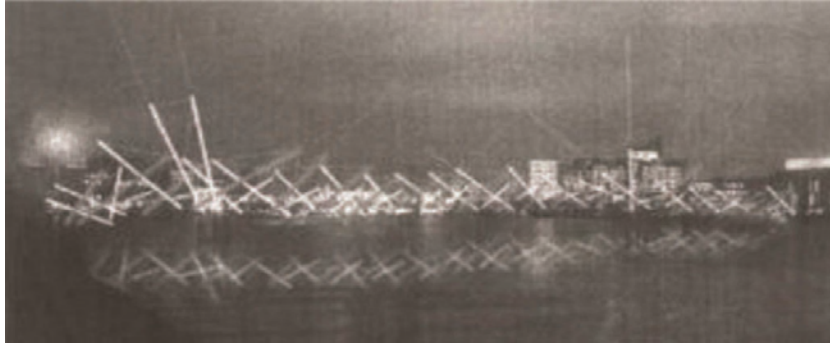


Figure 1.7: Presentation of a concept for tensegrity bridge in London. Source: (Boeck, 2013, p. 19, [1]).

1.3 Tensegrity Bridges

Several examples of realized and proposed tensegrity bridges are considered in this section. They were collected from an investigation on the state of the art and available literature on this field. First of all, Jan De Boeck (2013) [1] shownw that tensegrity appeared for the first time in 1996. Then Mott MacDonald submitted a conceptual project (Fig. 1.7) for the London’s Millennium Bridge. A step towards a tensegrity bridge was taken in 1998 in Purmerend, Netherlands as noted by Boeck (2013) [1]. Architect Jord den Hollander designed a pedestrian bridge comprises 18 spans of 4 m to cross a river (Fig. 1.8).

Andrea Micheletti (2012) [2] designed in 2005 the Tor Vergata footbridge (Fig. 1.9). The project was built close to the Faculty of Engineering of the University of Tor Vergata in Rome. This is a pedestrians bridge over one of the main road of the campus. The footbridge is nontrivial example of a modular tensegrity structure and is composed of five equal modules. The whole structure spans a distance 32 m without intermediate supports and its main axis has a banana shape with a maximum slope at the end modules of 5 %.

1. MOTIVATION AND BACKGROUND



Figure 1.8: Bridge in Purmerend. Source: (Boeck, 2013, p. 19, [1]).

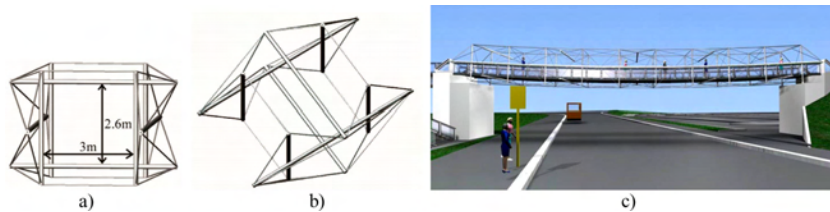


Figure 1.9: Tor Vergata footbridge: a), b) Two views of the footbridge module, c) Side view of the footbridge structure. Source: (Micheletti, 2012, p. 5, 10, [2])

The Kurilpa Bridge in Brisbane, Australia (Fig. 1.10) is the largest tensegrity - inspired bridge in the World. It exhibits some tensegrity members, but clearly it isn't a pure tensegrity structure as noted by Beck and Cooper (2012) [3]. The bridge was designed by Cox Rayner Architects and Arup and opened in 2009. The structure connects Kurilpa Point in South Brisbane to Tank Street in the Brisbane. The tensegrity bridge comprises three spans: a central span of 128 m and two side spans of 57 m and 45 m respectively, as reported by ARUP (2010) [4]. Barbarigos et al. (2010) [11] proposed a tensegrity "hollow rope" structure for a pedestrian bridge (Fig. 1.11) to be built in Switzerland.

1. MOTIVATION AND BACKGROUND



Figure 1.10: Kurilpa bridge. Source: ([http://tensegrity.wikispaces.com/Kurilpa + Bridge](http://tensegrity.wikispaces.com/Kurilpa+Bridge))



Figure 1.11: Tensegrity "hollow rope" pedestrian bridge. Source: (Barbarigos et al., 2010, p. 1159, [11])

It spans 20 m over a river and is composed of four identical tensegrity modules.

Briseghella et al. (2010) [5] designed a tensegrity footbridge of 30 m span with an arch deck (Fig. 1.12). Jan De Boeck (2013) [1] created a bridge like structure comprising a set of 3 struts tensegrity modules with a span of 12 m, juxtaposed next to each other (Fig. 1.13). The "Suspended Tensegrity Bridge" (Fig. 1.14) was designed by Stefano Paradiso and Marco Mucedola (2010) [6]. They designed a footbridge over the Sesia river, close to city of Greggio, Italy. Moreover, Fig. 1.15 shown a Tim Tyler's [7] conceptual project for a twisting hexagonal bridge.

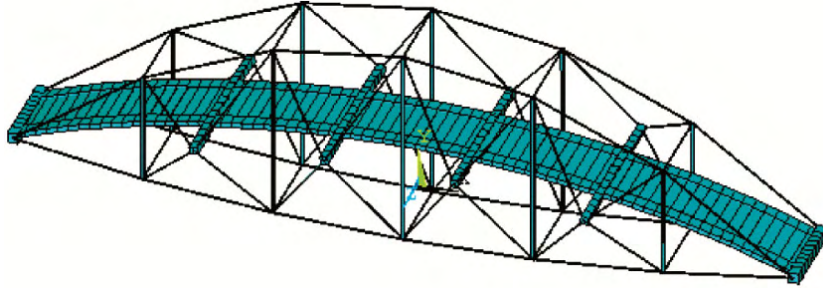


Figure 1.12: Tensegrity footbridge with an arch deck. Source: (Briseghella et al., 2010, p. 288, [5])

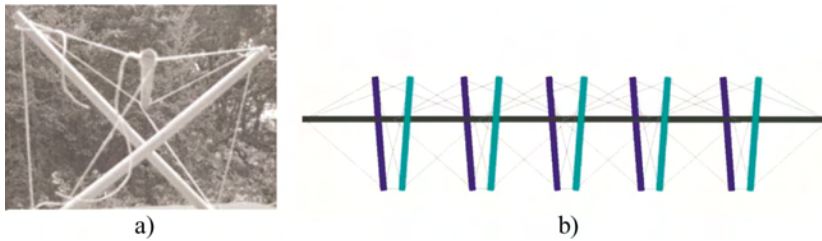


Figure 1.13: Jan De Boeck's tensegrity bridge: a) Front view of a rotated model of a 3 strut tensegrity module, b) Sketch illustrating how a 3 strut tensegrity module is multiplied and connected to a bridge like structure. Source: (Jan De Boeck, 2013, p. 65, 67, [1])

1.4 Research Goals

The present thesis deals with the parametric design of tensegrity bridges, through self-similar repetitions, at different scales of complexity. Michell [20] derived the minimal mass topology when superstructures is only allowed above the roadbed. Deck design requires structure below the roadbed. Here we integrate the two to minimize mass of the total bridge. The design variables consist of several complexity parameters and aspect angles, which rule the geometry of the *superstructure* and the *substructure*. The iterative procedure proposed in [145] is employed to generate minimum mass shapes under yielding

1. MOTIVATION AND BACKGROUND

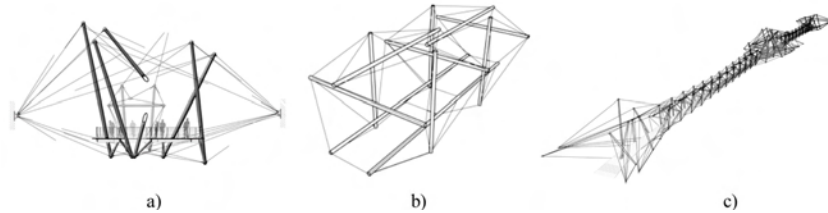


Figure 1.14: Suspended Tensegrity Bridge: a) Vertical cross section, b) Model of two tensegrity modules, c) Sketch illustrating the whole tensegrity bridge. Source: ([http://tensegrity.wikispaces.com/Suspended + Bridge + by + Paradiso](http://tensegrity.wikispaces.com/Suspended+Bridge+by+Paradiso))

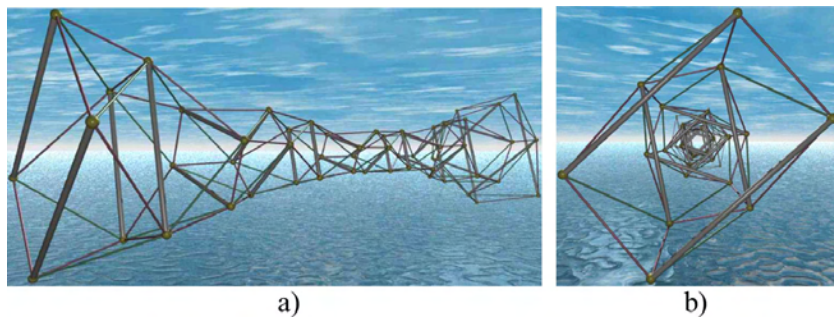


Figure 1.15: Tim Tyler's conceptual project for a twisting hexagonal bridge: a), b) Different views of the model. Source: (<http://hexdome.com/bridges>)

and buckling constraints, for varying values of the design variables.

Tensegrity structures are well suited for building bridges, being particularly light-weight and therefore able to cover long spans. In addition, they can be designed to have tunable stiffness, still remaining lightweight, by playing with the prestress of cable members (stiff or compliant structure). Finally, they can easily reproduce funicular structures, such as, e.g. the suspended bridges represented in Fig. 1.3 and the arch bridges illustrated in Fig. 1.2.

The tensegrity paradigm used for bridges allows the marriage of composite structures within the design. We indeed show in this dissertation that the tensegrity approach may lead to create a network of tension and compressive

1. MOTIVATION AND BACKGROUND

members distributed throughout the system at many different scales.

We develop a new method for bridge design which compares different solutions with the aim to minimize the total cost required to build the structure. Such optimization can be performed on different type of bridges with parametric geometries and then the optimal parameters can be detected. For example, given the span and the loads, we can compare *superstructure* and *substructure* bridges (see [141][137][145] for some numerical example). We will show that tensile elements have typically smaller masses than the compressive members because of the buckling. For this reason the optimal topology tends to maximize the number of tensile members and to reduce the length of compressive members (see the results in [141][137][145]). One should bear in mind, for instance, the two cases of arch bridges and suspended bridges.

In the first case there are one or more arches in compression with very high masses, which typically support an above deck. In the second case there is a very light stretched inverted arch with vertical cables that carry a below deck. Usually, the arch bridges appear to be more mass (so more expensive) than the suspended bridges and this could be analytically investigated with the method proposed in this thesis.

2

**Analytic Results on the
Optimal Design of Tensegrity
Bridges**

2.1 Introduction

This Chapter focuses on a form-find approach to tensegrity bridges based on mass minimization and fractal geometry. The subject of form-finding of tensegrity structures continues to be an active research area [19, 22, 23, 29, 30, 31], due to the special ability of such structures to serve as controllable systems (geometry, size, topology and prestress control), and also because the tensegrity architecture provides minimum mass structures for a variety of loading conditions, [25, 26, 27, 145]. Particularly interesting is the use of fractal geometry as a form-finding method for tensegrity structures, which is well described in [25, 26, 27, 17]. Such an optimization strategy exploits the use of fractal geometry to design tensegrity structures, through a finite or infinite number of self-similar subdivisions of basic modules. The strategy looks for the optimal number of self-similar iterations to achieve minimal mass or other design criteria. This number is called the optimal *complexity*, since this number fixes the total number of parts in the structure.

The self-similar tensegrity design presented in [25, 26, 27] is primarily focused on the generation of *minimum mass* structures, which are of great technical relevance when dealing with tensegrity bridge structures (refer, e.g., to [13]). The ‘fractal’ approach to tensegrity form-finding paves the way to an effective implementation of the tensegrity paradigm in *parametric architectural design* [23, 22, 21, 12].

The present Chapter deals with a parametric approach to the minimum mass design of tensegrity structures carrying simply supported and distributed bending loads. In [141] numerical solutions were found for a specified topology, without any theoretical guarantees that those topologies produced minimal mass. This Chapter provides more fundamental proofs that provide necessary and sufficient conditions for minimal mass. A different parametric approach to tensegrity bridges is presented in Chap. 3.

The remainder of the Chapter is organized as follows. Section 2.2 provides some basic knowledges on the mode of failure of tensile and compressive

members. Section 2.3 describes the topology of the tensegrity bridge under examination. For a simply-supported structure of the simplest complexity, Section 2.4 describes the minimal mass bridge when the admissible topology allows *substructure* and *superstructure* (that is, respectively, structure below and above the roadbed). Section 2.5 provides closed-form solutions to the minimal mass bridge designs (of complexity $n = 1$) when only sub- or superstructure is allowed. Section 2.6 provides closed-form solutions to the minimal mass bridge designs (of complexity $n, p = q = 1$) when only sub- or superstructure is allowed. This finalizes the proof that the minimal mass bridge is indeed the *substructure* bridge. Section 2.7 also defines deck mass and adds joint mass and shows that the optimal complexity is finite. Discussion of the results are offered at the end of this Chapter.

2.2 Properties of Tensile and Compressive Components of the Tensegrity Structure

The tensegrity structures in this paper will be composed of rigid compressive members called *bars*, and elastic tensile members called *cables*. We will assume that a tensile member obeys Hooke's law,

$$t_s = k(s - s_0), \tag{2.1}$$

where k is cable stiffness, t_s is tension in the cable, s is the length of the cable, and $s_0 < s$ is the rest length of the cable. The tension members cannot support compressive loads. For our purposes, a compressive member is a solid cylinder, called a bar. All results herein are trivially modified to accommodate pipes, tubes of any material, but the concepts are more easily demonstrated and the presentation is simplified by using the solid bar in our derivations. The minimal mass of a cable with loaded length s , yield strength σ_s , mass

2. ANALYTIC RESULTS ON THE OPTIMAL DESIGN OF TENSEGRITY BRIDGES

density ϱ_s , and maximal tension t_s is

$$m_s = \frac{\varrho_s}{\sigma_s} t_s s. \quad (2.2)$$

To avoid yielding, a bar of length b , yield strength σ_b , mass density ϱ_b with compression force f_b , has the minimal mass

$$m_{b,Y} = \frac{\varrho_b}{\sigma_b} f_b b. \quad (2.3)$$

To avoid buckling, the minimal mass of a round bar of length b , modulus of elasticity E_b , and maximal force f_b is

$$m_{b,B} = 2\varrho_b b^2 \sqrt{\frac{f_b}{\pi E_b}}. \quad (2.4)$$

The actual mode of failure (buckling or yielding) of a compressive member can be identified by using the following well-know facts that give the basis to a correct design of the bar radius r_b . Define r_Y , the bar radius that satisfies yielding constraints, and r_B , the radius that satisfies buckling constraints, by

$$r_Y = \sqrt{\frac{f_b}{\pi \sigma_b}}, \quad r_B = \sqrt[4]{\frac{4b^2 f_b}{\pi^3 E_b}}. \quad (2.5)$$

The following are well known facts:

Lemma 2.2.1. *Designs subject to only yield constraints (hence $r_b = r_Y$) fail to identify the actual mode of failure (buckling) if $r_Y < r_B$, or equivalently if,*

$$\frac{f_b}{b^2} < \frac{4\sigma_b^2}{\pi E_b}. \quad (2.6)$$

Lemma 2.2.2. *Designs subject to only yield constraints ($r_b = r_Y$) automati-*

cally also satisfy buckling constraints if $r_Y > r_B$, or equivalently if,

$$\frac{f_b}{b^2} > \frac{4\sigma_b^2}{\pi E_b}. \quad (2.7)$$

Lemma 2.2.3. *Designs subject to only buckling constraints ($r_b = r_B$) fail to identify the actual mode of failure (yielding) if $r_B < r_Y$, or equivalently if,*

$$\frac{f_b}{b^2} > \frac{4\sigma_b^2}{\pi E_b}. \quad (2.8)$$

Lemma 2.2.4. *Designs subject to only buckling constraints ($r_b = r_B$) automatically also satisfy yielding constraints if $r_B > r_Y$, or equivalently if,*

$$\frac{f_b}{b^2} < \frac{4\sigma_b^2}{\pi E_b}. \quad (2.9)$$

2.3 Planar Topologies of the Tensegrity Bridges Under Study

The planar bridge topology is considered here to elucidate the fundamental properties that are important in the vertical plane. We use the following nomenclature, referring to Fig. 2.2:

- A *superstructure* bridge has no structure below the deck level.
- A *substructure* bridge has no structure above the deck level.
- A *nominal* bridge contains both *substructure* and *superstructure*.
- *Y* means the design was constrained against yielding for both cables and bars.
- *B* means the design was constrained against yielding for cables and buckling for bars.
- *n* means the number of self-similar iterations involved in the design ($n = 1$ in Fig 2.2, and $n \geq 1$ in Fig. 2.3).

2. ANALYTIC RESULTS ON THE OPTIMAL DESIGN OF TENSEGRITY BRIDGES

- p means the complexity of each iteration in the substructure ($p = 1$ in Fig 2.2c, and $p \geq 1$ in Fig 2.3).
- q means the complexity of each iteration in the superstructure ($q = 1$ in Fig 2.2b, and $q \geq 1$ in Fig 2.3).
- α is the aspect angle of the *superstructure* measured from the horizontal.
- β is the aspect angle of the *substructure* measured from the horizontal.

For a tensegrity bridge with generic complexities n , p and q (see Fig. 2.3), the total number of nodes n_n of each topology is given by:

$$n_n = (p + q)(2^n - 1) + 2^n + 1. \quad (2.10)$$

For the *substructure* bridge (that is $q = 0$), the number of bars n_b and the number of cables n_s are:

$$n_b = p(2^n - 1), \quad n_s = (p + 1)(2^n - 1) + 2^n. \quad (2.11)$$

For the *superstructure* bridge (that is $p = 0$), the number of bars n_b and the number of cables n_s are:

$$n_b = (q + 1)(2^n - 1), \quad n_s = q(2^n - 1) + 2^n. \quad (2.12)$$

For the *nominal* bridge, the number of bars n_b and the number of cables n_s are:

$$n_b = (p + q + 1)(2^n - 1), \quad n_s = (p + q + 1)(2^n - 1) + 2^n. \quad (2.13)$$

2. ANALYTIC RESULTS ON THE OPTIMAL DESIGN OF TENSEGRITY BRIDGES

We define the *superstructure* bridge of complexity $(n, p = 0, q)$ by Fig. 2.3 where the *substructure* below is deleted. We define the *substructure* bridge of complexity $(n, p, q = 0)$ by Fig. 2.3 where the *superstructure* above is deleted.

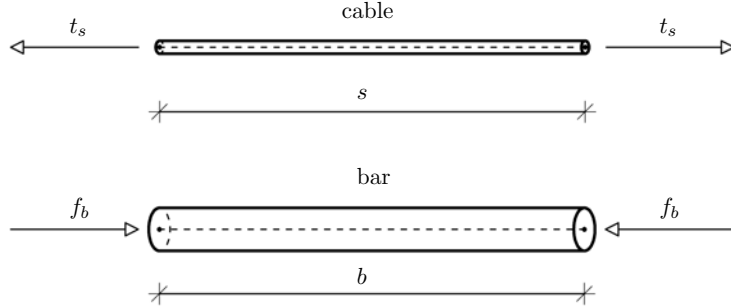


Figure 2.1: Adopted notation for bars and cables of a tensegrity system.

2.4 Analysis of the Basic Modules ($n = 1, p = 1$ or $0, q = 1$ or 0)

We first will examine the simplest of bridge concepts, as in Fig 2.2. Consider, first, the *nominal* bridge, subject to yield constraints, with complexity $(n, p, q) = (1, 1, 1)$. This configuration, described by Fig 2.2a, is composed of 5 cables and 3 bars. Let the bottom end of each compressive member above the deck be constrained by a hinge boundary condition, so as to allow rotation but not translation. Define F as the total applied load, and L as the span. All cables use the same material, and all bars use the same material. It will be convenient to define the following constants:

$$\varrho = \frac{\varrho_b/\sigma_b}{\varrho_s/\sigma_s}, \quad (2.14)$$

2. ANALYTIC RESULTS ON THE OPTIMAL DESIGN OF TENSEGRITY BRIDGES

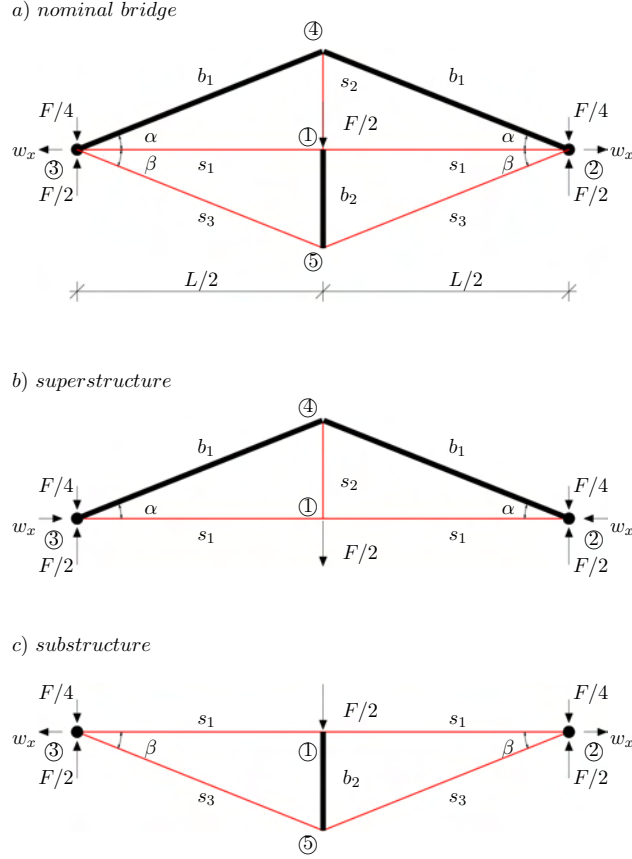


Figure 2.2: Basic modules of the tensegrity bridge with: a) nominal bridge: $n = q = p = 1$; b) superstructure: $n = q = 1$; c) substructure: $n = p = 1$.

$$\eta = \frac{\varrho_b L}{(\varrho_s / \sigma_s) \sqrt{\pi E_b F}}. \quad (2.15)$$

Define a normalization of the system mass m by the dimensionless quantity μ :

$$\mu = \frac{m}{(\varrho_s / \sigma_s) FL}, \quad (2.16)$$

2. ANALYTIC RESULTS ON THE OPTIMAL DESIGN OF TENSEGRITY BRIDGES

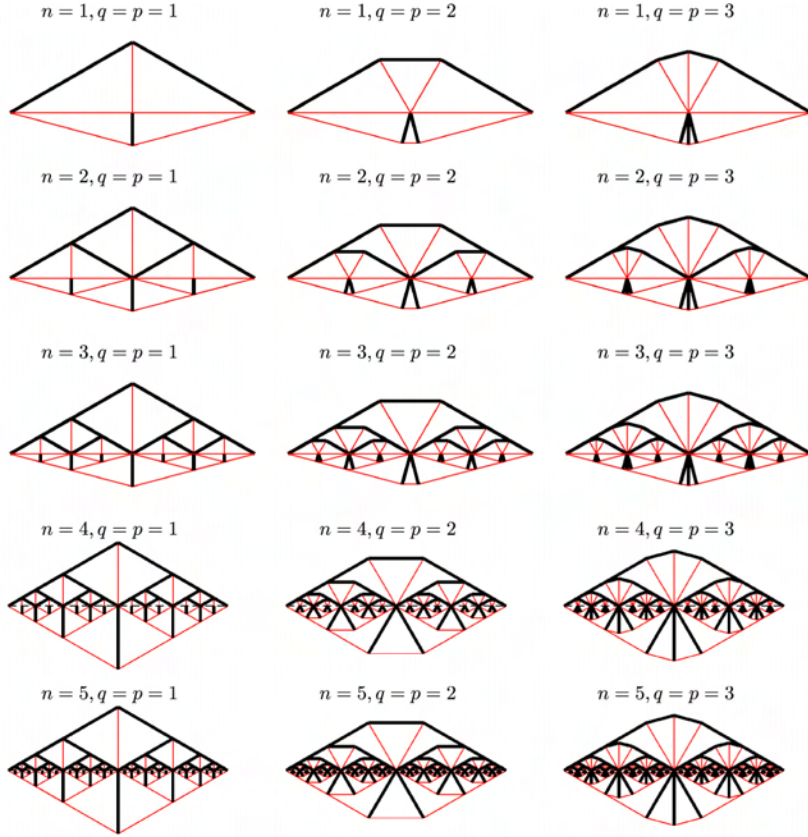


Figure 2.3: Exemplary geometries of the nominal bridges for different values of the complexity parameters n (increasing downward) and q (increasing leftward).

where the mass m at the yield condition is:

$$m = \frac{\rho_b}{\sigma_b} \sum f_i b_i + \frac{\rho_s}{\sigma_s} \sum t_i s_i, \quad (2.17)$$

where (b_i, s_i) is respectively the length of the i^{th} bar or i^{th} cable, and respectively (f_i, t_i) is the force in the i^{th} bar or cable.

The mass of the *nominal* bridge will be minimized over the choice of angles α

2. ANALYTIC RESULTS ON THE OPTIMAL DESIGN OF TENSEGRITY BRIDGES

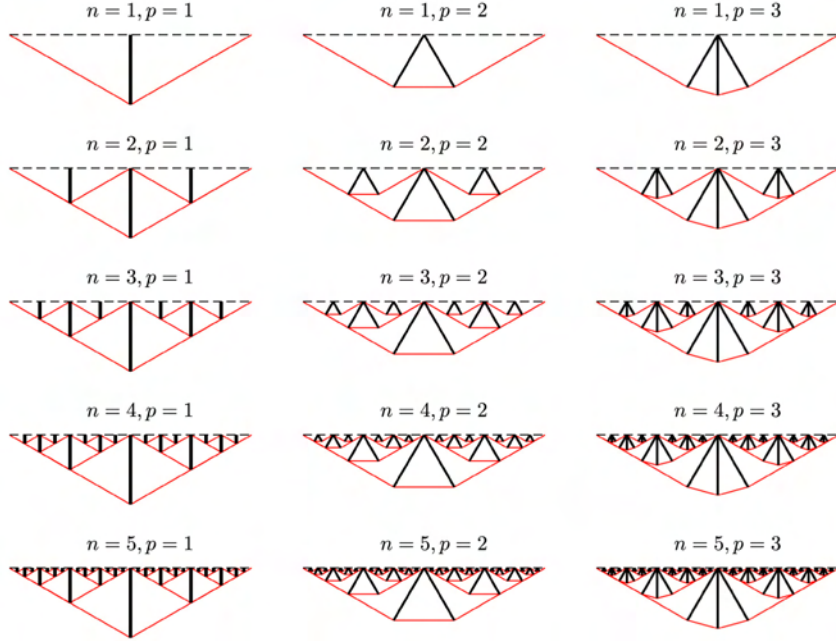


Figure 2.4: Exemplary geometries of the substructures for different values of the complexity parameters n (increasing downward) and p (increasing leftward).

and β . The lengths of the members are:

$$\begin{aligned}
 s_1 &= \frac{L}{2}, & s_2 &= \frac{L}{2} \tan \alpha, & s_3 &= \frac{L}{2 \cos \beta} = \frac{L}{2} \sqrt{1 + \tan^2 \beta}, \\
 b_1 &= \frac{L}{2 \cos \alpha} = \frac{L}{2} \sqrt{1 + \tan^2 \alpha}, & b_2 &= \frac{L}{2} \tan \beta.
 \end{aligned} \tag{2.18}$$

The equilibrium equations at each node are:

2. ANALYTIC RESULTS ON THE OPTIMAL DESIGN OF TENSEGRITY BRIDGES

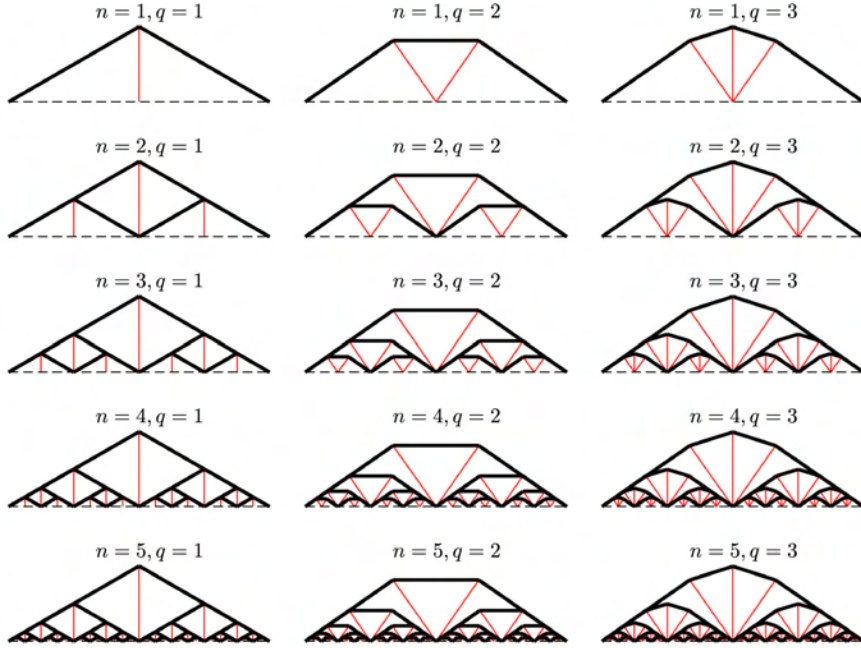


Figure 2.5: Exemplary geometries of the superstructures for different values of the complexity parameters n (increasing downward) and q (increasing leftward).

$$\begin{aligned}
 t_1 + t_3 \cos \beta &= w_x + f_1 \cos \alpha, \\
 \frac{F}{4} &= f_1 \sin \alpha + t_3 \sin \beta, \\
 t_2 &= 2f_1 \sin \alpha, \\
 f_2 &= 2t_3 \sin \beta, \\
 \frac{F}{2} &= t_2 + f_2.
 \end{aligned} \tag{2.19}$$

This system of equations can be solved, choosing t_1 and t_3 are free independent parameters:

2. ANALYTIC RESULTS ON THE OPTIMAL DESIGN OF TENSEGRITY BRIDGES

$$\begin{aligned}
\frac{f_1}{F} &= \frac{\sqrt{1 + \tan^2 \alpha}}{4 \tan \alpha} \left(1 - \frac{t_3}{F} \frac{4 \tan \beta}{\sqrt{1 + \tan^2 \beta}}\right), \\
\frac{f_2}{F} &= \frac{t_3}{F} \frac{2 \tan \beta}{\sqrt{1 + \tan^2 \beta}}, \\
\frac{t_2}{F} &= \frac{1}{2} - \frac{t_3}{F} \frac{2 \tan \beta}{\sqrt{1 + \tan^2 \beta}}, \\
\frac{w_x}{F} &= \frac{t_1}{F} + \frac{t_3}{F} \frac{\tan \alpha + \tan \beta}{\tan \alpha \sqrt{1 + \tan^2 \beta}} - \frac{1}{4 \tan \alpha}.
\end{aligned} \tag{2.20}$$

2.4.1 Nominal Bridges under Yielding Constraints

Theorem 2.4.1. *Given the nominal bridge with complexity $(n, p, q) = (1, 1, 1)$ (described in Fig. 2.2a), with attendant data (2.18), the minimal mass can be expressed in terms of independent variables t_1 and t_3 :*

$$\mu_Y(t_1, t_3) = \frac{t_1}{F} + \frac{t_3}{F} c_3(\alpha, \beta, \varrho) + \frac{b_\alpha}{4}, \tag{2.21}$$

where:

$$c_3(\alpha, \beta, \varrho) = \frac{(1 + \varrho) \tan^2 \beta - b_\alpha \tan \beta + 1}{\sqrt{1 + \tan^2 \beta}}, \quad b_\alpha = \frac{\varrho + (1 + \varrho) \tan^2 \alpha}{\tan \alpha} \tag{2.22}$$

An alternate expression for the mass can be written by substituting the relation between t_2 and t_3 from (27), to get an equivalent expression $\mu_Y(t_1, t_2) = \mu_Y(t_1, t_3)$, where:

2. ANALYTIC RESULTS ON THE OPTIMAL DESIGN OF TENSEGRITY BRIDGES

$$\frac{t_3}{F} = \frac{\sqrt{1 + \tan^2 \beta}(1 - 2t_2/F)}{4 \tan \beta}, \quad (2.23)$$

$$\mu_Y(t_1, t_2) = \frac{t_1}{F} + \frac{t_2}{F} c_2(\alpha, \beta, \varrho) + \frac{(1 + \varrho) \tan^2 \beta + 1}{4 \tan \beta}, \quad (2.24)$$

$$c_2(\alpha, \beta, \varrho) = -c_3 \frac{\sqrt{1 + \tan^2 \beta}}{2 \tan \beta} = -\frac{(1 + \varrho) \tan^2 \beta - b_\alpha \tan \beta + 1}{2 \tan \beta}. \quad (2.25)$$

Hence it follows that the minimal mass solution requires $t_3 > 0$ if and only if $c_3 < 0$ (equivalently $c_2 > 0$). Note also that $c_3 < 0$ if and only if:

$$\frac{1 + (1 + \varrho) \tan^2 \beta}{\tan \beta} < \frac{\varrho + (1 + \varrho) \tan^2 \alpha}{\tan \alpha}. \quad (2.26)$$

Conversely, minimal mass requires $t_3 = 0$ if $c_3 > 0$ (equivalently $c_2 < 0$). This event occurs if and only if:

$$\frac{1 + (1 + \varrho) \tan^2 \beta}{\tan \beta} > \frac{\varrho + (1 + \varrho) \tan^2 \alpha}{\tan \alpha}. \quad (2.27)$$

Finally, $c_3 = 0$ (and also $c_2 = 0$) if and only if:

$$\frac{1 + (1 + \varrho) \tan^2 \beta}{\tan \beta} = \frac{\varrho + (1 + \varrho) \tan^2 \alpha}{\tan \alpha}. \quad (2.28)$$

Note also that the requirement that t_2 and t_3 both be non-negative values limits the feasible range of t_3 such that:

$$0 \leq t_3 \leq \frac{F \sqrt{1 + \tan^2 \beta}}{4 \tan \beta}. \quad (2.29)$$

Given the relation between t_2 and t_3 in (2.23) we have the corresponding

2. ANALYTIC RESULTS ON THE OPTIMAL DESIGN OF TENSEGRITY BRIDGES

feasible range for t_2 :

$$0 \leq t_2 \leq \frac{F}{2}. \quad (2.30)$$

The proof of the theorem follows the mass calculation in (4.9), (4.19) after substituting the equilibrium forces given by (2.20).

Corollary 2.4.1. *Consider a superstructure bridge with complexity $(n, p, q) = (1, 0, 1)$ (topology is defined by Fig. 2.2b). The minimal mass μ_Y requires the following aspect angle:*

$$\alpha_Y^* = \arctan \left(\sqrt{\frac{\varrho}{1 + \varrho}} \right), \quad (2.31)$$

which corresponds to the following dimensionless minimal mass:

$$\mu_Y^* = \frac{1}{2} \sqrt{\varrho(1 + \varrho)}. \quad (2.32)$$

Proof. The mass of the superstructure can be obtained from Theorem (2.4.1) by setting $t_1 = 0$ since its coefficient is positive, and $t_3 = 0$ since the cable s_3 is absent. Thus,

$$\mu_Y = \frac{\tan \alpha}{4} + \varrho \frac{(1 + \tan^2 \alpha)}{4 \tan \alpha}. \quad (2.33)$$

This function has a unique minimum satisfying,

$$\frac{\partial \mu_Y}{\partial \tan \alpha} = \frac{\tan^2 \alpha + \varrho (\tan^2 \alpha - 1)}{4 \tan^2 \alpha} = 0, \quad (2.34)$$

2. ANALYTIC RESULTS ON THE OPTIMAL DESIGN OF TENSEGRITY BRIDGES

producing the unique optimal angle (2.31). Substituting this angle into (2.33) concludes the proof. □

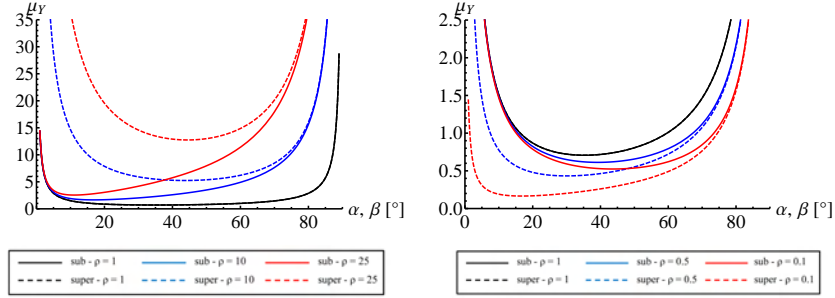


Figure 2.6: Dimensionless masses of the substructure (continuous curves) and superstructure (dashed curves) for different values of the aspect angles (respectively β or α) and for values of the coefficient $\varrho > 1$ (left) and $\varrho < 1$ (right) under yielding constraints.

Fig 2.6 plots the mass versus the angle β and α , yielding the minimum at the values given by (2.35) and (2.31). All designs in this section assume failure by yielding. One must check that yielding is indeed the mode of failure.

Corollary 2.4.2. *Consider a substructure bridge, with complexity $(n, p, q) = (1, 1, 0)$ (topology is defined by Fig. 2.2c). The minimal mass design under only yield constraints is given by the following aspect angle:*

$$\beta_Y^* = \arctan\left(\frac{1}{\sqrt{1 + \varrho}}\right), \quad (2.35)$$

which corresponds to the following dimensionless minimal mass:

$$\mu_Y^* = \frac{\sqrt{1 + \varrho}}{2}. \quad (2.36)$$

Proof. The mass of the substructure can be obtained from Theorem (2.4.1) with $t_1 = t_2 = 0$ to obtain,

2. ANALYTIC RESULTS ON THE OPTIMAL DESIGN OF TENSEGRITY BRIDGES

$$\mu_Y = \frac{(1 + \tan^2 \beta)}{4 \tan \beta} + \frac{\varrho}{4} \tan \beta. \quad (2.37)$$

The the unique minimum satisfies,

$$\frac{\partial \mu_Y}{\partial \tan \beta} = -\frac{1 + \tan^2 \beta}{4 \tan^2 \beta} + \frac{1}{2} + \frac{\varrho}{4} = 0, \quad (2.38)$$

producing the optimal optimal angle of (2.35). Substituting this angle into (2.37) concludes the proof. \square

Corollary 2.4.3. *For the designs in this section, yielding is indeed the mode of failure if the following inequalities hold:*

$$\frac{F}{L^2} > \frac{1}{2(1 + \varrho)} \left(\frac{4\sigma_b^2}{\pi E_b} \right), \quad \text{if : } 0 < \varrho \leq \frac{1}{4} (\sqrt{3} - 1), \quad (2.39)$$

$$\frac{F}{L^2} > \frac{\sqrt{\varrho(1 + 2\varrho)}}{1 + \varrho} \left(\frac{4\sigma_b^2}{\pi E_b} \right), \quad \text{if : } \varrho > \frac{1}{4} (\sqrt{3} - 1). \quad (2.40)$$

In addition, if $0 < \varrho \leq \frac{1}{4} (\sqrt{3} - 1)$ and (2.39) holds or if $\frac{1}{4} (\sqrt{3} - 1) < \varrho < 1$ and (2.40) holds, then the minimal mass of a superstructure bridge is less than the minimal mass of a substructure bridge. (In this event, the minimal mass bridge is superstructure only). If $\varrho = 1$ and (2.40) also holds, then the minimal mass of the substructure bridge is equal to the minimal mass of the superstructure bridge. If $\varrho > 1$ and (2.40) also hold, then the minimal mass of the substructure bridge is less than the minimal mass of the superstructure bridge. (The minimal mass bridge is substructure only).

Proof. Under yield constraints, if the design has the property

$f_{b,i}/b_i^2 > 4\sigma_b^2/(\pi E_b)$, then this guarantees that yielding is the mode of failure in bar b_i , and the buckling constraints are also satisfied (see lemma

2. ANALYTIC RESULTS ON THE OPTIMAL DESIGN OF TENSEGRITY BRIDGES

2.2.2). For the superstructure, assuming the optimal angle (2.31), the minimal mass (2.32), the force f_1 (2.20) and the length b_1 (2.18), the lemma 2.2.2 reduces to:

$$\frac{F}{L^2} > \frac{\sqrt{\varrho(1+2\varrho)}}{1+\varrho} \left(\frac{4\sigma_b^2}{\pi E_b} \right). \quad (2.41)$$

Similarly, for the substructure, assuming the optimal angle (2.35), the minimal mass (2.36), the force f_2 (2.20) and the length b_2 (2.18), the Lemma 2.2.2 reduces to:

$$\frac{F}{L^2} > \frac{1}{2(1+\varrho)} \left(\frac{4\sigma_b^2}{\pi E_b} \right). \quad (2.42)$$

Yielding is the mode of failure of superstructure and substructure designs if both (2.41) and (2.42) hold or, equivalently, if the following holds:

$$\frac{F}{L^2} > \max \left[\frac{\sqrt{\varrho(1+2\varrho)}}{1+\varrho}, \frac{1}{2(1+\varrho)} \right] \left(\frac{4\sigma_b^2}{\pi E_b} \right). \quad (2.43)$$

From the inequality $\frac{\sqrt{\varrho(1+2\varrho)}}{1+\varrho} / \frac{1}{2(1+\varrho)} > 1$ we obtain the following conclusions:

$$\frac{\sqrt{\varrho(1+2\varrho)}}{1+\varrho} < \frac{1}{2(1+\varrho)}, \quad \text{if: } 0 < \varrho \leq \frac{1}{4}(\sqrt{3}-1), \quad (2.44)$$

$$\frac{\sqrt{\varrho(1+2\varrho)}}{1+\varrho} > \frac{1}{2(1+\varrho)}, \quad \text{if: } \varrho > \frac{1}{4}(\sqrt{3}-1). \quad (2.45)$$

Equations (2.44) and (2.45) combined with (2.43) give the conditions (2.39) and (2.40). The mass of the substructure is shown to be less than the mass of the superstructure if $\varrho > 1$, a result that follows by taking the ratio between the optimal mass of the superstructure (2.32) and the optimal mass of the

2. ANALYTIC RESULTS ON THE OPTIMAL DESIGN OF TENSEGRITY BRIDGES

substructure (2.36).

□

As a practical matter, ϱ is almost always greater than 1, since compressive members tend to have higher mass density than tension members ($\varrho_b/\varrho_s > 1$), and the yield strength of tensile material tends to be greater than for compressive members ($\sigma_s/\sigma_b > 1$).

Thus far the conclusion is that if $\varrho > \frac{1}{4}(\sqrt{3} - 1)$ then the bridge in Fig. 2.2a at its minimal mass configuration becomes the configuration of substructure in Fig. 2.2c, if the bridge design is constrained against yielding. Furthermore, such a design will not buckle. Note that this design produced a topology constrained against yielding, and a design constrained against buckling might produce a different topology. Now let's consider this possibility.

2.4.2 Nominal Bridges under Buckling Constraints

This section repeats all the designs of the previous section (for the three structures of Fig. 2.2) with the added constraint that the bars cannot buckle.

Theorem 2.4.2. *Consider a nominal bridge of complexity $(n, p, q) = (1, 1, 1)$. The minimal mass (the cable mass required at the yield conditions plus the bar mass required at the bar buckling conditions), is, in terms of t_1 and t_3 :*

$$\begin{aligned} \mu_B(t_1, t_3) = & \frac{t_1}{F} + \frac{t_3 \tan^2 \beta - \tan \alpha \tan \beta + 1}{F \sqrt{1 + \tan^2 \beta}} + \frac{\tan \alpha}{4} \\ & + \eta \left[\frac{(1 + \tan^2 \alpha)^{5/4}}{2\sqrt{\tan \alpha}} \left(1 - \frac{t_3}{F} \frac{4 \tan \beta}{\sqrt{1 + \tan^2 \beta}} \right)^{1/2} \right. \\ & \left. + \frac{\tan^2 \beta}{\sqrt{2}} \sqrt{\frac{t_3}{F} \frac{\tan \beta}{(1 + \tan^2 \beta)^{1/2}}} \right], \end{aligned} \quad (2.46)$$

or, equivalently, in terms of t_1 and t_2 :

2. ANALYTIC RESULTS ON THE OPTIMAL DESIGN OF TENSEGRITY BRIDGES

$$\begin{aligned} \mu_B(t_1, t_2) &= \frac{t_1}{F} + \frac{t_2}{F} \left[\frac{\tan \alpha}{2} - \frac{(1 + \tan^2 \beta)}{2 \tan \beta} \right] + \frac{(1 + \tan^2 \beta)}{4 \tan \beta} \\ &+ \eta \left[(1 + \tan^2 \alpha)^{(5/4)} \sqrt{\frac{t_2}{2F \tan \alpha}} + \frac{\tan^2 \beta}{2} \sqrt{\frac{1}{2} - \frac{t_2}{F}} \right]. \end{aligned} \quad (2.47)$$

Proof. Given the solution (2.20), the total mass of bars is:

$$\begin{aligned} m_{b,B} &= \frac{\varrho_b L^2 \sqrt{F}}{\sqrt{\pi E_b}} \left[\frac{(1 + \tan^2 \alpha)^{5/4}}{2 \sqrt{\tan \alpha}} \left(1 - \frac{t_3}{F} \frac{4 \tan \beta}{\sqrt{1 + \tan^2 \beta}} \right)^{1/2} \right. \\ &\quad \left. + \frac{\tan^2 \beta}{\sqrt{2}} \sqrt{\frac{t_3}{F} \frac{\tan \beta}{(1 + \tan^2 \beta)^{1/2}}} \right]. \end{aligned} \quad (2.48)$$

Adding to (2.48) the total mass of cables and using the (2.20), we obtain the total mass of (2.46) given in the theorem. It is also possible to write this mass in terms of free parameters t_t and t_2 .

$$m_{b,B} = \frac{\varrho_b L^2 \sqrt{F}}{\sqrt{\pi E_b}} \left[(1 + \tan^2 \alpha)^{5/4} \sqrt{\frac{t_2}{2F \tan \alpha}} + \frac{\tan^2 \beta}{2} \sqrt{\frac{1}{2} - \frac{t_2}{F}} \right]. \quad (2.49)$$

Adding to (2.49) the total mass of cables and using the (2.20), we obtain the total mass of (2.47). □

The value of $\beta = 4.25 \text{ deg}$ minimizes the mass (2.47) if the material choice is steel ($\varrho = 7862 \text{ kg/m}^3$; $\sigma = 6.9 \times 10^8 \text{ N/m}^2$; $E = 2.06 \times 10^{11} \text{ N/m}^2$). It will become clear that the minimal mass solution of the minimal bridge μ_B , constrained against buckling, will reduce to only a *substructure* (Fig 3c). It is straightforward to show that the mass of the bars is much greater than the

2. ANALYTIC RESULTS ON THE OPTIMAL DESIGN OF TENSEGRITY BRIDGES

mass of the cables under the usual condition:

$$\eta \gg \frac{\tan^2 \alpha}{2(1 + \tan^2 \alpha)^{5/4}}. \quad (2.50)$$

To prepare for those insights, now consider the individual solutions for designs constrained to be only *superstructure* or only *substructure* in configuration.

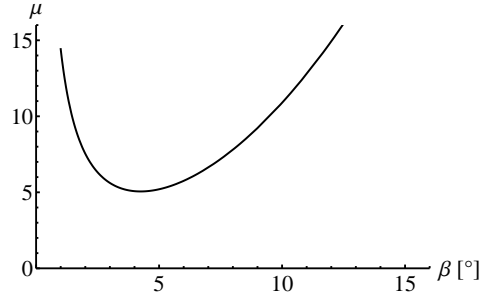


Figure 2.7: Mass $\mu_B(t_1, t_2)$ (Eq. 2.47) for different values of the aspect angles β assuming steel bars and cables, $F = 1 \text{ N}$, $L = 1 \text{ m}$ ($\eta = 857.71$), $t_1 = 0$ and $t_2 = 0$. The minimum value is $\mu_B^* = 5.0574$ at $\beta_B^* = 4.25 \text{ deg}$.

Corollary 2.4.4. *Consider a superstructure bridge of complexity $(n, p, q) = (1, 0, 1)$, (Fig. 2.2b). Suppose (2.50) holds. The minimal mass design under yielding and buckling constraints is given by the following aspect angle:*

$$\bar{\alpha}_B^* = \arctan\left(\frac{1}{2}\right), \quad (2.51)$$

which corresponds to the following dimensionless minimal mass:

$$\bar{\mu}_B^* = \frac{1}{8} \left(1 + 5^{(5/4)} \eta\right). \quad (2.52)$$

2. ANALYTIC RESULTS ON THE OPTIMAL DESIGN OF TENSEGRITY BRIDGES

Proof. The mass of the *superstructure* only case can be obtained from (2.46) assuming $t_1 = t_3 = 0$:

$$\mu_B = \frac{\tan \alpha}{4} + \eta \frac{(1 + \tan^2 \alpha)^{(5/4)}}{2\sqrt{\tan \alpha}}. \quad (2.53)$$

Assuming that the mass of the cables, which is the first term at the rhs of the (2.53) is neglectable if compared with the mass of the bars, which is the second term at the rhs of (2.53). Then the dimensionless mass becomes

$$\bar{\mu}_B = \eta \frac{(1 + \tan^2 \alpha)^{(5/4)}}{2\sqrt{\tan \alpha}}. \quad (2.54)$$

The solution for minimal mass can be achieved from the local minimum condition,

$$\frac{\partial \bar{\mu}_B}{\partial \tan \alpha} = \frac{5}{4} \eta (1 + \tan^2 \alpha)^{1/4} \sqrt{\tan \alpha} - \eta \frac{(1 + \tan^2 \alpha)^{5/4}}{4 \tan^{3/2} \alpha} = 0, \quad (2.55)$$

to obtain the optimal angle (2.51). Substituting it into (2.53) yields (2.52). \square

It is straightforward to show that the second variation of $\mu_B(\alpha)$ with respect to α is always positive, indicating that there is only one minimum described by (2.51).

Corollary 2.4.5. *Consider a substructure bridge, with complexity $(n, p, q) = (1, 1, 0)$ (Fig. 2.2c). The minimal mass design under yielding constraints and buckling constraints is given by the following aspect angle:*

$$\beta_B^* = \arctan \left[\frac{1}{6\eta} \left(\frac{1}{2^{(1/3)}\epsilon} + \frac{\epsilon}{2^{(2/3)}} - \frac{1}{\sqrt{2}} \right) \right], \quad (2.56)$$

2. ANALYTIC RESULTS ON THE OPTIMAL DESIGN OF TENSEGRITY BRIDGES

which corresponds to the following dimensionless minimal mass:

$$\mu_B^* = \frac{1 + \tan^2 \beta_B^*}{4 \tan \beta_B^*} + \frac{\eta}{2\sqrt{2}} \tan^2 \beta_B^*, \quad (2.57)$$

where:

$$\epsilon = \left[108\sqrt{2}\eta^2 + \sqrt{23328\eta^4 - 432\eta^2} - \sqrt{2} \right]^{1/3}. \quad (2.58)$$

Proof. The mass of the *substructure* bridge can be obtained from (2.47) assuming $t_1 = t_2 = 0$:

$$\mu_B = \frac{1 + \tan^2 \beta}{4 \tan \beta} + \frac{\eta}{2\sqrt{2}} \tan^2 \beta. \quad (2.59)$$

The above function has its minimum value μ_B^* for an optimal angle β_B^* that can be computed from the equation

$$\frac{\partial \mu_B}{\partial \tan \beta} = \frac{1}{2} - \frac{1 + \tan^2 \beta}{4 \tan^2 \beta} + \frac{\eta}{\sqrt{2}} \tan \beta = 0. \quad (2.60)$$

After rearranging (2.60), the optimal angle β can be computed solving the following equation:

$$4\eta \tan^3 \beta + \sqrt{2} \tan^2 \beta - \sqrt{2} = 0. \quad (2.61)$$

□

It is straightforward to show that the second variation of $\mu_B(\beta)$ with respect to β is always positive, indicating a unique global optimal value of (2.56). Fig 2.8 plots the mass versus the angle β and α , yielding the minimum at the

2. ANALYTIC RESULTS ON THE OPTIMAL DESIGN OF TENSEGRITY BRIDGES

values given by (2.51) and (2.56). We must verify if buckling is indeed the mode of failure in the designs of this section.

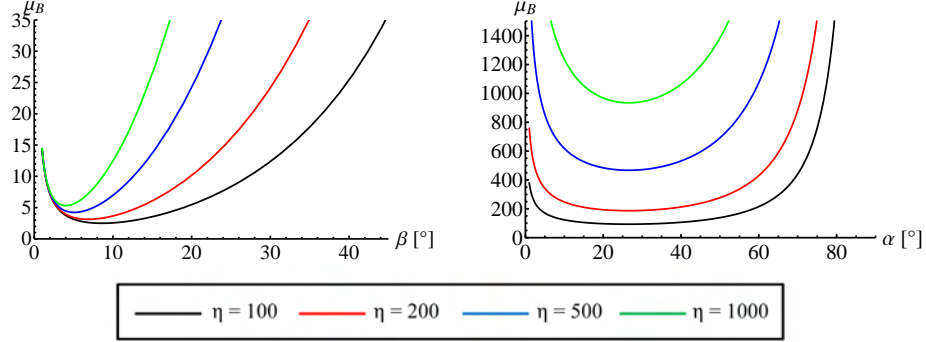


Figure 2.8: Dimensionless masses of the substructure (left) and superstructure (right) under buckling constraints for different values of the aspect angles (respectively β or α) and different values of the parameter η .

Corollary 2.4.6. *Suppose buckling constraints are considered in both the superstructure and substructure bridge designs. Then buckling is indeed the mode of failure if the following inequalities hold:*

$$\frac{F}{L^2} < \tan \alpha \sqrt{1 + \tan^2 \alpha} \left(\frac{4\sigma_b^2}{\pi E_b} \right), \quad \text{if } : \bar{\eta}_{\alpha\beta} < 1, \quad (2.62)$$

$$\frac{F}{L^2} < \frac{\tan^2 \beta}{2} \left(\frac{4\sigma_b^2}{\pi E_b} \right), \quad \text{if } : \bar{\eta}_{\alpha\beta} > 1, \quad (2.63)$$

where:

$$\bar{\eta}_{\alpha\beta} = \frac{2 \tan \alpha \sqrt{1 + \tan^2 \alpha}}{\tan^2 \beta}. \quad (2.64)$$

In addition, if the following inequality holds:

2. ANALYTIC RESULTS ON THE OPTIMAL DESIGN OF TENSEGRITY BRIDGES

$$\eta > \eta_{\alpha\beta} = \frac{-(\tan \alpha)^{(3/2)} \tan \beta + (1 + \tan^2 \beta) \sqrt{\tan \alpha}}{2(1 + \tan^2 \beta)^{(5/4)} \tan \beta - \sqrt{2} \tan^3 \beta \sqrt{\tan \alpha}}, \quad (2.65)$$

then the minimal mass of the substructure bridge is less than the minimal mass of the superstructure bridge. (The minimal mass of the nominal bridge reduces to substructure only. If $\eta = \eta_{\alpha\beta}$, (2.62) or (2.63) hold, then the minimal mass of the substructure is equal to the minimal mass of the superstructure. (The minimal mass of the nominal bridge reduces to either superstructure or substructure only). If $\eta < \eta_{\alpha\beta}$, and (2.62) or (2.63) hold, then the minimal mass of the superstructure is less than the minimal mass of the substructure. (The minimal mass bridge is superstructure only).

Proof. Under buckling constraints, if the design has the property $f_{b,i}/b_i^2 < 4\sigma_b^2/(\pi E_b)$, then this guarantees that buckling is the mode of failure in bar b_i , and the yielding constraints are also satisfied (see Lemma 4.2.1). For the *superstructure*, assuming the force f_1 (2.20) and the length b_1 (2.18), then Lemma 4.2.1 reduces to (2.62). Similarly, for the *substructure*, assuming the force f_2 (2.20) and the length b_2 (2.18), then Lemma (4.2.1) reduces to (2.63). Buckling is the mode of failure of *superstructure* and *substructure* designs if both (2.62) and (2.63) hold or, equivalently, if the following holds:

$$\frac{F}{L^2} < \min \left[\tan \alpha \sqrt{1 + \tan^2 \alpha}, \frac{\tan^2 \beta}{2} \right] \left(\frac{4\sigma_b^2}{\pi E_b} \right). \quad (2.66)$$

From the inequality $\bar{\eta}_{\alpha\beta} > 1$ we obtain conditions (2.62) and (2.63).

The mass of the *substructure* is shown to be less than the mass of the *superstructure* if $\eta > \eta_{\alpha\beta}$, a result that follows by taking the ratio between the mass of the *superstructure* (2.53) and the mass of the *substructure* (2.61). \square

The left contour plot in Fig. 2.9 shows values of the function $\bar{\eta}_{\alpha\beta}$ for any

2. ANALYTIC RESULTS ON THE OPTIMAL DESIGN OF TENSEGRITY BRIDGES

angles α and β , indicating the range of α and β for which $\bar{\eta}_{\alpha\beta} > 1$, which in turn chooses the appropriate condition (2.62) or (2.63). The trend of the function $\eta_{\alpha\beta}$ is shown in the right contour plot of Fig. 2.9. The physical parameter η is a positive number and Fig. 2.9 show the region for which the quantity $\eta_{\alpha\beta}$ is a negative number. We have shown earlier (2.51) that the approximated $\alpha = 26.56$ degrees. Furthermore Fig 2.8 illustrates that $\alpha = 26.56$ degrees is very close to the actual minimum over a very large range of the physical parameter η . Therefore, from the right plot in Fig 2.9 any α in the range of the optimal value (26 degrees) yields $\eta > \eta(\alpha, \beta)$. Hence, the *substructure* bridge has the minimal mass.

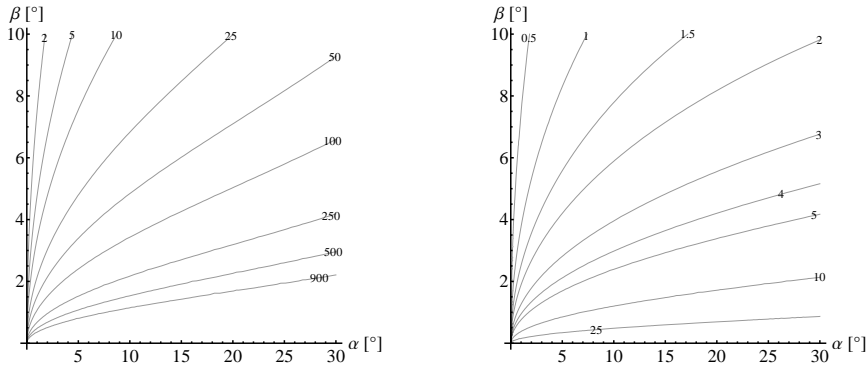


Figure 2.9: Contour plots of the functions $\bar{\eta}_{\alpha\beta}$, (left, Eq. 2.64) and $\eta_{\alpha\beta}$, (right, Eq. 2.65) for different values of the aspect angles α and β

2.5 Mass of Bridges of Complexity $(n, p, q) = (1, p, q)$, Under Yielding and Buckling Constraints

Now we consider more complex structures by increasing p, q . This section finds the minimal mass of *substructure*, and *superstructure* bridges with complexity $(n, p, q) = (1, p, q)$, for any p and q greater than 1.

2. ANALYTIC RESULTS ON THE OPTIMAL DESIGN OF TENSEGRITY BRIDGES

2.5.1 *Superstructure Bridge with Complexity* $(n, p, q) = (1, 0, q > 1)$

Refer to Fig. 2.10 for the notation. The angle between the bars is:

$$\gamma = \frac{2\alpha}{q-1}. \quad (2.67)$$

The lengths of the bars and cables are:

$$s_0 = \frac{L}{2}, \quad s_1 = s_2 = \frac{L}{2} \sin \alpha, \quad b_1 = \frac{L}{2} \cos \alpha, \quad b_2 = L \sin \alpha \sin \left(\frac{\alpha}{q-1} \right). \quad (2.68)$$

From the equilibrium equations, we obtain the following relations for the forces:

$$t_2 = \frac{F}{2 \left[\cos \alpha + \sin \left(\frac{\alpha(q-2)}{q-1} \right) / \sin \left(\frac{\alpha}{q-1} \right) \right]}, \quad t_1 = \frac{t_2}{2}, \quad (2.69)$$

$$f_2 = \frac{t_2}{2 \sin \left(\frac{\alpha}{q-1} \right)}, \quad f_1 = f_2 \cos \left(\frac{\alpha}{q-1} \right). \quad (2.70)$$

Theorem 2.5.1. *Consider a superstructure bridge, of total span L , topology*

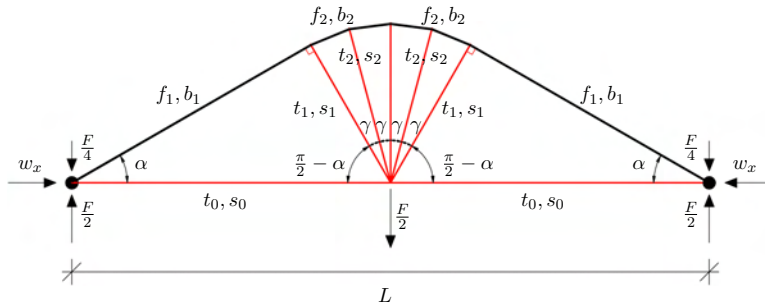


Figure 2.10: Notations for forces and lengths of bars and cables for a *superstructure* with complexity $n = 1$ and $q > 1$.

2. ANALYTIC RESULTS ON THE OPTIMAL DESIGN OF TENSEGRITY BRIDGES

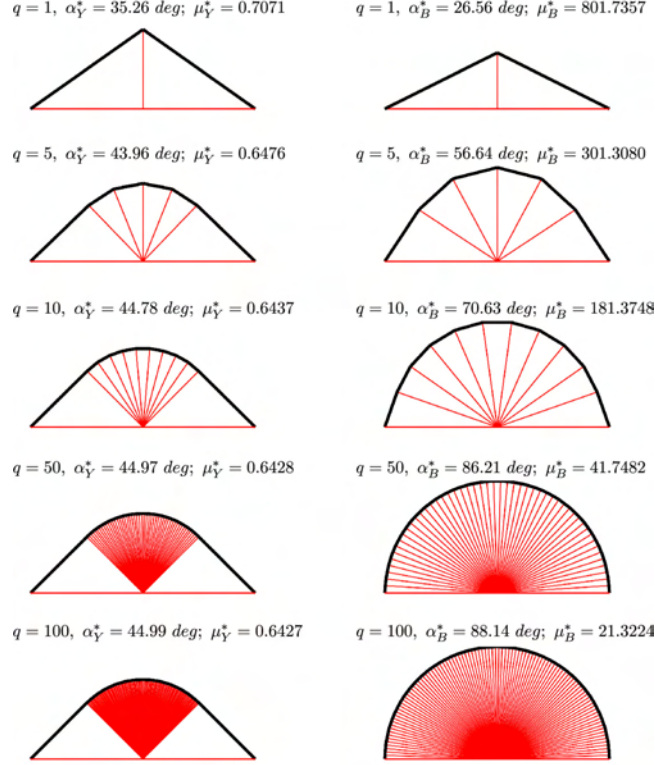


Figure 2.11: Optimal topologies of *superstructure* bridges with complexity $(n, p, q) = (1, 0, q \rightarrow \infty)$ under yielding constraints (left) and buckling constraints (right) for different q , (steel for bars and cables, $F = 1$ N, $L = 1$ m).

defined by (2.68), with complexity $(n = 1, q > 1)$, Fig. 2.10. At the yield condition under a vertical load F the dimensionless total mass is:

$$\mu_Y(\alpha, q) = \frac{t_0}{F} + \frac{(q-1) \sin \alpha}{4 \left[\cos \alpha + \sin \left(\frac{\alpha(q-2)}{q-1} \right) / \sin \left(\frac{\alpha}{q-1} \right) \right]} + \frac{\varrho (q-1) \sin \alpha \sin \left(\frac{\alpha}{q-1} \right) + \cos \alpha \cos \left(\frac{\alpha}{q-1} \right)}{4 \sin \left(\frac{\alpha}{q-1} \right) \cos \alpha + \sin \left(\frac{\alpha(q-2)}{q-1} \right)}. \quad (2.71)$$

2. ANALYTIC RESULTS ON THE OPTIMAL DESIGN OF TENSEGRITY BRIDGES

Proof. The total mass of the cables is:

$$m_s = \frac{\rho_s}{\sigma_s} \sum_{i=1}^{n_s} t_i s_i = \frac{\rho_s}{\sigma_s} (2t_0 s_0 + 2t_1 s_1 + (p-2)t_2 s_2). \quad (2.72)$$

Substituting (2.68) and (2.70) into m_s we get:

$$m_s = \frac{\rho_s}{\sigma_s} \left(t_0 L + \frac{FL}{4} \frac{(q-1) \sin \alpha}{\left(\cos \alpha + \sin \left(\frac{\alpha(q-2)}{q-1} \right) / \sin \left(\frac{\alpha}{q-1} \right) \right)} \right). \quad (2.73)$$

The total mass of bars is:

$$m_b = \frac{\rho_b}{\sigma_b} \sum_{i=1}^{n_b} f_i b_i = \frac{\rho_b}{\sigma_b} (2f_1 b_1 + (p-1)f_2 b_2). \quad (2.74)$$

Substituting (2.68) and (2.70) into m_b we get:

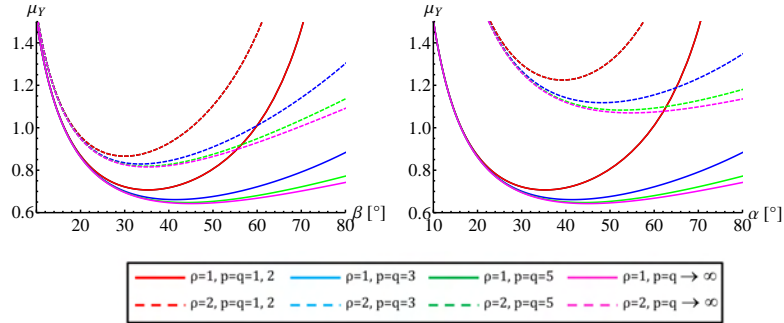


Figure 2.12: Mass curves under yielding constraints of *substructures* (left) and *superstructures* (right) vs. aspect angle β (left) and α (right) for different complexity p (left) and q (right), ($F = 1 N$, $L = 1 m$).

2. ANALYTIC RESULTS ON THE OPTIMAL DESIGN OF TENSEGRITY BRIDGES

$$m_b = \frac{\varrho_b FL}{4\sigma_b} \frac{(q-1) \sin \alpha \sin\left(\frac{\alpha}{q-1}\right) + \cos \alpha \cos\left(\frac{\alpha}{q-1}\right)}{\sin\left(\frac{\alpha}{q-1}\right) \cos \alpha + \sin\left(\frac{\alpha(q-2)}{q-1}\right)}. \quad (2.75)$$

Normalizing m_s and m_b and summing we get (2.71). □

Corollary 2.5.1. *The minimal mass in (2.71) is achieved at infinite complexity $q \rightarrow \infty$ and $t_0 = 0$. Then the minimal mass at yielding for a superstructure bridge is:*

$$\mu_Y^*(\alpha_Y^*, q^*) = \frac{1}{4} [(1 + \varrho) \arctan \sqrt{\varrho} + \sqrt{\varrho}], \quad (2.76)$$

where $q^* \rightarrow \infty$ and the optimal angle α_Y^* is:

$$\alpha_Y^* = \arctan \sqrt{\varrho}. \quad (2.77)$$

The left side of Fig. 2.11 illustrates *superstructure* bridges as $q \rightarrow \infty$, where masses are given for any q by (2.71).

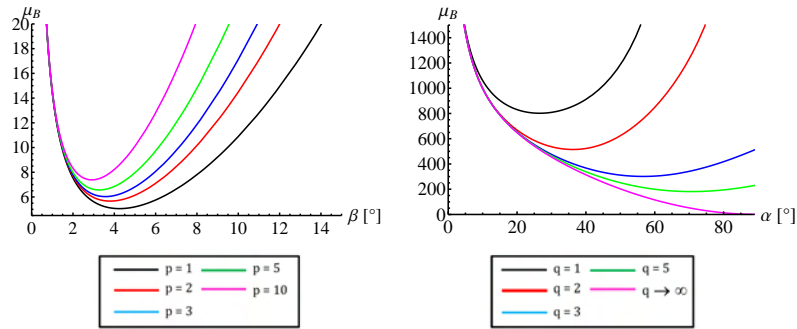


Figure 2.13: Mass curves under buckling constraints of *substructures* (left) and *superstructures* (right) vs. aspect angle β (left) and α (right) for different complexity p (left) and q (right), (steel bars and cables, $F = 1 \text{ N}$, $L = 1 \text{ m}$).

2. ANALYTIC RESULTS ON THE OPTIMAL DESIGN OF TENSEGRITY BRIDGES

Proof. Substitute $q \rightarrow \infty$ into Eq. (2.71) to obtain:

$$\mu_Y^*(\alpha, q^* \rightarrow \infty) = \frac{\alpha}{4} (1 + \varrho) + \frac{\varrho}{4 \tan \alpha}. \quad (2.78)$$

The value of α that minimizes (2.78) is (2.77). See Fig. 2.12 to see how mass (2.71) varies with q and α . The optimal q^* is deduced from the plot of Fig. 2.12 and the optimal angle is computed analytically in Eq. (2.77). \square

Theorem 2.5.2. Consider a superstructure bridge with topology (2.68), and complexity $(n, p, q) = (1, 0, q > 1)$, see Fig. 2.10. At the buckling condition the dimensionless total mass is:

$$\mu_B(\alpha, q) = \frac{t_0}{F} + \frac{(q-1) \sin \alpha}{4 \left[\cos \alpha + \sin \left(\frac{\alpha(q-2)}{q-1} \right) / \sin \left(\frac{\alpha}{q-1} \right) \right]} + \eta \left[\frac{\cos^2 \alpha \sqrt{\cos \left(\frac{\alpha}{q-1} \right) + 2(q-1) \sin^2 \alpha \sin^2 \left(\frac{\alpha}{q-1} \right)}}{2 \sqrt{\sin \left(\frac{\alpha}{q-1} \right) \cos \alpha + \sin \left(\frac{\alpha(q-2)}{q-1} \right)}} \right]. \quad (2.79)$$

Proof. The total mass of the cables has been already computed in the proof of Theorem 2.5.1.

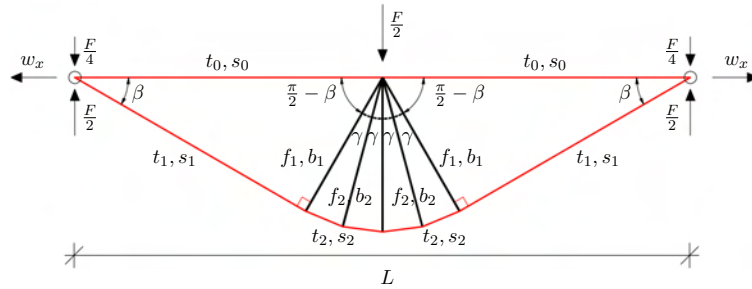


Figure 2.14: Notations for forces and lengths of bars and cables for a *substructure* with complexity $n = 1$ and $p > 1$.

2. ANALYTIC RESULTS ON THE OPTIMAL DESIGN OF TENSEGRITY BRIDGES

The total mass of bars is:

$$m_b = \sum_{i=1}^{n_b} 2\rho_b b_i^2 \sqrt{\frac{f_i}{\pi E_b}} = 4\rho_b b_1^2 \sqrt{\frac{f_1}{\pi E_b}} + 2(p-1)\rho_b b_2^2 \sqrt{\frac{f_2}{\pi E_b}}. \quad (2.80)$$

Substituting (2.68) and (2.70) into m_b we get:

$$m_b = \frac{\rho_b L^2 \sqrt{F}}{\sqrt{\pi E_b}} \left[\frac{\cos^2 \alpha \sqrt{\cos\left(\frac{\alpha}{q-1}\right)} + 2(q-1) \sin^2 \alpha \sin^2\left(\frac{\alpha}{q-1}\right)}{2\sqrt{\sin\left(\frac{\alpha}{p-1}\right) \cos \alpha + \sin\left(\frac{\alpha(q-2)}{q-1}\right)}} \right]. \quad (2.81)$$

Normalizing m_s and m_b and summing we get (2.79). □

Corollary 2.5.2. *The minimal mass superstructure is achieved for $q \rightarrow \infty$ and $t_0 = 0$, leading to the following mass:*

$$\mu_B(\alpha, q \rightarrow \infty) = \frac{\alpha}{4} + \frac{\eta \cos^2 \alpha}{2\sqrt{\sin \alpha}}. \quad (2.82)$$

Proof. The plot in Fig. 2.13 vs. α for different q shows that (2.79) has a global minimum value at $q \rightarrow \infty$. □

It is important to consider that, for the solution $q \rightarrow \infty$, buckling is not the mode of failure since the lengths of the bars approaches zero. Also note that at $\alpha = 90 \text{ deg}$, $\mu_B = \pi/8$.

The left side of Fig. 2.11 shows a sequence of *superstructures* under yielding constraints, as q increases. From (2.71) the mass is minimized at $q \rightarrow \infty$ and $\alpha_Y^* = 45 \text{ deg}$ ($\rho = 1$). The right side of Fig. 2.11 shows a sequence of *superstructures* under buckling constraints, as q increases. From plot in Fig.

2. ANALYTIC RESULTS ON THE OPTIMAL DESIGN OF TENSEGRITY BRIDGES

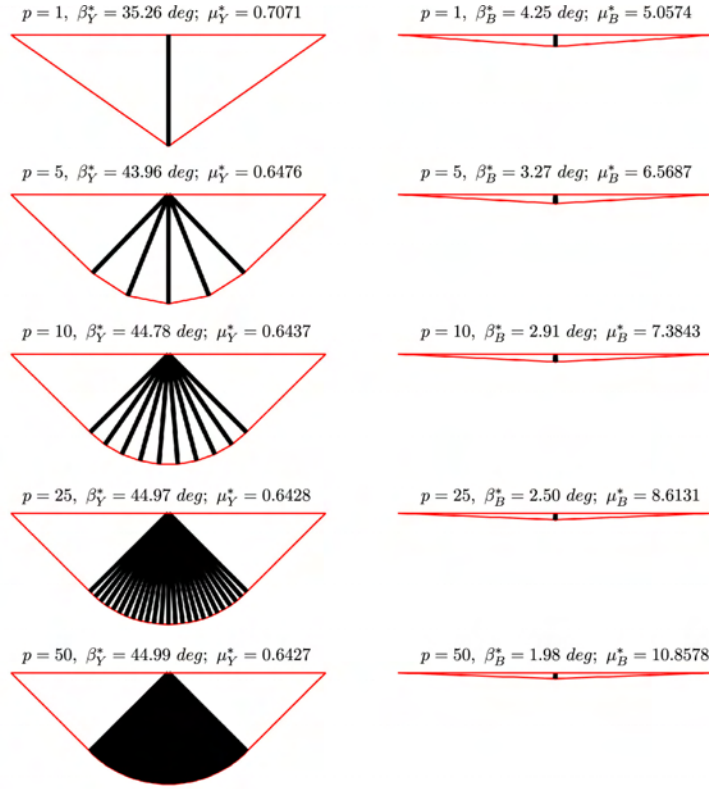


Figure 2.15: Optimal topologies of *substructure* bridges with $n = 1$ under yielding constraints (left) and buckling constraints (right) for different p , (steel for bars and cables, $F = 1 \text{ N}$, $L = 1 \text{ m}$).

2.13 the mass is minimized at $\alpha = 90 \text{ deg}$ for $q = \infty$ ($\eta = 857.71$, same steel/steel material as above).

2.5.2 *Substructure* Bridge with Complexity $(n, p, q) = (1, p > 1, 0)$

Refer to Fig. 2.14 for the notation. The angle between the bars is:

$$\gamma = \frac{2\beta}{p-1}. \quad (2.83)$$

2. ANALYTIC RESULTS ON THE OPTIMAL DESIGN OF TENSEGRITY BRIDGES

The lengths of the bars and cables are:

$$s_0 = \frac{L}{2}, \quad s_1 = \frac{L}{2} \cos \beta, \quad s_2 = L \sin \beta \sin \left(\frac{\beta}{p-1} \right), \quad b_1 = b_2 = \frac{L}{2} \sin \beta. \quad (2.84)$$

From the equilibrium equations, we obtain the following relations for the forces:

$$f_1 = \frac{F}{4 \left[\cos \beta + \sin \left(\frac{\beta(p-2)}{p-1} \right) / \sin \left(\frac{\beta}{p-1} \right) \right]}, \quad f_2 = 2f_1, \quad (2.85)$$

$$t_2 = \frac{f_2}{2 \sin \left(\frac{\beta}{p-1} \right)}, \quad t_1 = t_2 \cos \left(\frac{\beta}{p-1} \right). \quad (2.86)$$

Theorem 2.5.3. *Consider a substructure bridge with topology described by (2.84), with complexity $(n, p, q) = (1, p, 0)$ (Fig. 2.14). At the yield condition the dimensionless total mass is:*

$$\mu_Y(\beta, p) = \frac{t_0}{F} + \frac{1}{4} \left[\frac{(p-1) \sin \beta \sin \left(\frac{\beta}{p-1} \right) + \cos \beta \cos \left(\frac{\beta}{p-1} \right)}{\cos \beta \sin \left(\frac{\beta}{p-1} \right) + \sin \left(\frac{\beta(p-2)}{p-1} \right)} \right] + \frac{(p-1) \sin \beta}{4 \left[\cos \beta + \sin \left(\frac{\beta(p-2)}{p-1} \right) / \sin \left(\frac{\beta}{p-1} \right) \right]}. \quad (2.87)$$

Proof. Observing that the *substructure* bridge of the present theorem is the *dual* structure of the *superstructure* bridge of Theorem 2.5.1, we can easily obtain the proof of this theorem. □

Corollary 2.5.3. *The minimal mass in (2.87) is achieved at infinite complexity $p \rightarrow \infty$ and $t_0 = 0$. The minimal mass at yielding for a substructure bridge is:*

2. ANALYTIC RESULTS ON THE OPTIMAL DESIGN OF TENSEGRITY BRIDGES

$$\mu_Y^*(\beta_Y^*, p^*) = \frac{1}{4} \left[\sqrt{\varrho} + (1 + \varrho) \arctan \frac{1}{\sqrt{\varrho}} \right], \quad (2.88)$$

where $p^* \rightarrow \infty$ and the optimal angle β_Y^* is:

$$\beta_Y^* = \arctan \left(\frac{1}{\sqrt{\varrho}} \right). \quad (2.89)$$

Proof. Substitute $p \rightarrow \infty$ into Eq. (2.87) to obtain:

$$\mu_Y^*(\beta, p^* \rightarrow \infty) = \frac{\beta}{4} (1 + \varrho) + \frac{1}{4 \tan \beta}. \quad (2.90)$$

The value of β that minimizes (2.90) is (2.89). Fig. 2.12 shows how mass (2.87) varies with p and β . The optimal p^* is deduced from the plot of Fig. 2.12 and the optimal angle is computed analytically in Eq. (2.89). □

Theorem 2.5.4. *Consider a substructure bridge with topology defined by (2.84), with complexity $(n, p, q) = (1, p, 0)$, See Fig. 2.14. At the buckling condition the dimensionless total mass is minimized at $p = 2$ and $t_0 = 0$, where:*

$$\mu_B(\beta, p = 2) = \frac{1 + \tan^2 \beta}{4 \tan \beta} + \frac{\eta}{2} \frac{\tan^2 \beta}{(1 + \tan^2 \beta)^{3/4}}. \quad (2.91)$$

Corollary 2.5.4. *The minimal mass substructure is achieved for $p = 1$.*

Proof. The mass of a substructure with topology of $n = 1$ defined by (2.84), for a general $p > 1$ is:

2. ANALYTIC RESULTS ON THE OPTIMAL DESIGN OF TENSEGRITY BRIDGES

$$\mu_B(\beta, p) = \frac{t_0}{F} + \frac{1}{4} \left[\frac{(p-1) \sin \beta \sin\left(\frac{\beta}{p-1}\right) + \cos \beta \cos\left(\frac{\beta}{p-1}\right)}{\cos \beta \sin\left(\frac{\beta}{p-1}\right) + \sin\left(\frac{\beta(p-2)}{p-1}\right)} \right] + \frac{\eta}{2\sqrt{2}} \frac{(p-2 + \sqrt{2}) \sin^2 \beta}{\sqrt{\cos \beta + \sin\left(\frac{\beta(p-2)}{p-1}\right) / \sin\left(\frac{\beta}{p-1}\right)}}. \quad (2.92)$$

The plot of (2.92) in Fig. 2.13 vs. β for different p shows that (2.92) has a minimum value at $p = 2$. However, the mass at $p = 2$, (2.91), is larger than the mass (2.57) at $p = 1$ from Corollary 2.4.5.

□

The left side of Fig. 2.15 shows a sequence of *substructures* under yielding constraints, as p increases. From (2.87) the mass is minimized at $p \rightarrow \infty$ and $\beta_Y^* = 45 \text{ deg}$ ($\rho = 1$). The right side of Fig. 2.15 shows a sequence of *substructures* under buckling constraints, as p increases. From plot in Fig. 2.13 the mass is minimized at $\beta = 90 \text{ deg}$ for $p = 1$ ($\eta = 857.71$, same steel/steel material as above).

Theorem 2.5.5. *A minimal mass superstructure constrained against yielding with hinge/roller boundary conditions, has the same optimal topology as a minimal mass superstructure constrained against buckling and hinge/hinge boundary conditions.*

Proof. [20] proved that the minimal mass structure constrained against yielding with hinge/roller boundary conditions has the topology of the right side of Fig. 2.11 as $q \rightarrow \infty$ and $\alpha \rightarrow 90 \text{ deg}$. Theorem 2.5.2 provides the same topology for hinge/hinge constraints.

□

Theorem 2.5.6. *The minimal mass nominal bridge constrained against yielding is obtained combining the optimal superstructure topology (Fig. 2.11, left*

2. ANALYTIC RESULTS ON THE OPTIMAL DESIGN OF TENSEGRITY BRIDGES

side as $q \rightarrow \infty$) with the optimal substructure topology (Fig. 2.11, left side as $p \rightarrow \infty$).

Proof. [20] obtained these same results by starting with a continuum and optimizing the shape.

□

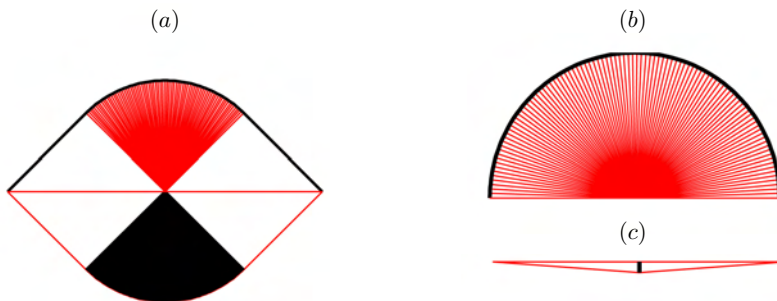


Figure 2.16: Minimal mass bridges under (a) yielding constrained *nominal* bridges, (b) buckling constrained *superstructure* bridge and (c) buckling constrained *substructure* bridge.

Fig. 2.16(a) illustrates the minimal mass *nominal* bridge under yielding constraints (Theorem 2.5.5), leading to complexity $(n, p, q) = (1, \infty, \infty)$. Fig. 2.16(b) illustrates the minimal mass *superstructure* bridge under buckling constraints, leading to complexity $(n, p, q) = (1, 0, q \rightarrow \infty)$. Fig. 2.16(c) illustrates the minimal mass *substructure* bridge under buckling constraints, leading to complexity $(n, p, q) = (1, 1, 0)$.

2.6 Mass of Bridges of Complexity $(n, p, q) = (n, 1 \text{ or } 0, 1 \text{ or } 0)$

This section finds the minimal mass of a tensegrity bridge of any complexity n . As in previous sections, no deck mass is yet added til the next section.

2. ANALYTIC RESULTS ON THE OPTIMAL DESIGN OF TENSEGRITY BRIDGES

The total external load is a given constant force F . Dividing the span into 2^n equal sections, creates nodes at each section that carries load f , given by,

$$f = \frac{F}{2^n}. \quad (2.93)$$

Distributing the total external load equally among the number of spans (2^n) of the subsections requires internal nodes to carry load $f = F/2^n$, and the external nodes of the deck to carry load $f/2$.

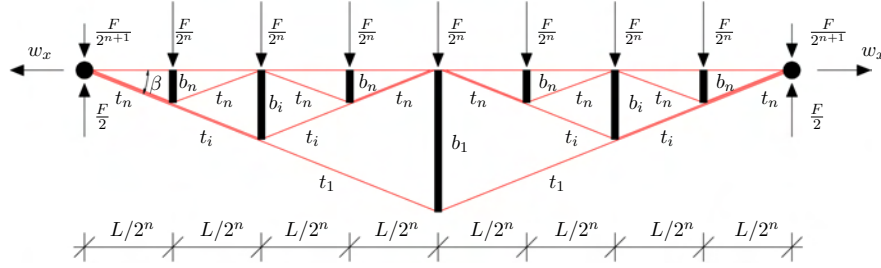


Figure 2.17: Adopted notations for forces and lengths of bars and cables for a substructure with generic complexity n and $p = 1$.

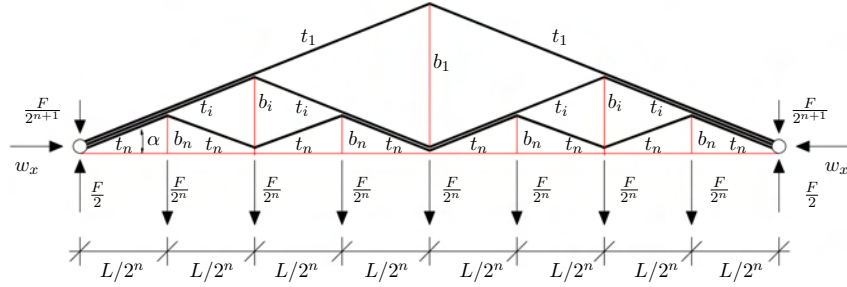


Figure 2.18: Adopted notations for forces and lengths of bars and cables for a superstructure with complexity $(n, p) = (n, 1)$

2.6.1 Substructure Bridge with Complexity $(n, p, q) = (n, 1, 0)$

In this case, we make use of the notation illustrated in Fig. 4.2 in which complexity p is fixed to be one. Since n is the number of self-similar iteration

2. ANALYTIC RESULTS ON THE OPTIMAL DESIGN OF TENSEGRITY BRIDGES

of the basic module of Fig. 2.2c at different scales, it can be defined n orders of bars and cables. The length of the generic i^{th} bar and the length of the generic i^{th} cables are,

$$b_i = \frac{L}{2^i} \tan \beta, \quad i = 1 - n, \quad (2.94)$$

$$s_i = \frac{L}{2^i \cos \beta}, \quad i = 1 - n. \quad (2.95)$$

From the equilibrium conditions, the axial force in each bar and the axial force in each cable are given by,

$$f_{bi} = \frac{F}{2^i}, \quad (2.96)$$

$$t_{si} = \frac{F}{2^{(1+i)} \sin \beta}. \quad (2.97)$$

Theorem 2.6.1. *Consider a substructure bridge with topology defined by (4.5), (4.6), (4.15) and (4.16), with complexity $(n, p, q) = (n, 1, 0)$, see Fig. 4.2. The minimal mass design under only yielding constraints is given by the following aspect angle:*

$$\beta_Y^* = \arctan \left(\frac{1}{\sqrt{1 + \varrho}} \right), \quad (2.98)$$

which corresponds to the following dimensionless minimal mass

2. ANALYTIC RESULTS ON THE OPTIMAL DESIGN OF TENSEGRITY BRIDGES

$$\mu_Y^* = \left(1 - \frac{1}{2^n}\right) \sqrt{1 + \varrho}. \quad (2.99)$$

Proof. Observing the multiscale structure of Fig. 4.2 it's clear that the number of bars and the number of cables of i^{th} order are

$$n_{si} = 2^i, \quad n_{bi} = 2^{i-1}. \quad (2.100)$$

The total mass of the structure is:

$$m_Y = \frac{\varrho_s}{\sigma_s} \sum_{i=1}^n n_{si} t_{si} s_i + \frac{\varrho_b}{\sigma_b} \sum_{i=1}^n n_{bi} f_{bi} b_i. \quad (2.101)$$

Substituting (4.15), (4.16), (2.96), (2.97) and (4.17) into (2.101) yields,

$$m_Y = \frac{FL}{2} \left(\sum_{i=1}^n \frac{1}{2^i} \right) \left(\frac{\varrho_s}{\sigma_s} \frac{1}{\sin \beta \cos \beta} + \frac{\varrho_b}{\sigma_b} \tan \beta \right). \quad (2.102)$$

Using the following identities in (2.102),

$$\sum_{i=1}^n \frac{1}{2^i} = \left(1 - \frac{1}{2^n}\right), \quad \frac{1}{\sin \beta \cos \beta} = \frac{1 + \tan^2 \beta}{\tan \beta}, \quad (2.103)$$

we obtain:

$$m_Y = \frac{FL}{2} \left(1 - \frac{1}{2^n}\right) \left[\frac{\varrho_s (1 + \tan^2 \beta)}{\varrho_b \tan \beta} + \frac{\varrho_b}{\sigma_b} \tan \beta \right]. \quad (2.104)$$

Switching to the dimensionless mass defined in (4.9) we have:

2. ANALYTIC RESULTS ON THE OPTIMAL DESIGN OF TENSEGRITY BRIDGES

$$\mu_Y = \frac{1}{2} \left(1 - \frac{1}{2^n}\right) \left[\frac{(1 + \tan^2 \beta)}{\tan \beta} + \varrho \tan \beta \right]. \quad (2.105)$$

The solution for minimal mass can be achieved from,

$$\frac{\partial \mu_Y}{\partial \tan \beta} = \frac{1}{2} \left(1 - \frac{1}{2^n}\right) \left[-\frac{(\tan^2 \beta + 1)}{\tan^2 \beta} + 2 + \varrho \right] = 0, \quad (2.106)$$

yielding the optimal angle of (2.98). Substituting it into (2.105) concludes the proof. □

Note from (2.35) and (2.98) that the optimal angle β does not depend upon the choice of n . The minimal mass solution under yielding constraints depends only on the material choice ϱ (2.14), and the complexity parameter n . Note that, since the total external force F is a specified constant, the optimum complexity is $n = 1$. However if the total vertical force depends upon n as it will in the next section dealing with massive decks, or with massive joints, then the optimal complexity will be shown to be $n > 1$.

Theorem 2.6.2. *Consider a substructure bridge with topology defined by (4.5), (4.6), (4.15) and (4.16), with complexity $(n, p, q) = (n, 1, 0)$, see Fig. 4.2. The minimal mass design under yielding and buckling constraints, is given by the following aspect angle:*

$$\beta_B^* = \arctan \left\{ \frac{1}{12\alpha_2\eta} \left[\alpha_3 + \alpha_1 \left(\frac{\alpha_1}{\alpha_3} - 1 \right) \right] \right\}. \quad (2.107)$$

which corresponds to the following dimensionless minimal mass:

2. ANALYTIC RESULTS ON THE OPTIMAL DESIGN OF TENSEGRITY BRIDGES

$$\mu_B^* = \alpha_1 \frac{1 + \tan^2 \beta_B^*}{2 \tan \beta_B^*} + \eta \alpha_2 \tan^2 \beta_B^*, \quad (2.108)$$

where:

$$\alpha_1 = \left(1 - \frac{1}{2^n}\right), \quad (2.109)$$

$$\alpha_2 = \left(\frac{1 + 2\sqrt{2}}{7}\right) \left(1 - \frac{1}{2^{3n/2}}\right), \quad (2.110)$$

$$\alpha_3 = \left(216\alpha_1\alpha_2^2\eta^2 - \alpha_1^3 + 12\sqrt{324\alpha_1^2\alpha_2^4\eta^4 - 3\alpha_1^4\alpha_2^2\eta^2}\right)^{1/3}. \quad (2.111)$$

Proof. The total mass of cables is given by,

$$m_s = \sum_{i=1}^n \frac{\rho_s}{\sigma_s} n_{si} t_{si} s_i. \quad (2.112)$$

Substituting (4.16), (2.97), (4.17) into (2.112) and making use of identities (2.103),

$$m_s = \frac{FL}{2} \frac{\rho_s}{\sigma_s} \left(\frac{1 + \tan^2 \beta}{\tan \beta}\right) \left(1 - \frac{1}{2^n}\right). \quad (2.113)$$

This corresponds to the following normalized mass

2. ANALYTIC RESULTS ON THE OPTIMAL DESIGN OF TENSEGRITY BRIDGES

$$\mu_s = \left(\frac{1 + \tan^2 \beta}{2 \tan \beta} \right) \left(1 - \frac{1}{2^n} \right). \quad (2.114)$$

The total mass of bars, making use of (4.2), is

$$m_b = \sum_{i=1}^n n_{bi} m_{bi} = \sum_{i=1}^n n_{bi} \frac{2Q_b}{\sqrt{\pi E_b}} b_i^2 \sqrt{f_i}. \quad (2.115)$$

Substituting (4.15), (4.17) and (2.96) into (2.115) yields

$$m_b = \frac{\rho_b L^2 \sqrt{F}}{\sqrt{\pi E_b}} \tan^2 \beta \sum_{i=1}^n \frac{1}{2^{3i/2}}. \quad (2.116)$$

Since

$$\sum_{i=1}^n \frac{1}{2^{3i/2}} = \left(\frac{1 + 2\sqrt{2}}{7} \right) \left(1 - \frac{1}{2^{3n/2}} \right), \quad (2.117)$$

normalizing we get the following dimensionless mass of bars,

$$\mu_b = \eta \tan^2 \beta \left(\frac{1 + 2\sqrt{2}}{7} \right) \left(1 - \frac{1}{2^{3n/2}} \right). \quad (2.118)$$

The total mass is then the sum of (4.25) and (4.26) and introducing constants α_1 and α_2 given in (2.109) and (2.110):

$$\mu_B = \mu_s + \mu_b = \alpha_1 \frac{1 + \tan^2 \beta}{2 \tan \beta} + \eta \alpha_2 \tan^2 \beta. \quad (2.119)$$

2. ANALYTIC RESULTS ON THE OPTIMAL DESIGN OF TENSEGRITY BRIDGES

The solution for minimal mass can be achieved from,

$$\frac{\partial \mu_B}{\partial \tan \beta} = \alpha_1 \left(1 - \frac{1 - \tan^2 \beta}{2 \tan^2 \beta} \right) + 2\eta\alpha_2 \tan \beta = 0, \quad (2.120)$$

yielding the optimal angle (2.107) by solving the following cubic equation:

$$4 \frac{\alpha_2}{\alpha_1} \eta \tan^3 \beta + \tan^2 \beta - 1 = 0. \quad (2.121)$$

Note that the optimal angle given in (2.107) reduces to the optimal angle given in (2.56) for the particular case $n = 1$. Then, substituting (2.107) into (2.119) concludes the proof. □

2.6.2 Superstructure Bridge with Complexity $(n, p, q) = (n, 0, 1)$

In this case, we make use of the notation illustrated in Fig. 2.18 in which complexity q is fixed to be one. Since n is the number of self-similar iteration of the basic module of Fig. 2.2b at different scales, it can be defined n orders of bars and cables. The length of the generic i^{th} bar and the length of the generic i^{th} cable, for i ranging from 1 to n , are:

$$b_i = \frac{L}{2^i \cos \alpha}, \quad s_i = \frac{L}{2^i} \tan \alpha. \quad (2.122)$$

Moreover, looking at the equilibrium of each node of the structure, we found that the axial force in each bar and the axial force in each cable are given by:

$$f_{bi} = \frac{F}{2^{(1+i)} \sin \alpha}, \quad t_{si} = \frac{F}{2^i}. \quad (2.123)$$

2. ANALYTIC RESULTS ON THE OPTIMAL DESIGN OF TENSEGRITY BRIDGES

Observing the multiscale structure of Fig. 2.18 it's clear that the number of bars and the number of cables of i^{th} order are:

$$n_{si} = 2^{i-1}, \quad n_{bi} = 2^i. \quad (2.124)$$

Theorem 2.6.3. *Consider a superstructure bridge with topology defined by (4.5), (2.12), (2.173), with complexity $(n, p, q) = (n, 0, 1)$, see Fig. 2.18. The minimal mass design under yielding constraints is given by the following aspect angle:*

$$\alpha_Y^* = \arctan \left(\sqrt{\frac{\varrho}{1 + \varrho}} \right), \quad (2.125)$$

which corresponds to the following dimensionless minimal mass:

$$\mu_Y^* = \left(1 - \frac{1}{2^n} \right) \sqrt{\varrho(1 + \varrho)}. \quad (2.126)$$

Proof. The total mass of the structure is:

$$m_Y = \frac{\varrho_s}{\sigma_s} \sum_{i=1}^n n_{si} t_{si} s_i + \frac{\varrho_b}{\sigma_b} \sum_{i=1}^n n_{bi} f_{bi} b_i. \quad (2.127)$$

Substituting (2.173), (2.123), and (2.174) into (2.127) and considering positions (2.103) we get:

$$m_Y = \frac{FL}{2} \left(1 - \frac{1}{2^n} \right) \left[\frac{\varrho_s}{\sigma_s} \tan \alpha + \frac{\varrho_b}{\sigma_b} \frac{(1 + \tan^2 \alpha)}{\tan \alpha} \right]. \quad (2.128)$$

Switching to the dimensionless mass defined in (4.9) we have:

2. ANALYTIC RESULTS ON THE OPTIMAL DESIGN OF TENSEGRITY BRIDGES

$$\mu_Y = \frac{1}{2} \left(1 - \frac{1}{2^n}\right) \left[\tan \alpha + \varrho \frac{(1 + \tan^2 \alpha)}{\tan \alpha} \right]. \quad (2.129)$$

The solution for minimal mass can be achieved from,

$$\frac{\partial \mu_Y}{\partial \tan \alpha} = \frac{1}{2} \left(1 - \frac{1}{2^n}\right) \left[1 + \varrho \left(2 - \frac{1 + \tan^2 \alpha}{\tan^2 \alpha}\right) \right] = 0, \quad (2.130)$$

yielding the optimal angle of (2.125). Substituting it into (2.129) concludes the proof. □

Theorem 2.6.4. *Consider a superstructure bridge with topology defined by (4.5), (2.12), (2.173), with complexity $(n, p, q) = (n, 0, 1)$, see Fig. 2.18. The minimal mass design under yielding and buckling constraints is given by the following aspect angle:*

$$\alpha_B^* = \arctan \frac{1}{2}, \quad (2.131)$$

which corresponds to the following dimensionless minimal mass:

$$\mu_B^* = \frac{\gamma_1}{2} + \eta \gamma_2 \frac{5^{5/4}}{4}, \quad (2.132)$$

where:

$$\gamma_1 = \frac{1}{2} \left(1 - \frac{1}{2^n}\right), \quad (2.133)$$

2. ANALYTIC RESULTS ON THE OPTIMAL DESIGN OF TENSEGRITY BRIDGES

$$\gamma_2 = \sqrt{2} \left(\frac{1 + 2\sqrt{2}}{7} \right) \left(1 - \frac{1}{2^{3n/2}} \right). \quad (2.134)$$

Proof. The total mass of cables is given by:

$$m_s = \sum_{i=1}^n \frac{\rho_s}{\sigma_s} n_{si} t_{si} s_i. \quad (2.135)$$

Substituting (2.173), (2.123) and (2.174) into (2.135) and making use of position (2.103):

$$m_s = \frac{FL}{2} \frac{\rho_s}{\sigma_s} \left(1 - \frac{1}{2^n} \right) \tan \alpha. \quad (2.136)$$

That corresponds to the following normalized mass:

$$\mu_s = \frac{1}{2} \left(1 - \frac{1}{2^n} \right) \tan \alpha. \quad (2.137)$$

The total mass of bars, making use of (4.2), is:

$$m_b = \sum_{i=1}^n n_{bi} m_{bi} = \sum_{i=1}^n n_{bi} \frac{2Q_b}{\sqrt{\pi E_b}} b_i^2 \sqrt{f_i}. \quad (2.138)$$

Substituting (2.173), (2.123) and (2.174) into (2.138):

$$m_b = \frac{\sqrt{2} \rho_b L^2 \sqrt{F}}{\sqrt{\pi E_b}} \frac{1}{\cos^2 \alpha \sqrt{\sin \alpha}} \sum_{i=1}^n \frac{1}{2^{3i/2}}. \quad (2.139)$$

Since:

2. ANALYTIC RESULTS ON THE OPTIMAL DESIGN OF TENSEGRITY BRIDGES

$$\sum_{i=1}^n \frac{1}{2^{3i/2}} = \left(\frac{1+2\sqrt{2}}{7} \right) \left(1 - \frac{1}{2^{3n/2}} \right),$$

$$\frac{1}{\cos^2 \alpha} = 1 + \tan^2 \alpha, \quad \frac{1}{\sqrt{\sin \alpha}} = \frac{(1 + \tan^2 \alpha)^{1/4}}{\sqrt{\tan \alpha}}, \quad (2.140)$$

and normalizing we get the following dimensionless mass of bars:

$$\mu_b = \sqrt{2}\eta \left(\frac{1+2\sqrt{2}}{7} \right) \left(1 - \frac{1}{2^{3n/2}} \right) \frac{(1 + \tan^2 \alpha)^{5/4}}{\sqrt{\tan \alpha}}. \quad (2.141)$$

The total mass is then the sum of (2.137) and (2.141) and introducing constants γ_1 and γ_2 given in (2.133) and (2.134):

$$\mu_B = \mu_s + \mu_b = \gamma_1 \tan \alpha + \eta\gamma_2 \frac{(1 + \tan^2 \alpha)^{5/4}}{\sqrt{\tan \alpha}}. \quad (2.142)$$

The solution for minimal mass can be achieved assuming that:

$$\gamma_1 \tan \alpha \ll \eta\gamma_2 \frac{(1 + \tan^2 \alpha)^{5/4}}{\sqrt{\tan \alpha}}. \quad (2.143)$$

So that the (2.142) becomes:

$$\bar{\mu}_B = \eta\gamma_2 \frac{(1 + \tan^2 \alpha)^{5/4}}{\sqrt{\tan \alpha}}. \quad (2.144)$$

The optimal angle can be obtained from:

$$\frac{\partial \bar{\mu}_B}{\partial \tan \alpha} = \frac{\eta}{2} \gamma_2 (1 + \tan^2 \alpha)^{(1/4)} \left(\frac{4 \tan^2 \alpha - 1}{\tan \alpha \sqrt{\tan \alpha}} \right) = 0, \quad (2.145)$$

yielding the optimal angle of (2.131). Substituting it into (2.142) concludes the proof. □

2.7 Introducing Deck and Joint Masses

In previous sections, complexity n was restricted to 1. This is appropriate only when the external loads are all applied at the midspan. Real bridges cannot tolerate such an assumption. So in this section we consider a distributed load. Part of the load is the mass of the deck that must span the distance between adjacent support structures (complexity n will add $2^n - 1$ supports). In the section 2.7.4 we will consider adding mass to make the joints, where high precision joints have less mass than rudely constructed joints.

2.7.1 Including Deck Mass

The total load that the structure must support includes the mass of the deck, which increases with the distance that must be spanned between support points of the structure design (which is determined by the choice of complexity n). We therefore consider bridges with increasing complexity n . We will show that the smallest $n = 1$ yields smallest structural mass and the largest deck mass. The required deck mass obviously approaches zero as the required deck span approaches zero, which occurs as $n \rightarrow \infty$. We will show that the mass of the deck plus the mass of the structure is minimized at a finite value of n .

The deck, as illustrated in Fig. 2.19, is composed by 2^n simply supported beams connecting the nodes on the deck. Let the deck parameters be labeled as: mass m_d , mass density ρ_d , yielding strength σ_d , width w_d , thickness t_d and length equal to:

2. ANALYTIC RESULTS ON THE OPTIMAL DESIGN OF TENSEGRITY BRIDGES

$$\ell_d = \frac{L}{2^n}. \quad (2.146)$$

The cross sectional of the deck beam has a moment of inertia equal to: $I_d = w_d t_d^3 / 12$. Each beam is assumed to be loaded by a uniformly distributed vertical load summing to the total value F and the total self weight of the deck (\mathcal{F}) ($g = 9.81 m s^{-2}$):

$$f_d = \frac{F}{L} + \frac{\mathcal{F}}{L} = \frac{F}{L} + \frac{m_d g 2^n}{L}. \quad (2.147)$$

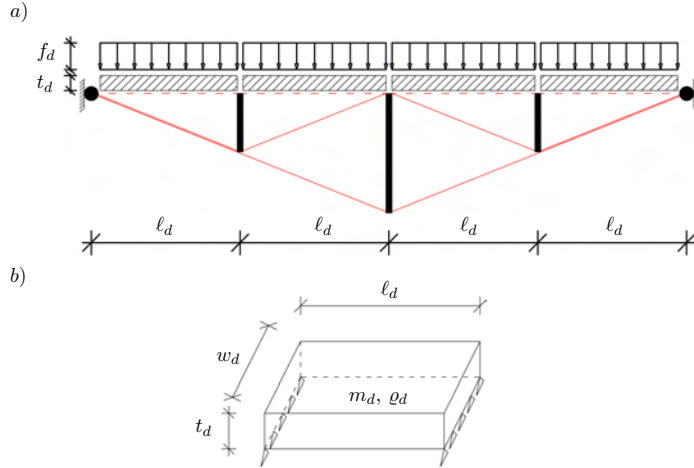


Figure 2.19: a) schematic deck system for a *substructure* with complexity $n = 3$ and $p = 1$. b) detail of a single deck module.

Assuming that the beam of a single deck section is simply supported between two consecutive nodes of the bridge, the maximum bending moment is equal to $f_d \ell_d^2 / 8$ and the maximum stress is given by Navier's equation [144]:

$$\sigma_d = \frac{3 f_d \ell_d^2}{4 w_d t_d^2}. \quad (2.148)$$

2. ANALYTIC RESULTS ON THE OPTIMAL DESIGN OF TENSEGRITY BRIDGES

The thickness of the deck beam is:

$$t_d = \frac{m_d}{\varrho_d w_d \ell_d}. \quad (2.149)$$

Substituting (2.146), (2.147) and (2.149) into (2.148) we get the following equation for the mass of one deck section:

$$m_d = \frac{c_1}{2^{3n}} + \frac{c_1}{2^{2n}} \sqrt{c_2 + \frac{1}{2^{2n}}}, \quad (2.150)$$

where:

$$c_1 = \frac{3 w_d g \varrho_d^2 L^3}{8 \sigma_d}, \quad c_2 = \frac{16 \sigma_d F}{3 w_d g^2 L^3 \varrho_d^2}. \quad (2.151)$$

Then, the normalized total mass of the deck structure is:

$$\mu_d^* = \frac{2^n m_d}{(\varrho_s/\sigma_s) FL}. \quad (2.152)$$

The total force acting on each internal node on the deck is then the sum of the force due to the external loads and the force due to the deck:

$$F_{tot} = F + 2^n m_d g. \quad (2.153)$$

2.7.2 Adding Deck Mass for A *Substructure* Bridge with Complexity $(n, p, q) = (n, 1, 0)$

In this case, we make use of the notation illustrated in Fig. 4.2 in which complexity p is fixed to be one. Complexity n is defined to be the number of self-similar iterations of the basic module of Fig. 2.2c. Each iteration

2. ANALYTIC RESULTS ON THE OPTIMAL DESIGN OF TENSEGRITY BRIDGES

$n = 1, 2, \dots$ generates different lengths of bars and cables. The lengths at the i^{th} iteration are:

$$b_i = \frac{L}{2^i} \tan \beta, \quad i = 1 - n, \quad (2.154)$$

$$s_i = \frac{L}{2^i \cos \beta}, \quad i = 1 - n. \quad (2.155)$$

Observing the multiscale structure of Fig. 4.2 it's clear that the number of bars and the number of cables at the i^{th} self-similar iteration are

$$n_{si} = 2^i, \quad n_{bi} = 2^{i-1}. \quad (2.156)$$

In this case the total force applied to the bridge structure is given by (4.14) and then the forces in each member become:

$$f_{bi} = \frac{F + 2^n m_d g}{2^i}, \quad t_{si} = \frac{F + 2^n m_d g}{2^{(1+i)} \sin \beta}. \quad (2.157)$$

Theorem 2.7.1. *Consider a substructure bridge with deck mass m_d and topology defined by (4.5), (4.6), (4.15) and (4.16), with complexity $(n, p, q) = (n, 1, 0)$, see Fig. 4.2. The minimal mass design under yielding constraints is given by:*

$$\mu_Y^* = \left(1 - \frac{1}{2^n}\right) \left(1 + 2^n g \frac{m_d}{F}\right) \sqrt{1 + \varrho}, \quad (2.158)$$

using the optimal angle:

2. ANALYTIC RESULTS ON THE OPTIMAL DESIGN OF TENSEGRITY BRIDGES

$$\beta_Y^* = \arctan\left(\frac{1}{\sqrt{1+\varrho}}\right). \quad (2.159)$$

Proof. Assuming (4.15) and (4.16) for the length of each member, (4.18) for the forces of each member, and (4.17) for the number of members, the dimensionless minimal mass becomes:

$$\mu_Y = \frac{1}{2} \left(1 + 2^n g \frac{m_d}{F}\right) \left[\frac{1}{\sin \beta \cos \beta} + \varrho \tan \beta \right] \left(\sum_{i=1}^n \frac{1}{2^i} \right). \quad (2.160)$$

yielding,

$$\mu_Y = \frac{1}{2} \left(1 - \frac{1}{2^n}\right) \left(1 + 2^n g \frac{m_d}{F}\right) \left[\frac{(1 + \tan^2 \beta)}{\tan \beta} + \varrho \tan \beta \right]. \quad (2.161)$$

The solution for minimal mass can be achieved from,

$$\frac{\partial \mu_Y}{\partial \tan \beta} = \frac{1}{2} \left(1 - \frac{1}{2^n}\right) \left(1 + 2^n g \frac{m_d}{F}\right) \left[-\frac{(\tan^2 \beta + 1)}{\tan^2 \beta} + 2 + \varrho \right] = 0, \quad (2.162)$$

yielding the optimal angle of (2.98). Substituting it into (2.160) concludes the proof. \square

Observe that (2.158) yields mass $\sqrt{1+\varrho}/2$ for complexity $n = 1$ and mass $\sqrt{1+\varrho}$ for complexity $n = \infty$. Note from (2.98), which is the same as (2.35), that the optimal angle β_Y^* does not depend upon the choice of n . Indeed, the minimal mass solution under yielding constraints (2.158) depends on the material choice ϱ (2.14), the complexity parameter n and the deck properties. Note that, since the total external force F is a specified constant, the mass

2. ANALYTIC RESULTS ON THE OPTIMAL DESIGN OF TENSEGRITY BRIDGES

is minimized by the complexity $n = 1$ if $m_d = 0$. However since m_d depends upon n , the total vertical force including deck mass depends upon n , and the optimal complexity will be shown to be $n > 1$ in that case.

Theorem 2.7.2. *Consider a substructure bridge with topology defined by (4.5), (4.6), (4.15) and (4.16), with complexity $(n, p, q) = (n, 1, 0)$. The minimal mass design under yielding and buckling constraints is given by:*

$$\mu_B^* = \beta_1 \frac{(1 + \tan^2 \beta_B^*)}{2 \tan \beta_B^*} + \eta \beta_2 \tan^2 \beta_B^*, \quad (2.163)$$

using the aspect angle:

$$\beta_B^* = \arctan \left\{ \frac{1}{12\beta_2\eta} \left[\beta_3 + \beta_1 \left(\frac{\beta_1}{\beta_3} - 1 \right) \right] \right\}, \quad (2.164)$$

where:

$$\beta_1 = \left(1 - \frac{1}{2^n} \right) \left(1 + 2^n g \frac{m_d}{F} \right), \quad (2.165)$$

$$\beta_2 = \left(\frac{1 + 2\sqrt{2}}{7} \right) \left(1 - \frac{1}{2^{3n/2}} \right) \sqrt{1 + 2^n g \frac{m_d}{F}}, \quad (2.166)$$

$$\beta_3 = \left(216\beta_1\beta_2^2\eta^2 - \beta_1^3 + 12\sqrt{324\beta_1^2\beta_2^4\eta^4 - 3\beta_1^4\beta_2^2\eta^2} \right)^{1/3}. \quad (2.167)$$

Proof. The total mass of the cables, using (4.16), (4.18) and (4.17), is given by:

2. ANALYTIC RESULTS ON THE OPTIMAL DESIGN OF TENSEGRITY BRIDGES

$$\mu_s = \left(\frac{1 + \tan^2 \beta}{2 \tan \beta} \right) \left(1 - \frac{1}{2^n} \right) \left(1 + 2^n g \frac{m_d}{F} \right). \quad (2.168)$$

Similarly, making use of (4.2), the total mass of bars is:

$$\mu_b = \eta \tan^2 \beta \left(\frac{1 + 2\sqrt{2}}{7} \right) \left(1 - \frac{1}{2^{3n/2}} \right) \sqrt{1 + 2^n g \frac{m_d}{F}}. \quad (2.169)$$

Introducing constants β_1 and β_2 given in (4.22) and (4.23), the total mass is:

$$\mu_B = \mu_s + \mu_b = \beta_1 \frac{(1 + \tan^2 \beta)}{2 \tan \beta} + \eta \beta_2 \tan^2 \beta. \quad (2.170)$$

The solution for minimal mass can be achieved from,

$$\frac{\partial \mu_B}{\partial \tan \beta} = \beta_1 \left(1 - \frac{1 - \tan^2 \beta}{2 \tan^2 \beta} \right) + 2\eta \beta_2 \tan \beta = 0, \quad (2.171)$$

yielding the optimal angle of (4.21) by solving the following cubic equation:

$$4 \frac{\beta_2}{\beta_1} \eta \tan^3 \beta + \tan^2 \beta - 1 = 0. \quad (2.172)$$

Substituting (4.21) into (4.27) concludes the proof.

□

2.7.3 Adding Deck Mass for A *Superstructure* Bridge with Complexity $(n, p, q) = (n, 0, 1)$

In this case, we make use of the notation illustrated in Fig. 2.18 in which complexity q is fixed to be one. Complexity n is the number of self-similar iterations of the basic module of Fig. 2.2b at different scales. After the i^{th} self-similar iterations, the length of the bars and cables for i ranging from 1 to n , are:

$$b_i = \frac{L}{2^i \cos \alpha}, \quad s_i = \frac{L}{2^i} \tan \alpha. \quad (2.173)$$

Observing the multiscale structure of Fig. 2.18 it's clear that the number of bars and the number of cables after the i^{th} self-similar iterations are:

$$n_{si} = 2^{i-1}, \quad n_{bi} = 2^i. \quad (2.174)$$

In this case the total force applied to the bridge structure is given by (4.14) and then the forces in each member become:

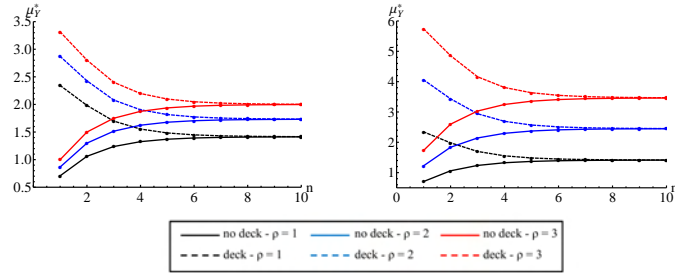


Figure 2.20: Optimal masses under yielding of the *substructures* (left) and *superstructure* (right) without deck (solid curves) and with deck (dashed curves) for different values of the complexity n and for different values of ρ , ($F = 1 N$, $w_d = 1 m$, steel deck).

2. ANALYTIC RESULTS ON THE OPTIMAL DESIGN OF TENSEGRITY BRIDGES

$$f_{bi} = \frac{F + 2^n m_d g}{2^{(i+1)} \sin \alpha}, \quad t_{si} = \frac{F + 2^n m_d g}{2^i}. \quad (2.175)$$

Theorem 2.7.3. Consider a superstructure bridge with topology defined by (4.5), (2.12), (2.173), with complexity $(n, p, q) = (n, 0, 1)$, Fig. 2.18. Under a given total vertical force (4.14), the minimal mass design under yielding constraints is given by:

$$\mu_Y^* = \left(1 - \frac{1}{2^n}\right) \left(1 + 2^n g \frac{m_d}{F}\right) \sqrt{\varrho(1 + \varrho)}, \quad (2.176)$$

using the aspect angle:

$$\alpha_Y^* = \arctan \left(\sqrt{\frac{\varrho}{1 + \varrho}} \right). \quad (2.177)$$

Proof. Substituting (2.173), (2.175), and (2.174) into (2.127) and considering positions (2.103) we get:

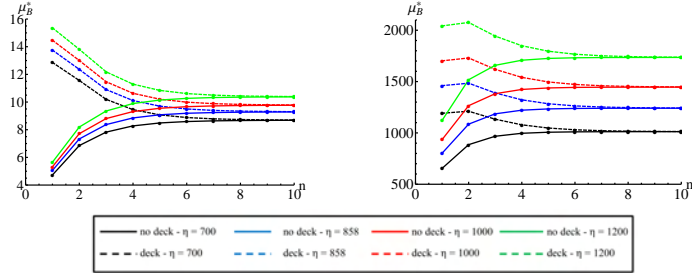


Figure 2.21: Optimal masses under buckling of the *substructures* (left) and *superstructure* (right) without deck (solid curves) and with deck (dashed curves) for different values of the complexity n and for different values of η , ($F = 1 N$, $L = w_d = 1 m$, steel deck).

2. ANALYTIC RESULTS ON THE OPTIMAL DESIGN OF TENSEGRITY BRIDGES

$$m_Y = \frac{(F + 2^n m_d g) L}{2} \left(1 - \frac{1}{2^n}\right) \left[\frac{\varrho_s}{\sigma_s} \tan \alpha + \frac{\varrho_b}{\sigma_b} \frac{(1 + \tan^2 \alpha)}{\tan \alpha} \right]. \quad (2.178)$$

Switching to the dimensionless mass defined in (4.9) we have:

$$\mu_Y = \frac{1}{2} \left(1 + 2^n g \frac{m_d}{F}\right) \left(1 - \frac{1}{2^n}\right) \left[\tan \alpha + \varrho \frac{(1 + \tan^2 \alpha)}{\tan \alpha} \right]. \quad (2.179)$$

The solution for minimal mass can be achieved from,

$$\frac{\partial \mu_Y}{\partial \tan \alpha} = \frac{1}{2} \left(1 + 2^n g \frac{m_d}{F}\right) \left(1 - \frac{1}{2^n}\right) \left[1 + \varrho \left(2 - \frac{1 + \tan^2 \alpha}{\tan^2 \alpha}\right) \right] = 0, \quad (2.180)$$

yielding the optimal angle of (2.177). Substituting it into (2.179) concludes the proof. □

Theorem 2.7.4. *Consider a superstructure bridge with topology defined by (4.5), (2.12), (2.173), and complexity $(n, p, q) = (n, 0, 1)$, see Fig. 2.18. The structure is loaded with a given total vertical force (4.14) and the minimal bar mass, subject to yield constraints is given by:*

$$\mu_B^* = \frac{\delta_1}{2} + \eta \delta_2 \frac{5^{5/4}}{4}, \quad (2.181)$$

using the aspect angle:

$$\alpha_B^* = \arctan \frac{1}{2}, \quad (2.182)$$

where:

2. ANALYTIC RESULTS ON THE OPTIMAL DESIGN OF TENSEGRITY BRIDGES

$$\delta_1 = \frac{1}{2} \left(1 + 2^n g \frac{m_d}{F} \right) \left(1 - \frac{1}{2^n} \right), \quad (2.183)$$

$$\delta_2 = \sqrt{2} \left(\frac{1 + 2\sqrt{2}}{7} \right) \sqrt{1 + 2^n g \frac{m_d}{F}} \left(1 - \frac{1}{2^{3n/2}} \right). \quad (2.184)$$

Proof. Substituting (2.173), (2.175) and (2.174) into (2.135) and making use of position (2.103):

$$m_s = \frac{(F + 2^n m_d g) L \varrho_s}{2 \sigma_s} \left(1 - \frac{1}{2^n} \right) \tan \alpha. \quad (2.185)$$

That corresponds to the following normalized mass:

$$\mu_s = \frac{1}{2} \left(1 + 2^n g \frac{m_d}{F} \right) \left(1 - \frac{1}{2^n} \right) \tan \alpha. \quad (2.186)$$

Substituting (2.173), (2.175) and (2.174) into (2.138):

$$m_b = \frac{\sqrt{2} \varrho_b L^2 \sqrt{F + 2^n m_d g}}{\sqrt{\pi E_b} \cos^2 \alpha \sqrt{\sin \alpha}} \sum_{i=1}^n \frac{1}{2^{3i/2}}. \quad (2.187)$$

Using positions (2.140) into (2.187) and normalizing we get the following dimensionless mass of bars:

$$\mu_b = \sqrt{2} \eta \sqrt{1 + 2^n g \frac{m_d}{F}} \left(\frac{1 + 2\sqrt{2}}{7} \right) \left(1 - \frac{1}{2^{3n/2}} \right) \frac{(1 + \tan^2 \alpha)^{5/4}}{\sqrt{\tan \alpha}}. \quad (2.188)$$

The total mass is then the sum of (2.186) and (2.188) and introducing con-

2. ANALYTIC RESULTS ON THE OPTIMAL DESIGN OF TENSEGRITY BRIDGES

stants δ_1 and δ_2 given in (2.183) and (2.184):

$$\mu_B = \mu_s + \mu_b = \delta_1 \tan \alpha + \eta \delta_2 \frac{(1 + \tan^2 \alpha)^{5/4}}{\sqrt{\tan \alpha}}. \quad (2.189)$$

The solution for minimal mass can be achieved assuming that:

$$\delta_1 \tan \alpha \ll \eta \delta_2 \frac{(1 + \tan^2 \alpha)^{5/4}}{\sqrt{\tan \alpha}}. \quad (2.190)$$

So that the (2.189) becomes:

$$\bar{\mu}_B = \eta \delta_2 \frac{(1 + \tan^2 \alpha)^{5/4}}{\sqrt{\tan \alpha}}. \quad (2.191)$$

The optimal angle can be obtained from:

$$\frac{\partial \bar{\mu}_B}{\partial \tan \alpha} = \frac{\eta}{2} \delta_2 (1 + \tan^2 \alpha)^{(1/4)} \left(\frac{4 \tan^2 \alpha - 1}{\tan \alpha \sqrt{\tan \alpha}} \right) = 0, \quad (2.192)$$

yielding the optimal angle of (2.182). Substituting it into (2.189) concludes the proof. □

Fig. 2.20 for yielding and Fig. 2.21 for buckling show as the theorems obtained in this section can be applied to compute the optimal mass of *substructure* or *superstructure* for any choice of the parameter ρ (for yielding) or η (for buckling). We obtained that, with the addition of deck mass to the design, the optimal complexity n becomes greater than 1. In the next section we will show the effect of the addition of joint mass.

2.7.4 Penalizing Complexity with cost considerations: Adding Joint Mass

Theorem 2.7.1, for $m_d = 0$, leads to an optimal complexity $n = 1$ which corresponds to a minimal mass equal to $\sqrt{1 + \varrho}/2$. As complexity n approaches infinity, instead, the mass given in (2.158), for $m_d = 0$, go to a limit equal to $\sqrt{1 + \varrho}$. However, the addition of the deck mass in Theorem 2.7.1 switches the optimal complexity from $n = 1$ to $n = \infty$, so small complexities n are penalized by massive decks. Also in this latter case, the resulting optimal minimal mass is then $\sqrt{1 + \varrho}$, as can be verified looking the (2.158) or considering that as n goes to infinity the deck mass given in (2.150) approaches zero. As a matter of fact, neither $n = 1$ or $n = \infty$ are believable solutions due to practical reasons: the first solution leads only to a single force at the middle of the span, the second solution leads to an infinite number of joints and connections. The minimal masses obtained from (2.158) with or without deck correspond to perfect massless joints. The addition of the joint masses to a tensegrity structure with n_n nodes, as illustrated in [27], leads to the following total normalized mass:

$$\mu_{Y,tot}^* = \mu_Y^* + \mu_d^* + \Omega n_n, \quad (2.193)$$

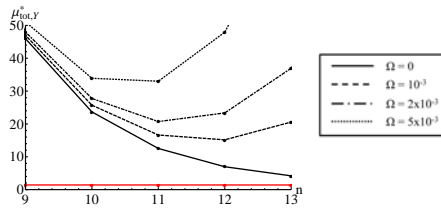


Figure 2.22: Optimal masses under yielding of the substructures (left) and superstructure (right) (red curve) and total optimal mass with deck and different joint factors (dashed and dotted curves) for different values of the complexity n (steel for bars, cables, deck, $F = 1 N$, $L = w_d = 1 m$).

2. ANALYTIC RESULTS ON THE OPTIMAL DESIGN OF TENSEGRITY BRIDGES

Let $\$j$ be the cost per kg of making joints and let $\$b$ be the cost per kg of making bars. Then define $\Omega = \$b/\j . For perfect joints $\Omega = 0$, for rudely made low cost joints $\$j$ is small and Ω is larger. Hence Ω is also approximatively the ratio of material cost per joint divided by material cost per structural member being joined.

Consider the minimal masses of the *substructure* bridge (μ_Y^*) constrained against yielding, for the cases with or without deck, see Eq. (2.158). Assume steel material for cables, bars and deck beams and set $F = 1 N$, $L = w_d = 1 m$. Without deck the optimal aspect angle β_Y^* (2.98) is $35.26 deg$. For the case with neither deck nor joint mass, the optimum complexity n is 1, which corresponds to an optimal mass $\mu_Y^* = \sqrt{2}/2$. As n approaches infinity the mass tends to a limit equal to $\sqrt{2}$, which is also the optimal mass for the case with deck mass and perfectly manufactured joints, since μ_d^* approaches zero for $n \rightarrow \infty$. Note that with the addition of joint masses as illustrated in (2.193), the optimal complexity n^* can become a finite value. The above procedure can be also used for the design under buckling constraints.

Figs. 2.22 (for yielding) and Fig. 2.23 (for buckling) show the total minimal masses obtained by using (2.193). In both Figs. 2.22 and 2.23 we also show with red curves the minimal mass of *substructures* or *superstructures* only. In either case, the total mass of the structure with deck (but no joint mass), is shown by black continuous lines in Figs. 2.22 and 2.23, reaching minimum for

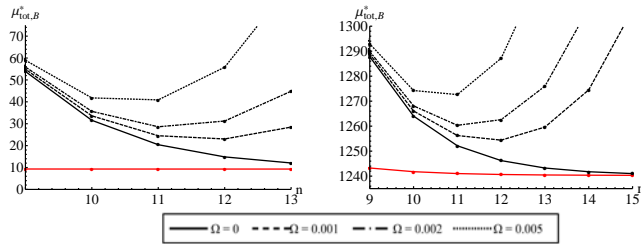


Figure 2.23: Optimal masses under buckling of the substructures (left) and superstructure (right) (red curves) and total optimal masses with deck and different joint factors (dashed and dotted curves) for different values of the complexity n (steel for bars, cables, deck, $F = 1 N$, $L = w_d = 1 m$).

an infinite complexity n . It is worth nothing that, for infinite n , the mass of the deck is zero and the total minimum mass is just the mass of the bridge structure. Then, with the dotted and dashed lines, we show that a finite optimal complexity can be achieved if the joint's masses are considered.

From Fig. 2.22 note that the minimal mass ($\mu \cong 21$) bridge has complexity $n = 11$ for $\Omega = 0.002$, and has minimal mass $\mu \cong 15$ with complexity $n = 12$ for $\Omega = 0.001$. Economic costs would decide if saving 25 % structural mass is worth the extra cost of improving the joint precision by a factor of 2.

2.8 Discussion of the results

We designed bridges from the elementary consideration of i) yielding constraints, ii) buckling constraints, iii) without deck mass, iv) with deck mass, v) *superstructure* only, vi) *substructure* only, vii) without joint mass, viii) with joint mass.

We optimize the complexity of the structure, where structural complexity as the number of members in the design. This can be related to 3 parameters (n, p, q) , where 2^n is the number of deck sections along the span; p is the number of compressive members (bars) reaching from the span center to the *substructure*; and q is the number of cables reaching from the span center to the *superstructure*. Hence we refer to (n, p, q) as the three different kinds of *complexities* of the structure. We used a tensegrity structural paradigm which allowed these several kinds of complexities. The complexity n is determined by a self-similar law to fill the space of the bridge. As the number of self-similar iterations go to infinity we get a tensegrity fractal topology. However, the number of self-similar iterations n and the complexities p and q required to minimize mass, under different circumstances within the set of 8 possibilities i),...,viii) listed above, go to an optimal number between 1 and infinity, where an infinite complexity fills the define space with a continuum.

First we optimized structures under yielding constraints for the simply-supported case ($n = 1$) with no deck. The number of self-similar iterations

2. ANALYTIC RESULTS ON THE OPTIMAL DESIGN OF TENSEGRITY BRIDGES

n of the given tensegrity module goes to infinity as the mass approaches the minimum. Our result produces the same topology as [20], where there is a compressive member at 45 deg attached at each boundary, connecting to a $1/4$ pie shaped continuum material piece at the center. The bottom half of the bridge (the *substructure*) is the *dual* of the *superstructure* (*dual* meaning flip the structure about the horizontal axis and replace all tension members with compression members and all tension members with compressive members). We showed that the top half of this structure is the optimal topology for bridge designs which do not allow any *substructure*, and conversely that the bottom half of this structure is the optimal topology for bridges allowing no *superstructure*.

Secondly, we optimized the simply supported bridge ($n = 1$) under buckling constraints with no deck. For the *superstructure* design we proved that the minimal mass is achieved at high values of q , approaching a continuum (where the shape of the structure is a half disk). It is interesting that this shape (designed under buckling constraints) is the same as the result of [20], which was derived under *yielding* constraints and different boundary conditions (our conditions were hinge/hinge and his were hinge/roller). We also optimized the *substructure* bridge (without deck) to find an optimal complexity $(n, p, q) = (1, 1, 0)$. This *substructure* bridge has less mass than the *superstructure* bridge except for extremely high complexity ($q > 400$). At $q = 3000$, the *superstructure* has one fifth the mass of the *substructure* design. Thirdly, we consider adding a deck to the bridge, since this is the only practical possibility to carry distributed loads. Under *yield* constraints the minimal mass bridge requires infinite complexity n (infinite self-similar iterations of the tensegrity module). The bridge has *superstructure* and *substructure* that are duals of each other. The angle of departure from the boundaries is 35.26 deg (as opposed to 45 deg for the no deck mass discussed above). Under buckling constraints the structure $(n, p, q) = (n, 1, 1)$ has minimal mass at $n = \infty$. The *superstructure* has a departure angle (from the boundary) of approximately 26.56 deg as opposed to larger angles for yielding designs and no-deck designs.

2. ANALYTIC RESULTS ON THE OPTIMAL DESIGN OF TENSEGRITY BRIDGES

The *substructure* under buckling constraints has an even more streamlined profile with departure angle approximatively of 5.18 *deg*. Furthermore the mass of a *substructure* design is much smaller than the mass of a *superstructure* design.

In all of the design cases studied, we conclude that the infinite complexity *substructure* bridge is the solution which minimizes the sum of deck mass and structural mass.

Finally, we consider the impact of assigning a mass penalty to the number of required joints. We suppose that the cost per *kg* of compressive members is $\$_b$, and that the cost per *kg* of fabricated joints is $\$_j$. The ratio $\Omega = \$_b/\$_j$ is used as a weighting factor to add joint mass to member mass and this sum is minimized. The total minimal mass is always at a finite complexity $n < \infty$ and $p = q = 1$. Again, buckling is always the mode of failure in our study, leading to the conclusion that with deck mass and joint mass, this paper describes the optimal complexity to obtain a minimal mass bridge, and this bridge is not a continuum (as Michell produced under yield assumptions), but, has finite complexity n . The optimal complexity n is given in terms of fabrication costs and material properties.

3

**Numerical Results on the
Optimal Design of Tensegrity
Bridges**

3.1 Introduction

The present Chapter deals with a numerical approach to the parametric design of tensegrity bridges, which complements the analytic one presented in Chap. 2. The minimal mass topology derived from A.G.M. Michell derived in [20] for a simply supported bridge structures examines only superstructures above the roadbed. Nevertheless, a tensegrity deck design requires a structure also below the roadbed. The bridge model analyzed here and in Chap. 2 integrates superstructures and substructures to minimize the overall mass of the bridge.

We hereafter examine different versions of the general bridge model presented in Chap. 2, with or without considering the mass of the deck. A key result that we observe is that the minimum mass topology of the tensegrity bridge features two different (discrete-continuous) structural scales, which are related to the different complexity parameters taken into account. We end by presenting the main conclusions of the present study in Sect. 4.6.

3.2 First bridge model without deck

In a famous work dated 1904, A.G.M. Michell examines the problem of finding the minimum volume network of fully stressed truss elements, which transmit a vertical force applied at the middle point C of a given segment AB to two fixed hinge supports applied at A and B [20]. On pages 594-597 of this work, Michell deals with a truss network spanning a 2D continuous domain including the points A , B and C along its boundary (*centrally loaded beam*), and assumes that the material of such a domain is homogenous. Without entering the mathematical aspects of Michell's problem (refer, e.g., to [14]), we notice that the Michell topology under consideration includes a portion DE of a circumference centered in C , the segments DA and EB lying on the tangents in D and F to the arch DE , and all the radii of the circular sector CDE (cf. Fig. 3.1, where the compressive elements (or *bars*) of the Michell frame are represented through thick black lines, while the tensile elements (or *strings*) are

3. NUMERICAL RESULTS ON THE OPTIMAL DESIGN OF TENSEGRITY BRIDGES

represented through thin red lines). Such a topology can be applied to both the regions placed above and below the applied force F , with the difference that the arch ADEB (hereafter also called Michell arch) works in compression and the radii pointing to C work in tension in the first case (Fig. 3.1, top), while, on the contrary, the arch ADEB works in tension and the radii pointing to C work in compression in the second case (Fig. 3.1, bottom). It is worth noting that the central angle of the circular sector CDE gets larger and larger, as the angle α (or β) gets closer and closer to 90 deg (Fig. 3.1).

We here introduce a parametric model of a tensegrity bridge obtained through n self-similar subdivisions of a basic module. This module is formed by a single Michell arch showing p radii, placed above the deck of the bridge, and two arches, each of them showing $q = p$ radii, placed below the deck. Such a bridge is constrained by a fixed hinge support at one end of the deck, and a rolling hinge support at the other end. We show the basic module corresponding to $n = p = 1$ in Fig. 3.2, while more complex shapes corresponding to higher values of n and p are shown in Fig. 5.4.3. Notice how each arch above the deck features p radii, and each arch below the deck features q radii, with $p = q$. The angles α and β can assume arbitrary values, and the horizontal elements at the level of the deck (represented through blue lines in Fig. 3.2) can work either in tension or in compression (*bidirectional elements*, cf. [145]). Such elements provide the horizontal components of the lateral (supporting) forces of the Michell arch (Fig. 3.1). The basic module shown in Fig. 3.2 exhibits a single compressed arch above the deck, two tensile chords below the deck and a subdivision of the deck into four elements of equal length. Hereafter, we let f denote the total force transferred from the deck to the bridge structure. For $n > 1$, we assume that the elements of the nested arches placed above the deck can overlap each other. Moreover, to consider a common requirement for bridges over navigable water, we discard the outer arches placed below the deck (indicated by dotted lines in Fig. 5.4.3), in order to reduce the size of the substructure below the deck, for clearance above the water. In a real bridge structure, the elements placed above the deck would have a

3. NUMERICAL RESULTS ON THE OPTIMAL DESIGN OF TENSEGRITY BRIDGES

3D geometry that prevents member overlapping. It is worth noting that the geometry corresponding to an arbitrary number n of self-similar subdivisions of the basic module features 2^{n+1} elements at the level of the deck, and show nodal forces equal to $f/(2^{n+1})$ in correspondence with the intermediate nodes placed at the level of the deck. The following variables completely define the geometry of the bridge structure: the total span L , the ‘top aspect angle’ α , the ‘bottom aspect angle’ β , and the complexity parameters n, p and q . The total numbers of top arches, n_{ta} , bottom arches, n_{ba} , strings, n_s , bars, n_b , and nodes, n_n , are given by:

$$n_{ta} = 2^n - 1, \quad n_{ba} = 2^n, \quad (3.1)$$

$$n_s = qn_{ta} + (p + 1)n_{ba} + 2^{n+1}, \quad n_b = (q + 1)n_{ta} + pn_{ba} + 2^{n+1}, \quad (3.2)$$

$$n_n = q n_{ta} + p n_{ba} + 2^{n+1} + 1. \quad (3.3)$$

As to the node coordinates, we observe that the nodes belonging to the ‘superstructure’ (i.e., the portion of the bridge placed above the deck) lie on n nested circumferences with radii R_{t_i} ($i = 1, \dots, n$), while the nodes of the ‘substructure’ instead lie on sequential circumferences with radius R_b . Such radii are computed as follows

$$R_{t_i} = \frac{L}{2^i} \sin \alpha, \quad (i = 1, \dots, n); \quad R_b = \frac{L}{2^n} \sin \beta. \quad (3.4)$$

We look for the optimal values of the complexity parameters n, p and q and the aspect angles α and β , which minimize the mass of the bridge under yielding and buckling constraints. As anticipated, we prescribe $q = p$ and we assume that all bars and strings are made up of the same material, for the sake of simplicity. The removal of such constraints is not a big issue from the theoretical point of view, but might lead to a significant increase in the number

3. NUMERICAL RESULTS ON THE OPTIMAL DESIGN OF TENSEGRITY BRIDGES

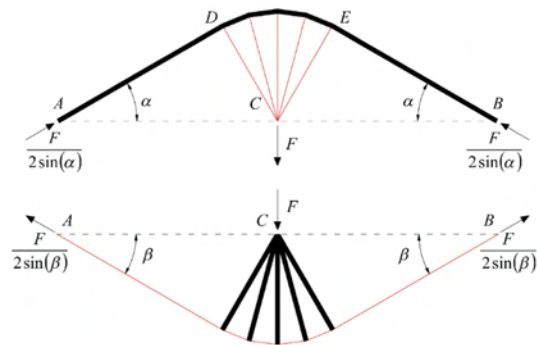


Figure 3.1: Michell frames for a centrally loaded beam.

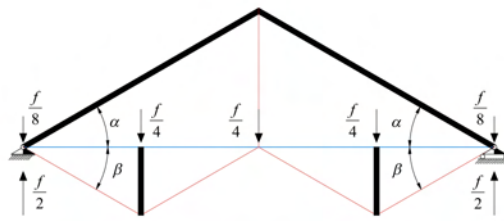


Figure 3.2: Basic module of the tensegrity bridge ($n = 1, p = 1$).

of optimization variables. We close the present section with some remarks on prestress design, a typical feature of tensegrity systems. The procedure by [145] returns the minimal mass structure, for a given loading condition, together with a certain prestress state. By changing such a prestress, while increasing the mass, one can improve the ability of a structure to tolerate larger uncertainties in the external loading, and avoid slackening problems in cables. We leave the prestress calibration to a second step of the current design strategy, to be carried out after the minimal mass topology has been determined.

3.2.1 Mass minimization algorithm

We deal with the minimum mass design of the fractal bridge presented in Sect. 3.2 through the iterative linear programming procedure extensively presented

3. NUMERICAL RESULTS ON THE OPTIMAL DESIGN OF TENSEGRITY BRIDGES

in [145] that we briefly summarize hereafter. Let $\bar{\sigma}_Y$ denote the yield stress of the material. We enforce the following yield constraint in the generic string

$$\sigma_{s_i} = \bar{\sigma}_Y, \quad i = 1, \dots, n_s, \quad (3.5)$$

where σ_{s_i} denotes the maximum admissible stress in such an element. Concerning the bars, we assume that the maximum admissible compressive stress σ_{b_i} in each of such elements, defined as a positive quantity, is given by

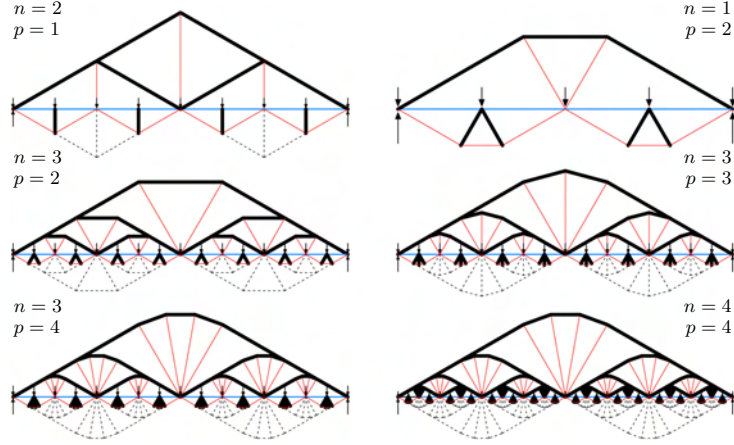


Figure 3.3: Exemplary geometries of the tensegrity bridge for different values of the complexity parameters n and $p = q$.

$$\sigma_{b_i} = \min (\bar{\sigma}_Y, \bar{\sigma}_{B_i}), \quad i = 1, \dots, n_b, \quad (3.6)$$

where $\bar{\sigma}_{B_i}$ denotes the local buckling stress [145]. Denoting the i -th bar length by b_i , and assuming that such a bar has circular cross-section with radius r_{b_i} ,

3. NUMERICAL RESULTS ON THE OPTIMAL DESIGN OF TENSEGRITY BRIDGES

we compute $\bar{\sigma}_{B_i}$ through Euler's formula

$$\bar{\sigma}_{B_i} = \frac{\pi^2 E}{4} \left(\frac{r_{b_i}}{b_i} \right)^2 = \frac{\pi E}{4} \frac{A_{b_i}}{b_i^2}, \quad i = 1, \dots, n_b, \quad (3.7)$$

where E is the Young moduli of the material, and $A_{b_i} = \pi r_{b_i}^2$ is the area of the cross-section.

Now, let λ_{b_i} denote the compressive force per unit length in the i -th bar, and let γ_{s_i} denote the tensile force per unit length in the i -th string, both defined to be positive quantities. Assuming that all the bars and strings are *fully stressed* (i.e., the normal stress is equal to the maximum admissible stress in each of such elements), we compute the overall mass of the bridge structure through

$$m = \mathbf{c}^T \mathbf{x}, \quad (3.8)$$

with

$$\mathbf{x} = [\lambda_1 \cdots \lambda_{n_b} \mid \gamma_1 \cdots \gamma_{n_s}]^T, \quad (3.9)$$

$$\mathbf{c} = \left[c_{b_1} \quad \dots \quad c_{n_b} \mid c_{s_1} \quad \dots \quad c_{n_s} \right]^T, \quad (3.10)$$

and we set

$$c_{b_i} = \frac{\varrho b_i^2}{\sigma_{b_i}}, \quad c_{s_i} = \frac{\varrho s_i^2}{\sigma_{s_i}}, \quad (3.11)$$

ϱ being the mass density per unit volume of the material, and s_i being the length of the i -th string. The force density vector \mathbf{x} must satisfy the equilibrium equations of all the nodes of the bridge structure, which we write into the following matrix form

$$\mathbf{A} \mathbf{x} = \mathbf{w}. \quad (3.12)$$

3. NUMERICAL RESULTS ON THE OPTIMAL DESIGN OF TENSEGRITY BRIDGES

Here, \mathbf{A} is a *static matrix* depending on the geometry and the connectivity of bars and strings, and \mathbf{w} is the *nodal force vector* obtained by stacking-up the single external force vectors of each node (refer to [145] for the detailed expressions of such arrays). We neglect the contributions to \mathbf{w} due to the self-weight of the bridge structure, assuming that the overall weight of the bridge structure is much less than the weight of the deck. If needed, the inclusion of gravity forces into Eq. (3.12) can be easily carried out following [145] (cf. Sect. 3.3).

Given the bridge span, L , the total weight of the deck, f , and arbitrary values of the design variables, α , β , n and p , we determine the minimum bridge mass and the optimal values of the force densities by iteratively solving the linear programming problem

$$\begin{aligned} & \underset{\mathbf{x}}{\text{minimize}} && m = \mathbf{c}^T \mathbf{x}, \\ & \text{subject to} && \begin{cases} \mathbf{A}\mathbf{x} = \mathbf{w}, \\ \mathbf{x} \geq 0. \end{cases} \end{aligned} \quad (3.13)$$

Initially, we set $\sigma_{b_i} = \bar{\sigma}_Y$ in all the bars. Let us denote the current solution of problem (3.13) by \mathbf{x}' , and the corresponding minimum mass of the bridge by m' (step 1). The current values of the axial forces in all the bars and strings are given by

$$t'_{b_i} = \lambda'_{b_i} b_i, \quad t'_{s_i} = \gamma'_{s_i} s_i, \quad (3.14)$$

where λ'_{b_i} is the entry of \mathbf{x}' corresponding to the i -th bar, and γ'_{s_i} is the entry of the same vector corresponding to the i -th string. By post-processing the current solution, and enforcing combined yielding and buckling constraints in all the bars, we compute updated bar cross-section areas through

3. NUMERICAL RESULTS ON THE OPTIMAL DESIGN OF TENSEGRITY BRIDGES

$$A''_{b_i} = \begin{cases} \sqrt{t'_{b_i}/(\pi E/4b_i^2)} & (t'_{b_i} \leq t_{b_i}^*) \\ t'_{b_i}/\bar{\sigma}_Y & (t'_{b_i} > t_{b_i}^*) \end{cases}, \quad (3.15)$$

where $t_{b_i}^* = (\bar{\sigma}_Y)^2/(\pi E/4b_i^2)$ (cf. [145], Appendix A). Accordingly, we define an updated mass of the bridge structure, via the equation

$$m'' = \sum_{i=1}^{n_b} \varrho A''_{b_i} b_i + \sum_{i=1}^{n_s} \frac{\varrho s_i^2}{\sigma_{s_i}} x'_{s_i}. \quad (3.16)$$

If the ratio $|(m'' - m')/m'|$ is lower than a given tolerance we stop the optimization procedure at the current iteration, otherwise we set $\sigma_{b_i} = t'_{b_i}/A''_{b_i}$ and go back to step 1. The rest of the document makes use of the following dimensionless mass factor,

$$\mu = \frac{m \bar{\sigma}_Y}{\varrho L f}. \quad (3.17)$$

A pure yielding design of the bridge, which corresponds to the approach followed by Michell in his 1904 study of a centrally loaded beam, is obtained by arresting the above procedure at the first iteration ($\sigma_{b_i} = \bar{\sigma}_Y$ in all the bars). Hereafter, we use the index Y to denote the mass and the design variables corresponding to such a design strategy. It is worth noting that the solution of the optimization problem (3.13) leads us to resolve the indeterminacy associated with the bidirectional elements placed at the level of the deck [145].

3.2.2 Numerical results

In this section we present a collection of numerical results, which aim to illustrate the potential of the minimum mass design under consideration. We use the symbols μ^* , α^* and β^* to denote the minimum mass and the optimal aspect angles of the tensegrity bridge under combined yielding and buckling constraints, respectively, and the symbols μ_Y^* , α_Y^* and β_Y^* to denote the optimal values of the same quantities under simple yielding constraints. In all the examples, we search for a global minimum mass configuration of the bridge, by recursively running the optimization procedure presented in Sect. 3.2.1, so that the design variables n , p , α and β may range within prescribed search domains. We set the step increments of n and p to 1, the step increments of α and β to 0.01 deg. In addition, we set L , f and ϱ to unity, in abstract units, and make use of the following assumptions: $\bar{\sigma}_Y = 6.9 \times 10^8 L^2/f$; $E = 2.1 \times 10^{11} L^2/f$. It is worth observing that the basic module shown in Fig. 3.2 can be in equilibrium either in presence of the elements placed at the level of the deck, or in absence of such elements (blue elements in Fig. 3.2), due to the double arch mechanism played by the two portions of the bridge placed above and below the deck. In order to highlight the relative ‘weight’ of the elements placed at the level of the deck, we introduce the following ratios,

$$\frac{\mu_{db}^*}{\mu_b^*}, \quad \frac{\mu_{ds}^*}{\mu_s^*}. \quad (3.18)$$

where μ_{db}^* , μ_{sb}^* , μ_b^* , μ_s^* denote the total mass of the bars placed at the level of the deck, the total mass of the strings placed at the level of the deck, the overall mass of the bars and the overall mass of the strings, respectively, in correspondence with any arbitrary minimum mass configuration under combined yielding and buckling constraints. We remind the reader that the elements placed at the level of the deck are bidirectional, in the sense that they can contemporarily serve as bars or strings [145].

3.2.3 Minimum mass design for $n = 1$, and variable p , α , and β

We begin by conducting a minimum mass design that keeps n constant and equal to 1, and lets α , β and p range in the following intervals,

$$p \in [1, 60], \quad \alpha \in (0, 90) \text{ deg}, \quad \beta \in (0, 90) \text{ deg}. \quad (3.19)$$

Figure 3.4 and Tab. 3.1 show the optimization results obtained in the present case. Under simple yielding constraints, the results shown in Tab. 3.1 indicate that the mass of the bridge might converge to a global minimum when $p \rightarrow \infty$ ($\mu_Y^* \rightarrow 0.985$, cf. Tab. 3.1). Conversely, the aspect angles α and β converge to the following limiting values: $\alpha_Y^* \rightarrow 54.73$ deg, and $\beta_Y^* \rightarrow 35.26$ deg. The inclusion of self-weight [145] does not cause a significant change of the optimal topology: by adding gravity forces we indeed obtain $\mu_Y^* = 0.9853$, $\alpha_Y^* = 55.31$ deg, $\beta_Y^* = 35.84$, when $p = 60$. Under *combined* buckling and yielding constraints, the mass of the bridge approaches a global minimum for a finite value of the complexity p ($\mu^* \rightarrow 337.69$ for $p = 11$, cf. Tab.3.1). As p approaches such an optimal value, the aspect angles converge to the following limiting values: $\alpha^* \rightarrow 53.42$ deg, and $\beta^* \rightarrow 33.97$ deg. It is worth noting that the minimum mass configuration under combined buckling and yielding constraints shows similar aspect ratios and a much greater mass, as compared to that corresponding to simple yielding constraints. For $p < 25$, the mass ratio μ_{ds}^*/μ_s^* assumes values ranging in the interval $[1 \times 10^{-7}, 6 \times 10^{-5}]$, while the mass ratio μ_{db}^*/μ_b^* ranges in the interval $[2 \times 10^{-11}, 6 \times 10^{-7}]$. Such results show that the elements placed at the level of the deck can be ignored for $p < 25$. On the contrary, for $p \geq 25$ we again observe $\mu_{ds}^*/\mu_s^* \ll 1$, but this time the ratio μ_{db}^*/μ_b^* becomes relevant and progressively increasing with p , being equal to 0.56 for $p = 25$, and 0.68 for $p = 60$. The latter results highlight that the elements placed at the level of the deck act as compressed members (bars) of relevant structural importance for $p \geq 25$. Fig. 3.4 illustrates the geometries of the (relative) minimum mass configurations corresponding to

3. NUMERICAL RESULTS ON THE OPTIMAL DESIGN OF TENSEGRITY BRIDGES

p	α_Y^*	β_Y^*	μ_Y^*	α^*	β^*	μ^*
1	41.83	24.11	1.1180	26.11	13.77	808.84
3	50.29	31.05	1.0235	42.78	24.83	446.26
5	53.42	33.97	0.9952	50.29	31.05	375.84
7	54.33	34.86	0.9896	51.97	32.59	349.79
9	54.42	34.95	0.9876	53.13	33.69	340.13
10	54.42	34.96	0.9871	53.42	33.97	338.30
11	54.44	34.97	0.9867	53.42	33.97	337.69
12	54.49	35.02	0.9864	53.42	33.97	337.92
13	54.53	35.06	0.9862	53.42	33.97	338.76
15	54.58	35.11	0.9859	53.13	33.69	341.67
20	54.65	35.18	0.9855	51.98	32.60	352.24
25	54.68	35.21	0.9854	74.39	22.29	375.03
30	54.70	35.23	0.9853	76.17	21.15	372.02
40	54.72	35.25	0.9852	78.37	19.60	369.85
50	54.72	35.25	0.9852	79.69	18.54	370.17
60	54.73	35.26	0.9851	80.57	17.75	371.58

Table 3.1: Selected results for the example in Sect. 3.2.3.

several selected values of p , in presence of combined yielding and buckling constraints.

3.2.3.1 Minimum mass design for variable n , p , α , and β

The second minimum mass design that we examine assumes that all the design variables n , p , α , and β may simultaneously vary within the following bounds,

$$n \in [2, 5], \quad p \in [1, 7], \quad \alpha \in (0, 90) \text{ deg}, \quad \beta \in (0, 90) \text{ deg}. \quad (3.20)$$

The most relevant results corresponding to the present case are illustrated in Tab. 3.2 and Figs. 3.5, 3.6. The results in Tab. 3.2 highlight that the global minimum mass configuration under combined yielding and buckling constraints is reached for $n = 2$, $p = 7$ ($\mu^* = 333.17$, $\alpha^* = 62.52$ deg, $\beta^* = 17.77$ deg), within the search domain (3.23). In particular, the mass of such

3. NUMERICAL RESULTS ON THE OPTIMAL DESIGN OF TENSEGRITY BRIDGES

n	p	α_Y^*	β_Y^*	μ_Y^*	α^*	β^*	μ^*
2	1	44.62	9.34	1.5207	26.58	4.77	1086.23
2	3	57.81	14.83	1.3329	45.20	9.53	558.02
2	5	63.73	18.66	1.2674	56.10	13.93	413.11
2	7	66.42	20.90	1.2534	62.52	17.77	333.17
3	1	44.96	4.08	1.7545	26.58	2.05	1186.33
3	3	59.52	6.92	1.5232	45.31	4.13	607.67
3	5	69.56	10.85	1.4341	56.63	6.19	446.20
3	7	72.52	12.78	1.4137	63.71	8.23	354.03
4	1	44.96	1.91	1.8761	26.58	1.03	1221.82
4	3	59.73	3.27	1.6256	45.31	1.93	625.75
4	5	71.41	5.66	1.5262	56.65	2.90	459.24
4	7	75.51	7.35	1.5021	63.82	3.88	363.95
5	1	45.01	0.93	1.9378	26.58	0.75	1234.39
5	3	59.92	1.60	1.6784	45.32	1.44	632.19
5	5	71.84	2.83	1.5747	56.65	1.71	463.95
5	7	76.80	3.96	1.5489	63.83	1.88	367.65

Table 3.2: Selected results for the example in Sect. 3.2.3.1.

a configuration is slightly lower than the global minimum mass obtained for $n = 1$, $p = 11$ in Sect. 3.2.3 ($\mu^* = 333.17$ vs $\mu^* = 337.69$, respectively). Referring to the case with $n = 2$, in order to detect if the global minimum mass configuration is obtained for finite complexity p or not, we let this parameter grow up to $p = 13$, and determine the corresponding relative minimum mass configurations of the bridge. We find out that the mass of the bridge monotonically decreases when p grows from 1 to 13, and n remains equal to 2. In particular, the relative minimum mass configuration for $n = 2$ and $p = 13$ is the following: $\mu^* = 225.98$, $\alpha^* = 69.45$ deg, $\beta^* = 23.97$ deg. Such results, together with those presented in Tab. 3.2, indicate that the global minimum mass configuration of the bridge might be achieved either for rather large values of p , or in the limit $p \rightarrow \infty$, when $n \geq 2$. By adding gravity

3. NUMERICAL RESULTS ON THE OPTIMAL DESIGN OF TENSEGRITY BRIDGES

p	μ_Y^*	μ^*
1	2.0261	1419.43
5	1.8545	569.55
10	1.8486	524.96
15	1.8478	512.81
20	1.8475	507.41
30	1.8473	502.79
40	1.8473	501.03
50	1.8472	500.33
60	1.8472	500.12

Table 3.3: Selected results for the example in Sect. 3.2.3.2.

forces [145], and referring to the case with $n = 2$ and $p = 13$, we obtain $\mu^* = 227.49$, $\alpha^* = 69.48$ deg, and $\beta^* = 23.52$ deg. Such results show that the inclusion of self-weight does not cause a significant change of the minimum mass configuration at hand, as we already observed in presence of simple yielding constraints (cf. Sect. 3.2.3). As to the elements placed at the level of the deck, we observe the following results: $\mu_{db}^*/\mu_b^* \ll 1$, and $\mu_{ds}^*/\mu_s^* \ll 1$, for $n \leq 3$. The ratio μ_{ds}^*/μ_s^* becomes relevant for $n > 3$, being equal to 0.06 for $n = 4$ and $p = 1$, and 0.3 for $n = 5$ and $p = 1$. Nevertheless, the same ratio decreases with p for fixed n , being equal to $\approx 10^{-4}$ for $n = 4$ and $p = 7$, and $\approx 10^{-5}$ for $n = 5$ and $p = 7$. We can therefore conclude that such elements serve as tensile members (strings) for $n > 1$, and that their structural relevance increases with n and decreases with p . Regarding the global minimum mass configuration corresponding to the search domain (3.23) and simple yielding constraints, we observe that such a configuration is reached for $n = 2$ and $p = 7$ ($\mu_Y^* = 1.2534$, $\alpha_Y^* = 66.42$ deg, $\beta_Y^* = 20.90$ deg, cf. Tab. 3.2) and that the corresponding mass is greater than the global minimum obtained in Sect. 3.2.3 for $n = 1$ and $p \rightarrow \infty$ ($\mu_Y^* \rightarrow 0.9851$). It is also seen from Tab. 3.2 that, in each of the examined cases, the optimal values of α very slowly increase with n , and rather markedly increase with p . The optimal values of β instead

3. NUMERICAL RESULTS ON THE OPTIMAL DESIGN OF TENSEGRITY BRIDGES

markedly decrease with n , and significantly increase with p . It is worth noting that the two examined design strategies (simple yielding constraints and combined yielding and buckling constraints) lead to rather different aspect ratios of the bridge for $p = 1$ (cf. Fig. 3.5), and, on the contrary, to more similar geometries as p gets larger, for any given n (cf. Tab. 3.2, and Sect. 3.2.3). The results shown in Fig. 3.6 emphasize that the current minimum mass design of the bridge leads to rather large values of α and considerably small values of β , as the complexity parameters n and p progressively increase. In particular, the bottom height of the bridge dramatically shrinks for $n \geq 3$ (Fig. 3.6). This is explained by observing that the lower chords of the bridge carry tensile forces $t_{ba} = \frac{f_n}{2\sin(\beta)}$ (cf. Fig. 3.1), with $f_n = f/(2^{n+1})$. As n goes to infinity and β goes to zero, it can be verified that t_{ba} approaches a finite limit. The solution with $\beta \rightarrow 0$ becomes convenient in terms of mass savings as $n \rightarrow \infty$, since it reduces the lengths of the tensile chords and compressed rays placed below the deck. We wish to remark, however, that the global minimum mass configuration is achieved for $n = 1$ under simple yielding constraints, and $n = 2$ under combined yielding and buckling constraints

3.2.3.2 Minimum mass design for $n = 5$, $\alpha = 40$ deg, $\beta = 60$ deg, and variable p

The results shown in Fig. 3.6 highlight that a rigorous minimum mass design of a tensegrity bridge might lead to rather disordered shapes and member overlapping. Moreover, bridge designers usually prefer to orient their conceptual designs, by requiring that the bridge features given aspect ratios, and/or given topologies or shapes. Therefore, it makes sense to consider a minimum mass design that keeps fixed most of the design variables, and lets just one of them to vary within prescribed bounds. Tab. 3.3 and Fig. 3.7 show the results of a minimum mass design that keeps $n = 5$, $\alpha = 40$ deg, and $\beta = 60$ deg fixed, and lets the complexity p to range in the search interval $[1, 60]$. The results in Tab. 3.3 highlight that the mass of the bridge monotonically decrease with p within such a search domain, either under simple yielding constraints, and in presence of combined yielding and buckling constraints. The current results confirm those presented in the previous section, highlighting that the global minimum mass configuration is achieved either for very large values of p , or in the limit $p \rightarrow \infty$. Concerning the elements placed at the deck level, we now observe $\mu_{db}^*/\mu_b^* \ll 1$, and $\mu_{ds}^*/\mu_s^* \approx 0.6$, which implies that such elements serve as strings with relevant structural importance in the present case. Some of the relative minimum mass geometries corresponding to different choices of p are illustrated in Fig. 3.7.

3. NUMERICAL RESULTS ON THE OPTIMAL DESIGN OF TENSEGRITY BRIDGES

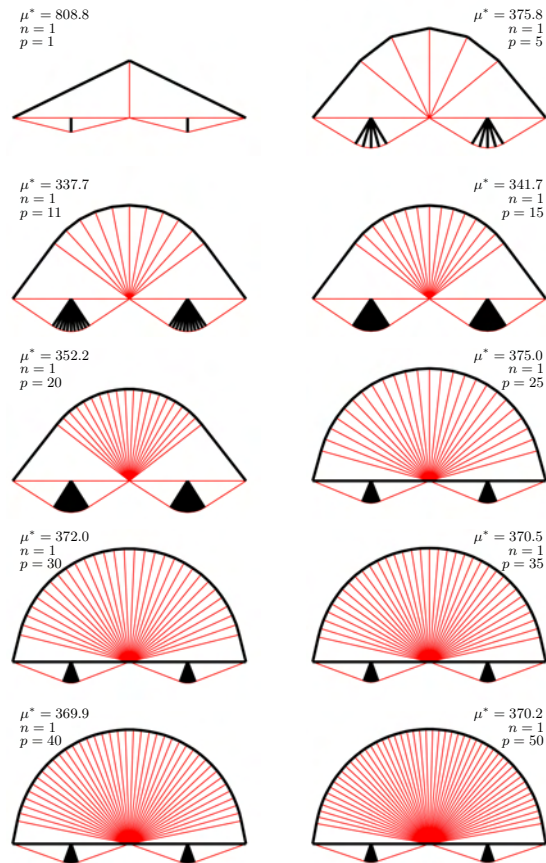


Figure 3.4: Optimal bridge topologies under combined yielding and buckling constraints, for $n = 1$, $\alpha \in (0, 90)$ deg, $\beta \in (0, 90)$ deg, and $p \in [1, 50]$.

3.3 Second bridge model without deck

In the present and next Section 3.4 we show the minimal masses and the optimal angles of tensegrity bridges defined in Chap. 2 with several complexities n , p and q . The numerical results are presented in terms of μ_B^* , α_B^* and β_B^* denoting respectively the minimal masses and the optimal aspect angles under combined yielding and buckling constraints for each bar and yielding constraints for each cable; and in terms of μ_Y^* , α_Y^* and β_Y^* denoting respec-

3. NUMERICAL RESULTS ON THE OPTIMAL DESIGN OF TENSEGRITY BRIDGES

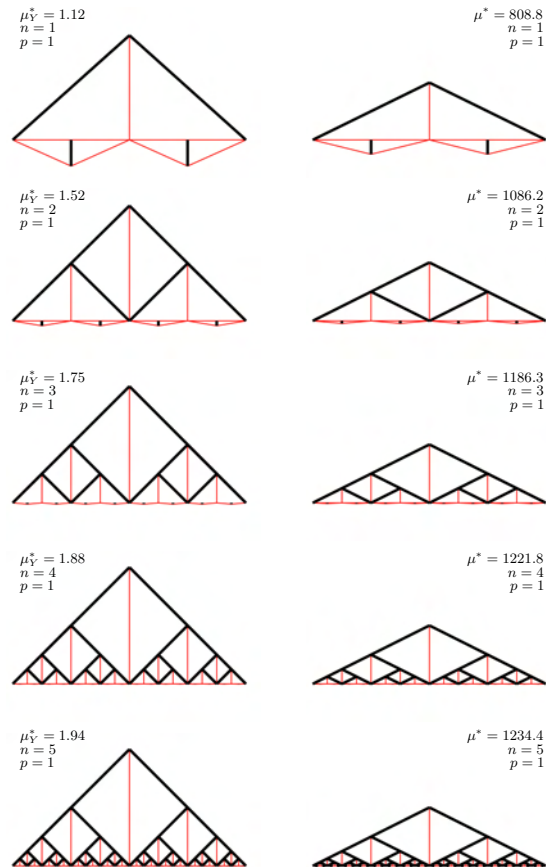


Figure 3.5: Optimal topologies under yielding constraints (left) and combined yielding and buckling constraints (right) for different values of n and $p = 1$.

tively the minimal masses and the optimal aspect angles under yielding constraints only for each member. The results are obtained numerically through a MatLab[®] program written employing the algorithm illustrated in Sect. 3 of [141]. The optimization problems presented in Tables 3.5, 3.6, 3.7, 3.8, 3.9, 3.10, are solved assuming $L = 1$ m, $F = 1$ N, no deck mass, and steel for both cables and bars (refer to Table 4.1 for the material properties; $\varrho = 1$; $\eta = 857.71$). The examined topologies are distinguished in three categories: 1) *nominal* bridges with both structure above and below the roadway (Sect.

3. NUMERICAL RESULTS ON THE OPTIMAL DESIGN OF TENSEGRITY BRIDGES

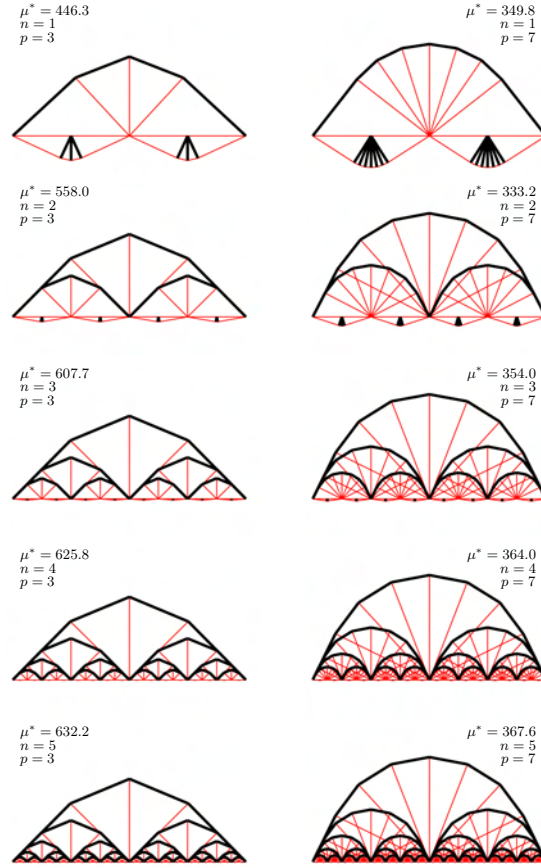


Figure 3.6: Optimal topologies under combined yielding and buckling constraints for different values of n , $p = 3$ (left), and $p = 7$ (right).

3.3.1; Fig 2.3); 2) *substructure* only bridges (Sect. 3.3.2; Fig. 2.5) and 3) *superstructure* only bridges (Sect. 3.4.2; Fig. 4.4). In all the optimized cases, we set step increments of complexities n , p and q to 1 and step increments of 0.01 deg for the aspect angles α and β . It is worth noting that, as showed for the basic module (Fig. 2.2) analyzed in Sect. 2.4.1, the cables placed on the deck have zero mass at the solution for minimal mass basically thanks to the adopted constraints (HH : double fixed hinges). We also show in Section 3.5 some numerical results for rolling hinge at one end of the bridge and fixed

3. NUMERICAL RESULTS ON THE OPTIMAL DESIGN OF TENSEGRITY BRIDGES

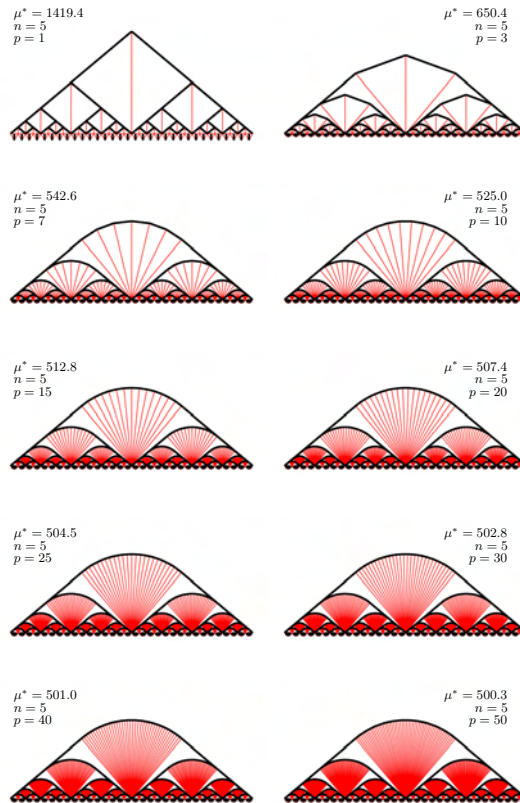


Figure 3.7: Optimal topologies under buckling constraints for $n = 5$, fixed angles $\alpha = 40$ deg and $\beta = 60$ deg, and different values of p .

hinge at the other end (HR). We also report, for each optimized structure, the masses of cables under buckling constraints ($\mu_{B,s}^*$) to show, as will be more clear in the following, as their order of magnitude with respect to the mass total mass of the structure (μ_B^*) increase towards the global optimum. In other words, the principal source of mass savings of a tensegrity structure for buckling is placed in the mass of bars.

3. NUMERICAL RESULTS ON THE OPTIMAL DESIGN OF TENSEGRITY BRIDGES

<i>steel</i>	
ϱ [kg/m^3]	7862
σ [N/m^2]	6.9×10^8
E [N/m^2]	2.06×10^{11}
<i>Spectra[®] - UHMWPE</i>	
ϱ [kg/m^3]	970
σ [N/m^2]	2.7×10^9
E [N/m^2]	120×10^9

Table 3.4: Material properties.

3.3.1 Nominal Bridges

We have performed several numerical results for the *nominal bridges*, illustrated in Fig. 2.3, in which both structure above and below the roadway are allowed. Starting from the basic unit in Fig. 2.2a, we have considered different complexities n , p and q and different aspect angles α and β , in order to get the combination of such parameters that ensures the minimal mass solution. First of all, we start fixing parameter n to unity and let parameters p , α and β ranging in the following intervals:

$$(p, q) \in [1, 100], \quad \alpha \in (0, 90) \text{ deg}, \quad \beta \in (0, 90) \text{ deg}. \quad (3.21)$$

The results of this first design are presented in Table 3.5. For what concern the design under only yielding constraints for all members, the global minimum is achieved for a complexity $q_Y^* = p_Y^* \rightarrow \infty$ and for aspect angles $\alpha_Y^* = \beta_Y^* \rightarrow 45 \text{ deg}$, which corresponds to a minimal mass $\mu_Y^* \rightarrow 0.6427$ (Table 3.5). Such a result confirms the minimal mass solution for a centrally loaded loaded beam reported in Fig. 2 by [20]. In particular, for a beam of total span $2a_M$ loaded in the middle with a force F_M and made of tensile and compressive members with allowable yielding stresses equal respectively to P and Q ; [20] predicted

3. NUMERICAL RESULTS ON THE OPTIMAL DESIGN OF TENSEGRITY BRIDGES

a limit volume equal to:

$$v_M = F_M a_M \left(\frac{1}{2} + \frac{\pi}{4} \right) \left(\frac{1}{P} + \frac{1}{Q} \right). \quad (3.22)$$

Substituting in the (3.22), as in the present case, $F_M = F/2$, $a_M = L/2 m$, $P = Q = 6.9x10^8 N/m^2$, we obtain a volume $v_M = 9.31448x10^{-10} m^3$. On the other hand, the minimal mass $\mu_Y^* \rightarrow 0.6427$ corresponds to a volume $v_Y^* = 0.6427FL/\sigma_s = 9.31449x10^{-10}m^3$. We will show in the next Sects. 3.3.2 and 3.4.2 that the same minimal mass can be achieved also starting from *superstructure only* bridges showed in Fig. 4.4 and *superstructure* bridges showed in Fig. 2.5. The equivalence between *substructure* and *superstructure* under yielding constraints can be justified by the assumption of bars and cables made of the same materials ($\varrho = 1$). An example of this equivalence can be obtained assuming, eg., $\varrho = 1$ in the Eq. (2.99) of Theorem 2.6.1 for *substructures* with complexity $(n, p) = (n, 1)$ and in the Eq. (2.126) of Theorem 2.6.3 for *superstructures* with complexity $(n, q) = (n, 1)$.

Under buckling constraints, the global optimum in the domain (3.21) is achieved for a finite complexity $p_B^* = 1$, which corresponds to a minimal mass of $\mu_B^* = 5.0574$ and an aspect angle of the substructure equal to $\beta_B^* = 4.25 deg$. In all the combined cases under buckling, we have obtained that the optimal solutions keep only the substructure and the total mass of the superstructure is negligible if compared with the total mass. In fact, for the global optimum with $q_B^* = p_B^* = 1$ and $\beta_B^* = 4.25 deg$, we have obtained a mass of the superstructure equal to $4.3983x10^{-10}$. For the other cases, we have obtained similar negligible values of the mass of superstructures ranging from a minimum of $1.9019x10^{-12}$ for the case with $q = p = 45$ and a maximum of $3.1483x10^{-6}$ for the case with $p = q = 10$. The analyzed cases of domain (3.21), then, reduce to the substructure only cases for buckling. As a matter of fact, the angles β_B^* decrease from $4.25 deg$ to $1.98 deg$ as the complexities $q = p$ increase from 1 to 100. The reduction of β_B^* corresponds to an increase of the tensile forces of the cables constituting the substructure and, consequently, also the total

3. NUMERICAL RESULTS ON THE OPTIMAL DESIGN OF TENSEGRITY BRIDGES

n	p	α_Y^* [deg]	β_Y^* [deg]	μ_Y^*	α_B^* [deg]	β_B^* [deg]	μ_B^*	$\mu_{B,s}^*$
1	1	35.26	35.26	0.7071	-	4.25	5.0574	3.3827
1	2	35.26	35.26	0.7071	-	3.80	5.6662	3.7805
1	3	41.41	41.41	0.6614	-	3.57	6.0309	4.0227
1	4	43.23	43.23	0.6514	-	3.40	6.3260	4.2228
1	5	43.96	43.96	0.6476	-	3.27	6.5683	4.3899
1	10	44.78	44.78	0.6437	-	2.91	7.3839	4.9308
1	15	44.91	44.91	0.6431	-	2.72	7.9054	5.2741
1	20	44.95	44.95	0.6429	-	2.59	8.2960	5.5380
1	25	44.97	44.97	0.6428	-	2.50	8.6127	5.7369
1	30	44.98	44.98	0.6428	-	2.42	8.8796	5.9260
1	35	44.98	44.98	0.6428	-	2.36	9.1115	6.0763
1	40	44.99	44.99	0.6428	-	2.31	9.3173	6.2076
1	45	44.99	44.99	0.6427	-	2.26	9.5025	6.3446
1	50	44.99	44.99	0.6427	-	2.22	9.6712	6.4587
1	100	45.00	45.00	0.6427	-	1.98	10.8574	7.2401

Table 3.5: Numerical results of nominal bridge with complexities $n = 1$ and different $p = q$ under yielding ($_Y$) and combined yielding and buckling constraints ($_B$), ($F = 1$ N ; $L = 1$ m ; steel bars and steel strings).

mass of cables (indicated with $\mu_{B,s}^*$ in Table 3.5) increases. In other words, for the combined bridges under buckling or, equivalently, for the substructures bridges under buckling, the total mass of the cables is the big part of the total mass of the structure.

The second optimization domain let the parameters n , p , α and β ranging in the following intervals:

$$n \in [1, 5], \quad p \in [1, 3], \quad \alpha \in (0, 90) \text{ deg}, \quad \beta \in (0, 90) \text{ deg}. \quad (3.23)$$

The results of this second design are presented in Table 3.6. For what concern the yielding case, we can observe that, for fixed values of the complexity p , the global optimum in the domain (3.23) is achieved for $n_Y^* = 1$ and $p_Y^* = 3$. Moreover, the optimal aspect angles α_Y^* and β_Y^* appear not depending on

3. NUMERICAL RESULTS ON THE OPTIMAL DESIGN OF TENSEGRITY BRIDGES

the complexity n . Merging the optimization carried out in both the domains (3.21) and (3.23), we can conclude that the global optimum for yielding is for $n_Y^* = 1$ and $q_Y^* = p_Y^* \rightarrow \infty$ and for aspect angles $\alpha_Y^* = \beta_Y^* \rightarrow 45 \text{ deg}$, which corresponds to a minimal mass $\mu_Y^* \rightarrow 0.6427$ (Table 3.5). It is worth noting that such a solution brings to a mass reduction, from the case with $n = 1$ and $(p, q) = (1, 1)$ ($\mu_Y^* = 0.7071$), of only 9.1%. Moreover the above minimum doesn't take care of manufacture processes that becomes relevant for structures with numerous joints and members. Then, a finite optimal complexity $p = q$ could be achieved a posteriori by adding, eg., joint masses as illustrated in Sect. 2.7.4.

The optimizations under buckling constraints reported in Table 3.6 show that the global optimum in the domain (3.23) is the same obtained in the domain (3.21), i.e. for $p_B^* = 1$, $\beta_B^* = 4.25 \text{ deg}$ and $\mu_B^* = 5.0574$. Also in each complexities ranging in the intervals (3.23) we obtain, for buckling, local minimal masses solutions that keeps only the substructures. In fact, also in domain (3.23), we have obtained negligible values of the mass of superstructures under buckling ranging from a minimum of $3.7436x10^{-13}$ for the case with $n = 5, q = p = 1$ and a maximum of $2.3257x10^{-6}$ for the case with $n = 1, p = q = 3$. Such a results for buckling are also confirmed in the next Sect. 3.3.2. In Table 3.6, we observe that the optimal aspect angles for buckling β_B^* increase as complexity n increase and decrease as complexity $q = p$ increase.

3.3.2 Substructures

In this Section, we show the results obtained for the optimizations of the *substructure* bridges showed in Fig. 4.4 in which only structure below the roadway is allowed. Starting from the basic module illustrated in Fig. 2.2c, we have considered different complexities n , p and different aspect angles α and β ranging in two domains with the aims to get the global minimum mass design both under yielding constraints and under buckling constraints.

First of all, we start fixing parameter n to unity and let parameters p , α

3. NUMERICAL RESULTS ON THE OPTIMAL DESIGN OF TENSEGRITY BRIDGES

n	p	α_Y^* [deg]	β_Y^* [deg]	μ_Y^*	α_B^* [deg]	β_B^* [deg]	μ_B^*	$\mu_{B,s}^*$
1	1	35.26	35.26	0.7071	-	4.25	5.0574	3.3827
1	2	35.26	35.26	0.7071	-	3.80	5.6662	3.7805
1	3	41.41	41.41	0.6614	-	3.57	6.0309	4.0227
2	1	35.26	35.26	1.0607	-	4.40	7.3326	4.9024
2	2	35.26	35.26	1.0607	-	3.93	8.2143	5.4843
2	3	41.41	41.41	0.9922	-	3.69	8.7426	5.8388
3	1	35.26	35.26	1.2374	-	4.49	8.3705	5.6058
3	2	35.26	35.26	1.2374	-	4.02	9.3762	6.2561
3	3	41.41	41.41	1.1575	-	3.77	9.9791	6.6682
4	1	35.26	35.26	1.3258	-	4.55	8.8520	5.9276
4	2	35.26	35.26	1.3258	-	4.07	9.9149	6.6211
4	3	41.41	41.41	1.2402	-	3.82	10.5523	7.0516
5	1	35.26	35.26	1.3700	-	4.59	9.0790	6.0723
5	2	35.26	35.26	1.3701	-	4.10	10.1689	6.7921
5	3	41.41	41.41	1.2816	-	3.85	10.8226	7.2302

Table 3.6: Numerical results of nominal bridges with different complexities n and p under yielding (Y) and combined yielding and buckling constraints (B), ($F = 1\text{ N}$; $L = 1\text{ m}$; steel bars and steel strings).

and β ranging in the following intervals:

$$p \in [1, 500], \quad \alpha \in (0, 90) \text{ deg}, \quad \beta \in (0, 90) \text{ deg}. \quad (3.24)$$

The results of this first design are presented in Table 3.7. For what concern the design under only yielding constraints the global minimum is achieved for a complexity $p_Y^* \rightarrow \infty$ and for an aspect angle $\beta_Y^* \rightarrow 45 \text{ deg}$, which corresponds to a minimal mass $\mu_Y^* \rightarrow 0.6427$ (Table 3.7). The optimizations for buckling constraints, instead, allow to identify a global minimum for complexity $p_B^* = 1$ and for an aspect angle $\beta_B^* = 4.25 \text{ deg}$, which corresponds to a minimal mass $\mu_B^* = 5.0574$ (Table 3.7).

3. NUMERICAL RESULTS ON THE OPTIMAL DESIGN OF TENSEGRITY BRIDGES

n	p	β_Y^* [deg]	μ_Y^*	β_B^* [deg]	μ_B^*	$\mu_{B,s}^*$
1	1	35.26	0.7071	4.25	5.0574	3.3827
1	2	35.26	0.7071	3.80	5.6666	3.7805
1	3	41.41	0.6614	3.57	6.0312	4.0227
1	4	43.23	0.6514	3.40	6.3265	4.2228
1	5	43.96	0.6476	3.27	6.5687	4.3899
1	10	44.78	0.6437	2.91	7.3843	4.9308
1	15	44.91	0.6431	2.72	7.9058	5.2741
1	20	44.95	0.6429	2.59	8.2969	5.5380
1	25	44.97	0.6428	2.50	8.6131	5.7368
1	30	44.98	0.6428	2.42	8.8800	5.9260
1	35	44.98	0.6428	2.36	9.1120	6.0763
1	40	44.99	0.6428	2.31	9.3177	6.2076
1	45	44.99	0.6427	2.26	9.5029	6.3446
1	50	44.99	0.6427	2.22	9.6716	6.4587
1	100	45.00	0.6427	1.98	10.8578	7.2401
1	200	45.00	0.6427	1.76	12.1881	8.1437
1	300	45.00	0.6427	1.65	13.0402	8.6860
1	400	45.00	0.6427	1.57	13.6806	9.1281
1	500	45.00	0.6427	1.51	14.1994	9.4904

Table 3.7: Numerical results of substructures with complexities $n = 1$ and different p under yielding ($_Y$) and combined yielding and buckling constraints ($_B$), ($F = 1 N$; $L = 1 m$; steel bars and steel cables).

Then, we let parameters n , p , α and β ranging in the following intervals:

$$n \in [1, 5], \quad p \in [1, 3], \quad \alpha \in (0, 90) \text{ deg}, \quad \beta \in (0, 90) \text{ deg}. \quad (3.25)$$

The results of this second design are presented in Table 3.8. For what concern the design under only yielding constraints, the global minimum in domain (3.25), is achieved for complexities $n_Y^* = 1, p_Y^* = 3$ and for an aspect angle $\beta_Y^* \rightarrow 41.41 \text{ deg}$, which corresponds to a minimal mass $\mu_Y^* = 0.6614$

3. NUMERICAL RESULTS ON THE OPTIMAL DESIGN OF TENSEGRITY BRIDGES

n	p	β_Y^* [deg]	μ_Y^*	β_B^* [deg]	μ_B^*	$\mu_{B,s}^*$
1	1	35.26	0.7071	4.25	5.0574	3.3827
1	2	35.26	0.7071	3.80	5.6662	3.7805
1	3	41.41	0.6614	3.57	6.0308	4.0227
2	1	35.26	1.0607	4.40	7.3326	4.9024
2	2	35.26	1.0607	3.93	8.2143	5.4843
2	3	41.41	0.9922	3.69	8.7426	5.8388
3	1	35.26	1.2374	4.49	8.3705	5.6058
3	2	35.26	1.2374	4.02	9.3763	6.2562
3	3	41.41	1.1575	3.77	9.9791	6.6682
4	1	35.26	1.3258	4.55	8.8531	5.9929
4	2	35.26	1.3258	4.07	9.9149	6.6212
4	3	41.41	1.2402	3.82	10.5523	7.0517
5	1	35.26	1.3700	4.59	9.0790	6.0723
5	2	35.26	1.3701	4.10	10.1690	6.7921
5	3	41.41	1.2816	3.85	10.8226	7.2302

Table 3.8: Numerical results of substructures with different complexities n and p under yielding (Y) and combined yielding and buckling constraints (B), ($F = 1 N$; $L = 1 m$; steel bars and steel cables).

(Table 3.8). For the optimizations under buckling constraints, instead, we have obtained a global minimum for complexities $n_B^* = p_B^* = 1$ and for an aspect angle $\beta_B^* = 4.25 \text{ deg}$, which corresponds to a minimal mass $\mu_B^* = 5.0574$ (Table 3.8).

Such a results retrace the results in Table 3.5 already obtained for the nominal bridges. This can be explained considering the assumption $\varrho = 1$ and the symmetry of the constraints of the bridge (double fixed hinges, HH). It is shown, eg., in the numerical results of Tables 3.14, 3.15, 3.16 in Section 3.5 that changing constraints from double fixed hinges (HH) to fixed hinge and rolling hinge (HR), the equivalence between *nominal* bridge, *substructure* and *superstructure* bridge never subsists.

3.3.3 Superstructures

We end the numerical results without deck showing the optimizations of the superstructure bridges showed in Fig. 2.5 in which only structure above the roadway is allowed. Starting from the basic module illustrated in Fig. 2.2b, we have considered different complexities n , q and different aspect angles α and β ranging in two domains with the aims to get the global minimum mass design both under only yielding constraints and under buckling constraints.

First of all, we start fixing parameter n to unity and let parameters q , α and β ranging in the following intervals:

$$q \in [1, 500], \quad \alpha \in (0, 90) \text{ deg}, \quad \beta \in (0, 90) \text{ deg}. \quad (3.26)$$

Table 3.9 shows the results obtained considering parameters ranging in the domain (3.26). For what concern the design under only yielding constraints, the numerical results in Table 3.9 show that the global minimum is achieved for a complexity $q_Y^* \rightarrow \infty$ and for an aspect angle $\alpha_Y^* \rightarrow 45 \text{ deg}$, which corresponds to a minimal mass $\mu_Y^* \rightarrow 0.6427$ (Table 3.9). The optimizations for buckling constraints identify a global minimum for complexity $q_B^* \rightarrow \infty$ and for an aspect angle $\alpha_B^* \rightarrow 90 \text{ deg}$, which corresponds to a minimal mass $\mu_B^* \rightarrow 4.6151$ (Table 3.9).

Then, we let parameters n , q , α and β ranging in the following intervals:

$$n \in [1, 5], \quad q \in [1, 3], \quad \alpha \in (0, 90) \text{ deg}, \quad \beta \in (0, 90) \text{ deg}. \quad (3.27)$$

Refer to Table 3.10 for the results of the optimizations over the domain (3.27). For yielding constraints, the global minimum is obtained for complexities $n_Y^* = 1, q_Y^* = 3$ and for an aspect angle $\alpha_Y^* = 41.41 \text{ deg}$, which corresponds to a minimal mass $\mu_Y^* = 0.6614$ (Table 3.10). For the optimizations under buckling constraints, instead, we have obtained a global minimum for complexities $n_B^* = 1, p_B^* = 3$ and for an aspect angle $\alpha_B^* = 45.31 \text{ deg}$,

3. NUMERICAL RESULTS ON THE OPTIMAL DESIGN OF TENSEGRITY BRIDGES

n	q	α_Y^* [deg]	μ_Y^*	α_B^* [deg]	μ_B^*	$\mu_{B,s}^*$
1	1	35.26	0.7071	26.56	801.7357	0.1250
1	2	35.26	0.7071	36.22	514.7336	0.1231
1	3	41.41	0.6614	45.31	410.5778	0.2087
1	4	43.23	0.6514	51.70	346.8507	0.2326
1	5	43.96	0.6476	56.64	301.3080	0.2523
1	10	44.78	0.6437	70.63	181.3748	0.3101
1	15	44.91	0.6431	76.86	128.6606	0.3364
1	20	44.95	0.6429	80.19	99.3742	0.3505
1	25	44.97	0.6428	82.25	80.8126	0.3593
1	30	44.98	0.6428	83.56	68.0759	0.3649
1	35	44.98	0.6428	84.51	58.8000	0.3690
1	40	44.99	0.6428	85.23	51.7491	0.3721
1	45	44.99	0.6427	85.78	46.2113	0.3744
1	50	44.99	0.6427	86.21	41.7482	0.3763
1	100	45.00	0.6427	88.14	21.3224	0.3846
1	200	45.00	0.6427	89.07	10.9156	0.3886
1	300	45.00	0.6427	89.38	7.4204	0.3900
1	400	45.00	0.6427	89.53	5.6680	0.3907
1	500	45.00	0.6427	89.62	4.6151	0.3910

Table 3.9: Numerical results of superstructures with complexities $n = 1$ and different q under yielding ($_Y$) and combined yielding and buckling constraints ($_B$), ($F = 1 N$; $L = 1 m$; steel bars and steel cables).

which corresponds to a minimal mass $\mu_B^* = 410.5778$ (Table 3.10).

The optimizations for yielding conducted for the superstructure only bridges over the domains (3.26) and (3.27) allow to find a global minimum ($q_Y^* \rightarrow \infty$, $\alpha_Y^* \rightarrow 45 \text{ deg}$, $\mu_Y^* \rightarrow 0.6427$) that matches the minimum founded starting from *nominal* bridges and *substructure* only bridges. As validation of the adopted numerical solution, the here found global minimum corresponds to the result illustrated in Fig. 2 by [20]. It's interesting to note that the results under buckling constraints ($q_B^* \rightarrow \infty$, $\alpha_B^* \rightarrow 90 \text{ deg}$, $\mu_B^* \rightarrow 4.6151$) show that, differently for what obtained from the combined or the substructure

3. NUMERICAL RESULTS ON THE OPTIMAL DESIGN OF TENSEGRITY BRIDGES

n	q	α_Y^* [deg]	μ_Y^*	α_B^* [deg]	μ_B^*	$\mu_{B,s}^*$
1	1	35.26	0.7071	26.56	801.7349	0.1250
1	2	35.26	0.7071	36.22	514.7336	0.1231
1	3	41.41	0.6614	45.31	410.5778	0.2087
2	1	35.26	1.0607	26.56	1085.2	0.1875
2	2	35.26	1.0607	36.22	696.7464	0.2747
2	3	41.41	0.9922	45.31	555.7697	0.3130
3	1	35.26	1.2374	26.56	1185.4	0.2187
3	2	35.26	1.2374	36.22	761.1108	0.3204
3	3	41.41	1.1575	45.31	607.1179	0.3652
4	1	35.26	1.3258	26.56	1220.9	0.2343
4	2	35.26	1.3258	36.22	783.8740	0.3433
4	3	41.41	1.2402	45.31	625.2800	0.3913
5	1	35.26	1.3700	26.56	1233.4	0.2421
5	2	35.26	1.3701	36.22	791.9251	0.3548
5	3	41.41	1.2816	45.31	631.7049	0.4043

Table 3.10: Numerical results of superstructures with different complexities n and p under yielding (Y) and combined yielding and buckling constraints (B), ($F = 1$ N ; $L = 1$ m ; steel bars and steel cables).

bridges ($p_B^* = 1$, $\beta_B^* = 4.25$ deg, $\mu_B^* = 5.0574$), the optimal complexity q is at infinite. Moreover, it is worth noting that increasing complexity q allows a strong reduction of the mass, that is reducing from $\mu_B^* = 801.7357$ for $q = 1$ to $\mu_B^* = 4.6151$ for $q = 500$. Then, with the optimizations carried out in Sects. 3.3.1, 3.3.2 and 3.4.2, the case of a centrally loaded beam illustrated in Fig. 2 of [20] has been extended to accomplish the buckling case. Tables 3.7, 3.8 for substructure bridges and Tables 3.9, 3.10 for superstructure bridges also show the total masses of cables ($\mu_{B,s}^*$) obtained under buckling for each optimized case. We show that, for the substructures, the total mass of the cables ($\mu_{B,s}^*$) is the most part of the total mass of the structure under buckling (μ_B^*). For the case $n = q = p = 1$, eg., $\mu_{B,s}^*/\mu_B^* = 0.67$ for the substructure (see Table 3.7) while $\mu_{B,s}^*/\mu_B^* = 1.56x10^{-4}$ for the superstructure (see Ta-

3. NUMERICAL RESULTS ON THE OPTIMAL DESIGN OF TENSEGRITY BRIDGES

ble 3.9). This makes clear that the substructure bridges under buckling work mainly with cables and the length and the forces (and then the mass) of the bars can be extremely reduced playing with the aspect angle β . Moreover, Table 3.9 shows that the global minimum for buckling for the superstructure ($q_B^* \rightarrow \infty$, $\alpha_B^* \rightarrow 90 \text{ deg}$, $\mu_B^* \rightarrow 4.6151$) corresponds to a maximum of the ratio $\mu_{B,s}^*/\mu_B^* = 0.085$ over the domain (3.26).

3.4 Bridge model with deck

In the present Section, we report numerical results of the tensegrity bridges defined in Chap. 2 including deck mass and joints mass. Taking into account the results obtained in the case without deck, we performed the numerical simulation only for buckling constraints, since it has been shown that this is the mode of failure in all cases. Moreover, the optimizations will be performed only for *substructure* bridges (Sect. 3.4.1) and *superstructure* bridges (Sect. 3.4.2) and not for *nominal* bridges, since these optimizations bring to solutions keeping only substructure. The numerical results are presented in terms of μ_d^* , $\mu_{B,S}^*$, $\mu_{B,tot}^*$, α_B^* and β_B^* denoting respectively the mass of deck ($2^n m_d \sigma_s / (\varrho_s F L)$), the mass of the bridge structure, the total minimal mass including bridge structure, deck and joints ($\mu_{B,S}^* + \mu_d^* + \mu_J^*$) and the optimal aspect angles. The total mass of joints μ_J^* is computed as the product between the number of joints (n_n) and a fixed joint factor (Ω). The results are obtained numerically through the MatLab[®] program written employing the algorithm illustrated in Sect. 3 of [141]. The optimization problems presented in Tables 3.11, 3.12 are solved assuming $L = 30 \text{ m}$, $F = 450 \text{ kN}$, deck mass computed as defined in (2.150), steel for bars and deck beams, Spectra[®] for cables (refer to Table 4.1 for the material properties; $\varrho = 31.72$; $\eta = 1216.55$). In all the optimized cases, we set step increments of complexities n , p and q to 1 and step increments of 0.01 deg for the aspect angles α and β .

3.4.1 Substructures

In this Section, we show the results obtained for the optimizations of the *substructure* bridges showed in Fig. 4.4 including deck and joints masses. First of all, we let parameters n , p , α and β ranging in the following intervals:

$$n \in [1, 5], \quad p \in [1, 3], \quad \alpha \in (0, 90) \text{ deg}, \quad \beta \in (0, 90) \text{ deg}. \quad (3.28)$$

A first set of results are presented in Table 3.11 in which we didn't consider jet joint masses. The global minimum in the domain (3.28) is obtained for complexities $n_B^* = 5$, $p_B^* = 1$ and for an aspect angle $\beta_B^* = 4.11 \text{ deg}$, which corresponds to a total minimal mass $\mu_{B,tot}^* = 334.7613$ (Table 3.11).

The results in Table 3.11 identify an optimal complexity n lying on the boundary of the domain (3.28). Then we have performed another optimization keeping $p = 1$ and increasing only complexity n . In this case, since the number of nodes given in (4.5) is exponentially increasing with n , the numerical simulation of such structure would be computationally heavy. For that reason, we made use of the analytical solution given in Theorem 4.4.1. In this case, we have also added the mass of joints considering increasing values of the joint factor Ω and the results are showed in Fig. 3.8. The red curve reports the masses of substructure bridge only ($\mu_{B,S}^*$), the solid curve is the total mass without joints and the dashed and dotted curves include the joint masses. We obtained a finite complexity n ranging between 11 and 12 considering joint masses.

3.4.2 Superstructures

In this Section, we show the results obtained for the optimizations of the *superstructure* bridges showed in Fig. 2.5 including deck and joints masses.

3. NUMERICAL RESULTS ON THE OPTIMAL DESIGN OF TENSEGRITY BRIDGES

n	p	μ_d^*	β_B^* [deg]	$\mu_{B,S}^*$	$\mu_{B,tot}^*$
1	1	6659.9	4.13	8.8585	6668.8
1	2	6659.9	3.69	9.9260	6669.9
1	3	6659.9	3.47	10.5649	6670.5
2	1	2917.9	4.09	10.3025	2928.2
2	2	2917.9	3.66	11.5443	2929.5
2	3	2917.9	3.44	12.2875	2930.2
3	1	1364.3	4.09	10.5151	1347.8
3	2	1364.3	3.66	11.7826	1376.1
3	3	1364.3	3.43	12.5411	1376.9
4	1	659.5	4.10	10.5120	670.0878
4	2	659.5	3.66	11.7791	671.3548
4	3	659.5	3.44	12.5373	672.1131
5	1	324.28	4.11	10.4841	334.7613
5	2	324.28	3.67	11.7459	336.0232
5	3	324.28	3.45	12.5021	336.7793

Table 3.11: Numerical results of substructures with deck for different complexities n and p under buckling constraints ($_B$), ($F = 450 \text{ kN}$; $L = 30 \text{ m}$; $w_d = 3 \text{ m}$, steel bars and deck, Spectra[®]- UHMWPE cables).

First of all, we let parameters n , q , α and β ranging in the following intervals:

$$n \in [1, 5], \quad q \in [1, 3], \quad \alpha \in (0, 90) \text{ deg}, \quad \beta \in (0, 90) \text{ deg}. \quad (3.29)$$

A first set of results are presented in Table 3.12 in which we didn't consider jet joint masses. The global minimum in the domain (3.29) is obtained for complexities $n_B^* = 5$, $p_B^* = 3$ and for an aspect angle $\alpha_B^* = 45.31 \text{ deg}$, which corresponds to a total minimal mass $\mu_{B,tot}^* = 1235.3$ (Table 3.12).

We then fix parameter $n = 5$, and let q , α and β ranging in the following

3. NUMERICAL RESULTS ON THE OPTIMAL DESIGN OF TENSEGRITY BRIDGES

intervals:

$$q \in [1, 50], \quad \alpha \in (0, 90) \text{ deg}, \quad \beta \in (0, 90) \text{ deg}. \quad (3.30)$$

Results of such optimizations are reported in Table 3.13, in which we didn't consider joint masses. The global minimum in the domain (3.30) is obtained for complexities $n_B^* = 5$, $p_B^* = 50$ and for an aspect angle $\alpha_B^* = 86.21 \text{ deg}$, which corresponds to a total minimal mass $\mu_{B,tot}^* = 416.8388$ (Table 3.13).

The results in Table 3.13 identify an optimal complexity q lying on the boundary of the domain (3.30). It is worth noting that the above solution is without joint masses. Then, we have performed another optimization over the same domain (3.30) but considering joint masses with increasing joint factor Ω and their results are showed in Fig. 3.9. The red curve reports the masses of superstructure bridge ($\mu_{B,S}^*$), the solid curve is the total mass without joints and the dashed and dotted curves include the joint masses. We obtained a finite complexity q ranging between 10 and 20 considering joint masses. It must be noticed that, however, the minimum mass obtained with superstructure is bigger then the minimum mass obtained with the substructure, that has been confirmed as the most convenient bridge.

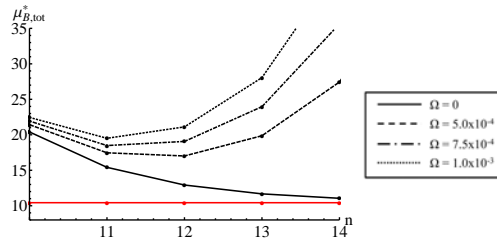


Figure 3.8: Total masses ($\mu_{B,tot}^*$, black curves) for different values of the joint factor Ω and structural masses ($\mu_{B,S}^*$, red curves) under buckling constraints for $p = q = 1$ and different n .

3. NUMERICAL RESULTS ON THE OPTIMAL DESIGN OF TENSEGRITY BRIDGES

n	q	μ_d^*	α_B^* [deg]	$\mu_{B,S}^*$	$\mu_{B,tot}^*$
1	1	6659.9	26.56	1484.5	8144.4
1	2	6659.9	36.22	953.0505	7613.0
1	3	6659.9	45.31	760.1925	7420.1
2	1	2917.9	26.56	1760.7	4678.6
2	2	2917.9	36.22	1130.4	4048.3
2	3	2917.9	45.31	901.6280	3819.6
3	1	1364.3	26.56	1798.5	3162.8
3	2	1364.3	36.22	1154.7	2519.0
3	3	1364.3	45.31	921.0011	2285.3
4	1	659.5	26.56	1790.9	2450.5
4	2	659.5	36.22	1149.8	1809.4
4	3	659.5	45.31	917.1257	1576.7
5	1	324.25	26.56	1779.1	2103.4
5	2	324.25	36.22	1142.2	1466.5
5	3	324.25	45.31	911.0597	1235.3

Table 3.12: Numerical results of superstructures with deck for different complexities n and q under buckling constraints (B), ($F = 450 \text{ kN}$; $L = 30 \text{ m}$; $w_d = 3 \text{ m}$, steel bars and deck, Spectra[®]- UHMWPE cables).

3.5 Bridge constrained with a fixed hinge and rolling hinge (HR)

This Section reports some numerical results for the cases of *nominal*, *substructure* and *superstructure* bridges illustrated in Chap. 2 and constrained with a fixed hinge at one end and a rolling hinge at the other end. Both the optimization under yielding and under buckling constraints are illustrated. Table 3.14 shows the results obtained for the *nominal* bridges, Table 3.15 shows the results obtained for the *substructure* and Table 3.16 shows the results obtained for the *superstructure*. For the HR case, the deck elements play an important role stabilizing the structure. For HR constraints, the so-called *bi-directional* elements must be used since deck elements can be contemporary cables or

3. NUMERICAL RESULTS ON THE OPTIMAL DESIGN OF TENSEGRITY BRIDGES

n	q	μ_d^*	α_B^* [deg]	$\mu_{B,S}^*$	$\mu_{B,tot}^*$
5	1	324.28	26.56	1779.1	2103.4
5	2	324.28	36.22	1142.2	1466.5
5	3	324.28	45.31	911.0597	1235.3
5	4	324.28	51.71	769.6990	1093.9
5	5	324.28	56.64	668.5721	992.8493
5	10	324.28	70.64	402.4183	726.6955
5	15	324.28	76.86	285.4356	609.7128
5	20	324.28	80.19	220.3840	544.6612
5	25	324.28	82.21	179.2518	503.5291
5	30	324.28	83.56	150.9876	475.2646
5	35	324.28	84.52	130.4024	454.6796
5	40	324.28	85.23	114.7554	439.0326
5	45	324.28	85.78	102.4660	426.7433
5	50	324.28	86.21	92.5615	416.8388

Table 3.13: Numerical results of superstructures with deck for $n = 5$ and different complexities q under buckling constraints (B), ($F = 450 \text{ kN}$; $L = 30 \text{ m}$; $w_d = 3 \text{ m}$, steel bars and deck, Spectra[®]- UHMWPE cables).

bars (see [145], [141]).

3. NUMERICAL RESULTS ON THE OPTIMAL DESIGN OF TENSEGRITY BRIDGES

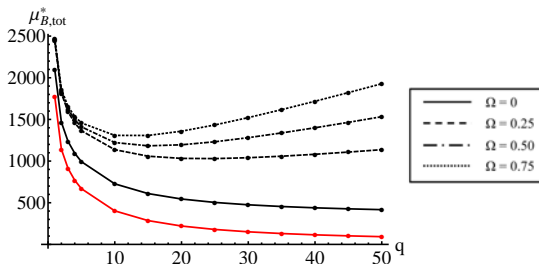


Figure 3.9: Total masses ($\mu_{B,tot}^*$, black curves) for different values of the joint factor Ω and structural masses ($\mu_{B,s}^*$, red curve) under buckling constraints for $n = 5$ vs q for superstructure.

3.6 Discussion

We have presented a numerical design methodology for tensegrity bridges, which is aimed to the generation of minimum mass shapes through parametric self-similar iterations. It makes use of basic units consisting of Michell trusses carrying a central point load [20, 12, 29]; compressed arches above the deck level; and tensile cords below the deck. The proposed design procedure is ruled by two complexity parameters (n and p), two aspect angles (α and β), and admits either combined buckling and yielding constraints, or, as a special case, simple yielding constraints. The results presented in Sect. 3.3 point out that the global minimum mass configuration of the examined bridge model shows finite complexity n , and markedly large or infinite complexity p .

3. NUMERICAL RESULTS ON THE OPTIMAL DESIGN OF TENSEGRITY BRIDGES

n	$p = q$	α_Y^* [deg]	β_Y^* [deg]	μ_Y^*	α_B^* [deg]	β_B^* [deg]	μ_B^*
1	1	35.26	35.26	0.707	16.31	29.37	592.154
1	2	35.26	35.26	0.707	33.46	21.25	447.577
1	3	41.41	41.41	0.661	43.42	15.75	380.153
1	4	43.23	43.23	0.651	50.35	12.14	330.506
1	5	43.96	43.96	0.648	55.61	9.78	291.635
1	6	44.32	44.32	0.646	59.79	8.09	260.365
1	7	44.52	44.52	0.645	63.18	6.86	234.711
1	8	44.65	44.65	0.644	65.98	5.93	213.346
1	9	44.73	44.73	0.644	68.32	5.17	195.321
1	10	44.79	44.78	0.644	70.29	4.57	179.943
1	15	44.91	44.91	0.643	76.71	2.70	128.319
1	20	44.96	44.98	0.643	80.12	1.82	99.240
1	25	44.96	44.98	0.643	82.18	1.37	80.763
1	30	44.97	44.99	0.643	83.54	1.01	68.061
1	35	44.97	44.99	0.643	84.51	0.90	58.799
1	40	44.98	45.00	0.643	85.22	0.73	51.754
1	45	44.98	45.00	0.643	85.78	0.61	46.219
1	50	44.98	45.00	0.643	86.22	0.55	41.758

Table 3.14: Numerical results of nominal bridges constrained with a fixed hinge and a rolling hinge (HR) and with complexities $n = 1$ and different $p = q$ under yielding (Y) and combined yielding and buckling constraints (B), ($F = 1 N$; $L = 1 m$; steel bars and steel cables).

We can therefore conclude that such a bridge shows a multiscale, discrete-continuum complexity. In all the examined cases, we have observed that the minimum mass of the bridge under simple yielding constraints is about two orders of magnitude smaller than the minimum mass corresponding to combined buckling and yielding constraints. This implies that buckling failure cannot be ignored in practical applications of the present design methodology. Concerning the aspect ratios of the bridge, we have observed that, as the complexity n increases, the height of the portion of the bridge placed above the deck increases, while the height of the structure placed below the deck decreases dramatically. We wish to highlight that the present minimum mass designs cannot be understood as universal optima, under the given constraints. They indeed represent mass minimizers within the examined sets of bridge topolo-

3. NUMERICAL RESULTS ON THE OPTIMAL DESIGN OF TENSEGRITY BRIDGES

p	$n = 1$				$n = 2$			
	β_Y^* [deg]	μ_Y^*	β_B^* [deg]	μ_B^*	β_Y^* [deg]	μ_Y^*	β_B^* [deg]	μ_B^*
1	45.00	1.000	33.42	660.522	45.00	1.500	25.69	474.588
2	45.00	1.000	36.56	668.307	45.00	1.500	25.25	494.442
3	45.25	0.912	35.28	691.574	60.00	1.299	23.73	513.060
4	67.50	0.828	32.88	716.173	67.50	1.243	22.30	529.458
5	72.00	0.812	31.02	736.332	72.00	1.218	21.21	542.791
6	75.00	0.804	29.59	753.097	75.00	1.206	20.36	553.928
7	77.14	0.799	28.45	767.398	77.14	1.198	19.67	563.481
8	78.75	0.796	27.51	779.861	78.75	1.193	19.09	571.847
9	80.00	0.793	26.72	790.909	80.00	1.190	18.60	579.295
10	81.00	0.792	26.04	800.834	81.00	1.188	18.17	586.010
15	84.00	0.788	23.63	839.445	84.00	1.182	16.63	612.330
20	85.50	0.787	22.11	867.300	85.50	1.181	15.64	631.487
25	86.40	0.786	21.01	889.214	86.40	1.180	14.91	646.642
30	87.00	0.786	20.17	907.341	87.00	1.179	14.34	659.224
35	87.43	0.786	19.49	922.833	87.43	1.179	13.88	670.010
40	87.75	0.786	18.92	936.383	87.75	1.179	13.50	679.464
45	88.00	0.786	18.44	948.441	88.00	1.179	13.17	687.893
50	88.18	0.786	18.02	959.313	88.20	1.178	12.88	695.504

Table 3.15: Numerical results of substructures constrained with a fixed hinge and a rolling hinge (HR) with different complexities n and p under yielding (Y) and combined yielding and buckling constraints (B), ($F = 1 N$; $L = 1 m$; steel bars and steel cables).

gies, against which other bridge designs could be usefully compared to.

3. NUMERICAL RESULTS ON THE OPTIMAL DESIGN OF TENSEGRITY BRIDGES

q	$n = 1$				$n = 2$			
	α_Y^* [deg]	μ_Y^*	α_B^* [deg]	μ_B^*	α_Y^* [deg]	μ_Y^*	α_B^* [deg]	μ_B^*
1	45.00	1.000	26.58	802.235	45.00	1.500	26.58	1085.960
2	45.00	1.000	36.24	515.075	45.00	1.500	36.24	697.258
3	60.00	0.866	45.32	410.825	60.00	1.299	45.32	556.141
4	67.50	0.828	51.72	347.048	67.50	1.243	51.72	469.811
5	72.00	0.812	56.65	301.473	72.00	1.218	56.65	408.120
6	75.00	0.804	60.60	266.610	75.00	1.206	60.60	360.931
7	77.14	0.799	63.82	238.878	77.14	1.198	63.83	323.393
8	78.75	0.796	66.50	216.235	78.75	1.193	66.50	292.744
9	80.00	0.794	68.75	197.388	80.00	1.190	68.75	267.234
10	81.00	0.792	70.65	181.463	81.00	1.188	70.65	245.678
15	84.00	0.788	76.88	128.719	84.00	1.182	76.88	174.286
20	85.50	0.787	80.21	99.391	85.50	1.181	80.21	134.588
25	86.40	0.786	82.23	80.847	86.40	1.180	82.23	109.488
30	87.00	0.786	83.58	68.104	87.00	1.179	83.58	92.240
35	87.43	0.786	84.53	58.824	87.43	1.179	84.53	79.679
40	87.75	0.786	85.24	51.770	87.75	1.179	85.24	70.131
45	88.00	0.786	85.79	46.223	88.00	1.179	85.79	62.632
50	88.18	0.786	86.23	41.765	88.20	1.178	86.23	56.588

Table 3.16: Numerical results of superstructures constrained with a fixed hinge and a rolling hinge (HR) with different complexities n and q under yielding (Y) and combined yielding and buckling constraints (B), ($F = 1 N$; $L = 1 m$; steel bars and steel cables).

The present study opens the way for a variety of further applications of tensegrity structures in civil engineering and parametric architecture, where the tensegrity ‘philosophy’ has only been partially exploited at present (cf. also [13, 22]). Particularly challenging is the use of parametric tensegrity design for the next generation long span or pedestrian bridges, which might require smart structures based on lightweight materials, active or passive control strategies, and/or real-time structural health monitoring [24]. Tensegrity applications also calls for a robust design to take care of errors on members’ manufactured lengths. These errors may lead to members’ over-stressing and to a construction not replicating the exact theoretical structure, and could even produce instabilities. Developments in this direction constitute a ripe

3. NUMERICAL RESULTS ON THE OPTIMAL DESIGN OF TENSEGRITY BRIDGES

subject for future studies. We also address to future work the realization of real-scale or reduced-scale physical models of tensegrity bridges, as well as the 3D generalization of the proposed design approach. Further generalizations of the present study might regard the adoption of different objective functions (minimum compliance, fabrication and assembly cost, integrated mechanical, functional, and architectural performance criteria, etc.), the adoption of optimization strategies based on evolutionary form-finding methods [17, 31, 19], or the lumped stress method [15, 16], and an enlargement of the present numerical analysis to more complex search domains and real case studies. Regarding the adoption of a different objective function, we are currently refining computations by using a global cost function, where different contributions, such as the cost of material, fabrication, and assembly, are customarily weighted and summed together. An interesting challenge is the modeling of a trade-off between these different costs, since lightweight and easy-to-assemble components would also be more expensive to design and manufacture.

4

Optimal Design of Solar Energy Harvesting Bridge Structures

4.1 Introduction

To stop the evaporation losses, reports have shown [142] the economic benefits of covering the aqueducts that bring water to California from the Colorado River. It is also logical that the chosen cover could be solar panels to generate energy without requiring new land, (contrary to the requirements of wind turbines or large solar farms). The Narmanda Canal in Gujarat India already has a solar panel covered aqueduct since 2012, but the design of the truss support structure is massive and costly, see Fig 1. To determine the true achievable benefits of such a concept one must engineer the support system to use the smallest amount of material possible, and then reconsider the economic projections. This Chapter provides the minimal mass solution to the solar panel support structure.

Tensegrity structures are very efficient, and tend to provide minimal mass solutions to structure design under certain conditions. We propose a tensegrity bridge design that has minimal mass among all possible tensegrity topologies (configurations of members). Some tensegrity papers have shown minimal mass for tensile structures, subject to a stiffness constraint [28]. Some have shown minimal mass for: compressive loads [25], cantilevered bending loads [26], torsional loads [27], simply-supported bending loads [135], and distributed loads on simply-supported spans, where significant structure is not allowed below the roadway, [141]. Of course, minimal mass bridges are not new ideas. Michell in 1904 derived the minimal mass simply-supported structure, subject to yield constraints. His result is a continuum in which the lines of tensile stress and the lines of compressive stress are perpendicular. This bridge rises very high above the water (for a span = L , the height above water = $0.35L$). This height would invite large loads from desert winds. Furthermore, yielding is not the mode of failure when the number of structural members is finite, rather than infinite (infinite members constitutes a continuum), and practical construction always creates joint mass that further reduces the complexity of the minimal mass realization of the bridge. Bridge designs that are subject to

4. OPTIMAL DESIGN OF SOLAR ENERGY HARVESTING BRIDGE STRUCTURES

buckling constraints are required, and will be used to produce minimal mass designs under practical conditions. The great advantage of these optimizations for the aqueduct cover is that these minimal mass solutions have flat roofs (no superstructure, only structure below the horizontal), and very streamlined cross sections, that tolerate high winds. They are also light-weight and easily deployable.

The present study deals with the minimum mass design of 3D networks of deployable tensegrity structures carrying vertical loads (PV panels) distributed over the surface of the solar array. The examined structures are designed to generate power and work as horizontal shading devices for water canals, reducing or eliminating water evaporation. A deck made of solar panels is supported by a special truss support system with tensegrity architecture, and these are connected through a stabilizing network of cables. The deck of solar panels serves as a deployable solar roof.

The present structures combine the shading effects of an horizontal shading device with the energy harvesting capabilities of solar thermal collectors and/or photo-voltaic panels, which ensure at the same time solar energy harvesting (conversion of solar energy into heat and/or electricity).

A shading device is realized through a 3D network of horizontal tensegrity modules supporting a roof of solar (thermal and/or photo-voltaic) panels. The network is foldable and deployable and is controlled by stretching or relaxing the transverse cables. A minimum mass design leads to lightweight structures easily deployed and maneuverable to aid construction, assembly, servicing, and repair.

The application of interest in this study is in any canal which brings water to cities that are long distances from a river. As an example, we compute the design for a 400 mile canal bringing water to San Diego from the Colorado River. The technical goal is two-fold: i) to stop or reduce the evaporative losses in such canals, and ii) to use the space above the canal to generate power using solar panels. This is not a new idea. The 2014 UCLA study [142] discusses some of the economic issues. The website [143] describes the efforts in India,

4. OPTIMAL DESIGN OF SOLAR ENERGY HARVESTING BRIDGE STRUCTURES

where they have actually built such systems and have data since 2012. The UCLA report suggests environmental improvements and challenges. The India report demonstrates feasibility with systems that have been operational since 2012. However this report uses very substantial bridge structures to support the solar panels. These structures are costly to build, erect, and repair. We seek a system using minimal material resources, and a deployment strategy that erects the light-weight structure. Our motivation is to reduce engineering and construction costs, in hopes that the most efficient system would alter the political and economic equations enough to justify such projects. We propose to design a support structure for a solar array that covers long canals. The panels will not be exactly flat to allow water runoff. Neither the panels nor the support structure will touch the water.

4.2 Description of the Model

The minimal mass of a cable with loaded length s , yield strength σ_s , mass density ρ_s , and maximal tension t_s is:

$$m_s = \frac{\rho_s}{\sigma_s} t_s s. \quad (4.1)$$

To avoid buckling, the minimal mass of a round bar of length b , modulus of elasticity E_b , and maximal force f_b is:

$$m_{b,B} = 2\rho_b b^2 \sqrt{\frac{f_b}{\pi E_b}}. \quad (4.2)$$

In the designs, we will assume buckling as a mode of failure of compressive members since it has been shown in [135] that buckling is the mode of failure in most of the practical cases, and indeed, in our design.

Lemma 4.2.1. *Minimal mass designs subject to only buckling constraints*

4. OPTIMAL DESIGN OF SOLAR ENERGY HARVESTING BRIDGE STRUCTURES

automatically also satisfy yielding constraints if,

$$\frac{f_b}{b^2} < \frac{4\sigma_b^2}{\pi E_b}. \quad (4.3)$$

The paper [135] finds the tensegrity bridge (planar) that minimizes the sum of deck mass, structural mass, and joint mass. The solution is a Class 1 tensegrity structure (compressive members do not make contact) with an optimal *complexity* (optimal number of structural members) that is finite. That is, the optimal structure is not a continuum (in contrast to the Michell truss) but a discrete structure with an optimal number of elements. This optimal number depends on material choice, the span, and the external load. This optimal bridge has no structure above the horizontal line (we call this a *substructure bridge*). This study assures that the most efficient structure does not extend above horizontal, making it ideal for our proposed solar array surface, since the surface is horizontal, and does not generate any shadows on the solar panels.

For a water canal application, Fig. 4.1 shows a 3D deployable flat roof made of repetitive 2D *substructure* bridges with multiscale topology defined in Fig. 4.2. Each planar *substructure* bridge is constrained with two fixed hinges at both ends (in practice these hinges might be pulleys that allow roll-up during construction or repair). As illustrated in Fig. 4.1, this module can be replicated (along the longitudinal direction) to build a deployable three-dimensional structure able to carry vertical loads distributed on the horizontal plane of the solar array. Fig. 4.3 shows a possible application of this module to water canals.

4.3 Description of the Deployment Scheme

Two different deployment features are incorporated into this design; one for construction, and one for maintenance (Fig 1). We will call the motion for construction, *transverse deployment*, described as follows. Since the network

4. OPTIMAL DESIGN OF SOLAR ENERGY HARVESTING BRIDGE STRUCTURES

is a class 1 tensegrity (no bars in contact) one can roll up the cables. Imagine the truss system (before the solar panels are installed) rolled up on a large reel of inner radius R_0 and radius after rollup R . To compute the required radius of the reel, let L be the cable length required to cross the canal, let r be the cable radius, let v be the number of revolutions required to rollup a cable of length L . The radius of the reel after rollup is $R = R_0 + 2vr$, and the length of the cable rollup up is L . Hence, $L = 2\pi \sum_v (R_0 + 2ir) = 2\pi(vR_0 + rv(v+1))$.

Then one can show that the required radius of the reel is:

$$\begin{aligned} R &= R_0 + 2vr \\ &= 3R_0 + 2r[-1 + \sqrt{1 + \frac{2L}{\pi r(1 + \frac{R_0}{r})^2}}]. \end{aligned} \quad (4.4)$$

The width of the reel is equal to the length of the longest bar in the bridge truss network (about 1 meter for a 20 meter span). One end of the reeled bridge network is secured to the bank foundation (at the reel location) and the other end attached to a cable across the water on the opposite bank. By pulling this cable across the canal the truss network unreels across the canal. In succession, as the truss is pulled across (while maintaining sufficient tension to remain above water level), the solar panels can be installed (attached to the cables) at the canal bank as the cable pulls the network across the canal.

The second type of deployment is perpendicular to the first one, and is called the *longitudinal deployment*, see Fig 4.1. This deployment is along the centerline direction of the canal. After a disconnection at the edge of a damaged section, this deployment can create an opening of the array to allow access to the water for any reason, such as cleaning, servicing, removing debris from the water, or repairing solar panels.

This longitudinal deployability is assured by controlling the actual aspect angle α . This angle is controlled by a motor that turns a tire on a level concrete track, to roll the bridge sections closer to each other (for servicing or

4. OPTIMAL DESIGN OF SOLAR ENERGY HARVESTING BRIDGE STRUCTURES

repair), or further apart (for deployment to operational configuration). The angle $\alpha = \alpha_d$, where α_d is a small angle (about 2 degrees), determined by the tension selected for the diagonal cables supporting the panels. Hence, the solar panels face vertical within 2 deg.

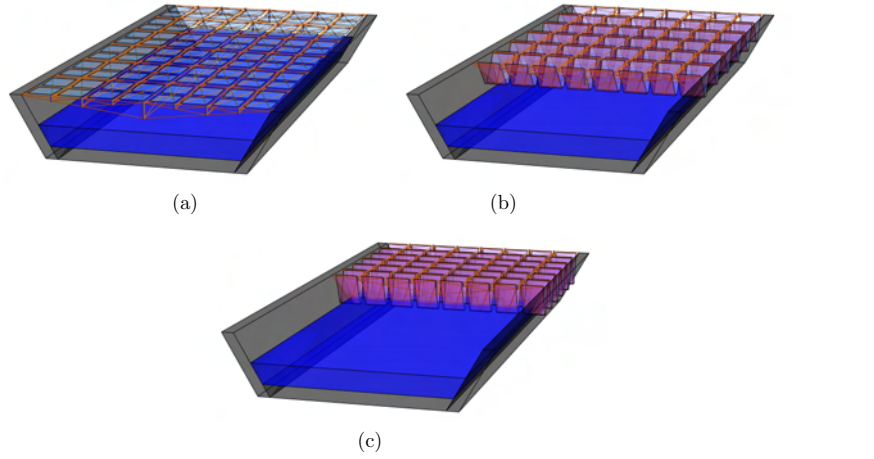


Figure 4.1: Different configurations of a deployable solar roof for water canals: (a) open onfiguration, (b) transition between open/closed configurations, (c) closed configuration.

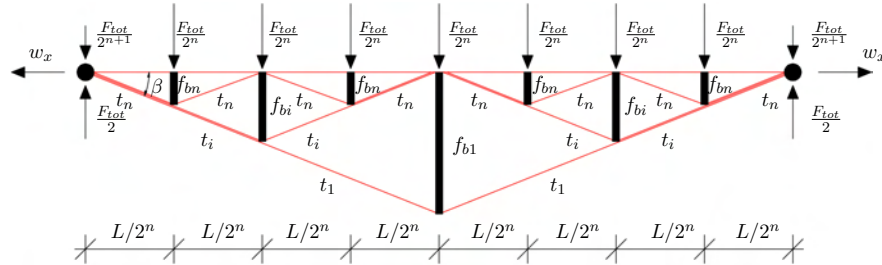


Figure 4.2: Adopted notations for forces and lengths of bars and cables for a substructure with generic complexity $(n, p, q) = (n, 1, 0)$.

The planar bridge topology is considered here to elucidate the fundamental properties that are important in the vertical plane. We use the following nomenclature, referring to Figs. 4.2 and 4.3:

4. OPTIMAL DESIGN OF SOLAR ENERGY HARVESTING BRIDGE STRUCTURES

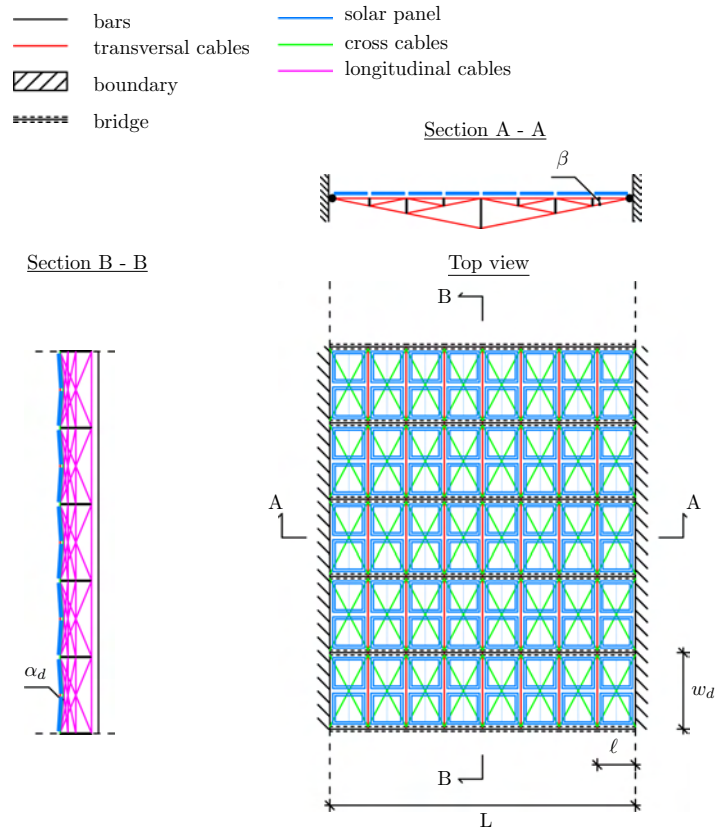


Figure 4.3: Schematic of a deployable tensegrity system with solar panel.

- A *substructure* bridge has no structure above the deck level.
- n means the number of self-similar iterations involved in the design ($n \geq 1$ in Fig. 4.4).
- p means the complexity of each iteration in the substructure ($p \geq 1$ in Fig 4.4).
- β is the aspect angle of the *substructure* measured from the horizontal.

For a tensegrity bridge with generic complexities n and p (see Fig. 4.2), the total number of nodes n_n of each topology is given by:

4. OPTIMAL DESIGN OF SOLAR ENERGY HARVESTING BRIDGE STRUCTURES

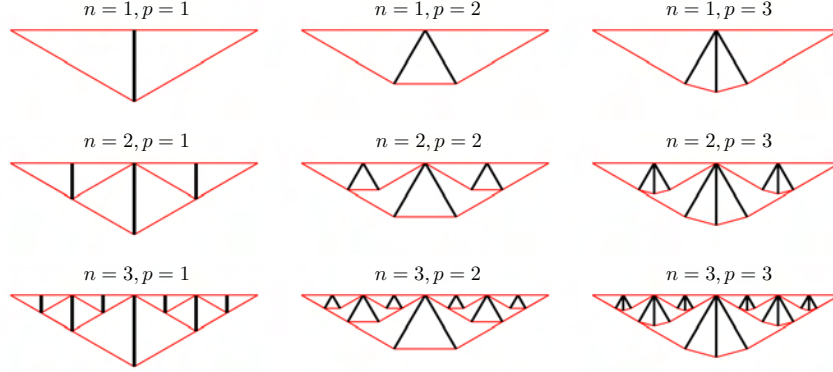


Figure 4.4: Exemplary geometries of the substructures for different values of the complexity parameters n (increasing downward) and p (increasing leftward).

$$n_n = p(2^n - 1) + 2^n + 1. \quad (4.5)$$

For the *substructure* bridge, the number of bars n_b and the number of cables n_s are:

$$n_b = p(2^n - 1), \quad n_s = (p + 1)(2^n - 1) + 2^n. \quad (4.6)$$

The bridge structures must be stabilized out of the plane with a set of longitudinal cables as illustrated in Fig. 4.3. In particular diagonal vertical cables and horizontal longitudinal cables (the magenta element showed in Section B-B of Fig. 4.3) are used to prevent out of plane vertical movement. The deck is composed of different orders of cables (refer to Figs. 4.3, 4.5):

- longitudinal cables: the elements connecting each tensegrity bridge unit along the length of the canal;
- transversal cables: the elements of each tensegrity bridge lying on the transversal direction;
- cross cables: the elements that directly carry the solar panel loads and

4. OPTIMAL DESIGN OF SOLAR ENERGY HARVESTING BRIDGE STRUCTURES

transfer their weight to the bridge structures.

Let F be the total external vertical load for the solar panels to be carried by one planar bridge structure. Each deck section will be loaded by:

$$f_p = \frac{F}{2n}. \quad (4.7)$$

It will be convenient to define the following constant:

$$\eta = \frac{\varrho_b L}{(\varrho_s/\sigma_s) \sqrt{\pi E_b F}}, \quad (4.8)$$

and define a normalization of the system mass m by the dimensionless quantity μ :

$$\mu = \frac{m}{(\varrho_s/\sigma_s) FL}. \quad (4.9)$$

The total vertical force F_{tot} can be computed designing the deck diagonal cables represented in Fig. 4.5. These cables directly support two different solar panel modules of sizes ℓ by $w_d/2$ (see Fig. 4.5). We design these cables assuming that, at the fully-deployed configuration of the structure, the deck diagonal cables are inclined at a fixed angle α_d with the respect to the horizontal (Fig. 4.5). At this configuration the tensile force in each deck diagonal cable is:

$$t_d = \frac{f_p}{4 \sin \alpha_d}, \quad (4.10)$$

and the length of each cable is:

$$s_d = \frac{\sqrt{w_d^2 + \ell^2}}{2 \cos \alpha_d}. \quad (4.11)$$

By using the Eq. 4.1 we can compute the total mass of the deck diagonal

4. OPTIMAL DESIGN OF SOLAR ENERGY HARVESTING BRIDGE STRUCTURES

cables as:

$$m_d = 4 \frac{\rho_d}{\sigma_d} t_d s_d = \frac{\rho_d f_p}{\sigma_d} \frac{\sqrt{w_d^2 + \ell^2}}{2 \sin \alpha_d \cos \alpha_d}. \quad (4.12)$$

Then, the normalized total mass of the deck structure is:

$$\mu_d^* = \frac{2^n m_d}{(\rho_s/\sigma_s) FL}. \quad (4.13)$$

The total force acting on each internal node on the deck is then the sum of the forces due to the external loads and the force due to the deck load.

$$F_{tot} = F + 2^n m_d g. \quad (4.14)$$

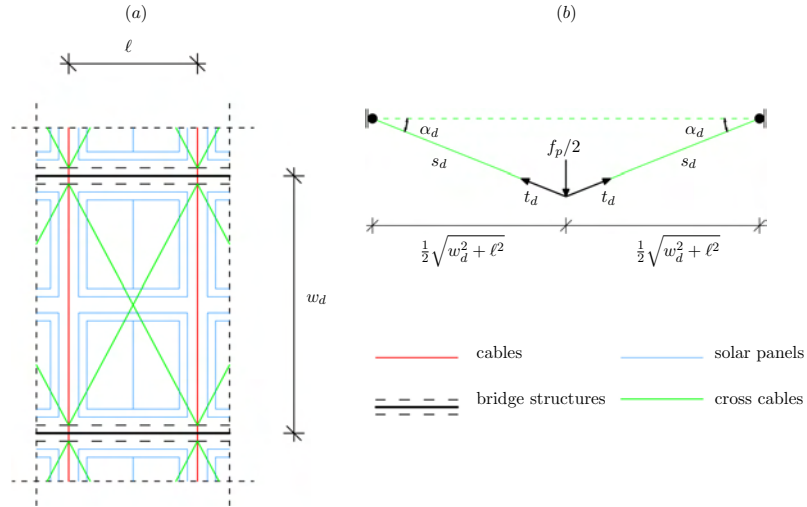


Figure 4.5: Details of the canal structure: (a) deck system, (b) deformed shape of the deck cross cables subjected to the solar panel force.

4.4 Analytical Results

In this section we study the minimal mass of bridges with complexity n . We make use of the notation illustrated in Fig. 4.2 in which complexity p is fixed to be one. Each iteration $n = 1, 2, \dots$ generates different lengths of bars and cables. We need not consider $p > 1$ because the *Corollary 4.5* in [135] shows that $p = 1$ is the minimal mass solution of a simply-supported *substructure* bridge under buckling constraints. The lengths at the i^{th} iteration are:

$$b_i = \frac{L}{2^i} \tan \beta, \quad i = 1 - n, \quad (4.15)$$

$$s_i = \frac{L}{2^i \cos \beta}, \quad i = 1 - n. \quad (4.16)$$

Observing the multi-scale structure of Fig. 4.2 it's clear that the number of bars and the number of cables at the i^{th} self-similar iteration are

$$n_{si} = 2^i, \quad n_{bi} = 2^{i-1}. \quad (4.17)$$

In this case the total force applied to the bridge structure is given by (4.14) and then the forces in each member become:

$$f_{bi} = \frac{F + 2^n m_d g}{2^i}, \quad t_{si} = \frac{F + 2^n m_d g}{2^{(1+i)} \sin \beta}. \quad (4.18)$$

Finally we can compute the total mass m_B at the buckling condition as:

$$m_B = \frac{2\rho_b}{\sqrt{\pi E_b}} \sum_{i=1}^{n_b} b_i^2 \sqrt{f_{b,i}} + \frac{\rho_s}{\sigma_s} \sum_{i=1}^{n_s} t_i s_i, \quad (4.19)$$

4. OPTIMAL DESIGN OF SOLAR ENERGY HARVESTING BRIDGE STRUCTURES

where (b_i, s_i) is respectively the length of the i^{th} bar or cable, and $(f_{b,i}, t_i)$ is respectively the force in the i^{th} bar or cable.

Theorem 4.4.1. *Consider a substructure bridge with topology defined by (4.5), (4.6), (4.15) and (4.16), with complexity n . The minimal mass design under yielding and buckling constraints is given by:*

$$\mu_B^* = \beta_1 \frac{(1 + \tan^2 \beta_B^*)}{2 \tan \beta_B^*} + \eta \beta_2 \tan^2 \beta_B^*, \quad (4.20)$$

where the aspect angle is

$$\beta_B^* = \arctan \left\{ \frac{1}{12\beta_2\eta} \left[\beta_3 + \beta_1 \left(\frac{\beta_1}{\beta_3} - 1 \right) \right] \right\}, \quad (4.21)$$

and the coefficients β_i are

$$\beta_1 = \left(1 - \frac{1}{2^n} \right) \left(1 + 2^n g \frac{m_d}{F} \right), \quad (4.22)$$

$$\beta_2 = \left(\frac{1 + 2\sqrt{2}}{7} \right) \left(1 - \frac{1}{2^{3n/2}} \right) \sqrt{1 + 2^n g \frac{m_d}{F}}, \quad (4.23)$$

$$\beta_3 = \left(216\beta_1\beta_2^2\eta^2 - \beta_1^3 + 12\sqrt{324\beta_1^2\beta_2^4\eta^4 - 3\beta_1^4\beta_2^2\eta^2} \right)^{1/3}. \quad (4.24)$$

Proof. The total mass of the cables, using (4.16), (4.18) and (4.17), is given by:

4. OPTIMAL DESIGN OF SOLAR ENERGY HARVESTING BRIDGE STRUCTURES

$$\mu_s = \left(\frac{1 + \tan^2 \beta}{2 \tan \beta} \right) \left(1 - \frac{1}{2^n} \right) \left(1 + 2^n g \frac{m_d}{F} \right). \quad (4.25)$$

Similarly, making use of (4.2), the total mass of bars is:

$$\mu_b = \eta \tan^2 \beta \left(\frac{1 + 2\sqrt{2}}{7} \right) \left(1 - \frac{1}{2^{3n/2}} \right) \sqrt{1 + 2^n g \frac{m_d}{F}}. \quad (4.26)$$

Introducing constants β_1 and β_2 given in (4.22) and (4.23), the total mass is:

$$\mu_B = \mu_s + \mu_b = \beta_1 \frac{(1 + \tan^2 \beta)}{2 \tan \beta} + \eta \beta_2 \tan^2 \beta. \quad (4.27)$$

The angle β for minimal mass can be achieved from,

$$\frac{\partial \mu_B}{\partial \tan \beta} = \beta_1 \left(1 - \frac{1 - \tan^2 \beta}{2 \tan^2 \beta} \right) + 2\eta \beta_2 \tan \beta = 0, \quad (4.28)$$

yielding the optimal angle of (4.21) by solving the following cubic equation:

$$4 \frac{\beta_2}{\beta_1} \eta \tan^3 \beta + \tan^2 \beta - 1 = 0. \quad (4.29)$$

Substituting (4.21) into (4.27) concludes the proof. □

The minimal mass solution under buckling constraints depends on the material choice for the structural component (bars, cables and deck), on the external force F and span L . If the deck mass m_d is zero then the minimal mass is for complexity $n = 1$. Instead, if F_{tot} is variable with the complexity n through the deck mass m_d (as defined in Eq. 4.14), the global optimum can

4. OPTIMAL DESIGN OF SOLAR ENERGY HARVESTING BRIDGE STRUCTURES

<i>steel</i>	
ρ [kg/m^3]	7862
σ [N/m^2]	6.9×10^8
E [N/m^2]	2.06×10^{11}
<i>Spectra[®] - UHMWPE</i>	
ρ [kg/m^3]	970
σ [N/m^2]	2.7×10^9
E [N/m^2]	120×10^9

Table 4.1: Material properties.

n	p	F_{tot} [N]	β_B^* [deg]	μ_B^*	μ_{tot}^*
4	1	12201.34	6.95	5.8932	10.8179
5	1	12191.10	7.00	6.0406	10.7148
6	1	12188.45	7.03	6.1121	10.7214
7	1	12187.78	7.04	6.1469	10.7400
8	1	12187.61	7.05	6.1641	10.7530

Table 4.2: Optimal masses μ_B^* (4.20) and μ_{tot}^* (4.30) and optimal aspect angles β_B^* (4.21) of *substructure* bridges with steel bars and cables, under combined yielding and buckling constraints (B), for different complexities n .

be reached for a generic finite complexity n , as a function of the ratio between the total deck force ($2^n m_d g$) and the total external force (F).

The final total mass to be optimized is then the summation of the mass of the bridge structure (4.20), the total mass of the deck (4.13) and the mass of the joints, Ωn_n :

$$\mu_{tot}^* = \mu_B^* + \mu_d^* + \Omega n_n, \quad (4.30)$$

being Ω a factor equal to zero for perfect joints and greater than zero for crudely constructed (cheaper) joints.

4. OPTIMAL DESIGN OF SOLAR ENERGY HARVESTING BRIDGE STRUCTURES

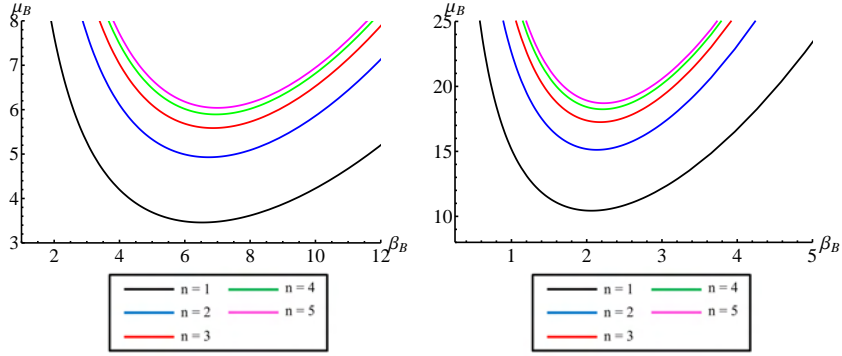


Figure 4.6: Dimensionless mass μ_B (4.27) vs. aspect angle β_B for: solution with steel bars and cables (left, $\eta = 238.65$), steel bars and Spectra cables (right, $\eta = 7569.04$).

n	p	F_{tot} [N]	β_B^* [deg]	μ_B^*	μ_{tot}^*
1	1	12019.39	2.06	10.4357	25.4791
2	1	12010.97	2.13	15.1186	23.6251
3	1	12007.50	2.18	17.2522	23.0724
4	1	12006.35	2.21	18.2414	23.1662
5	1	12006.03	2.23	18.7080	23.3822

Table 4.3: Optimal masses μ_B^* (4.20) and μ_{tot}^* (4.30) and optimal aspect angles β_B^* (4.21) of *substructure* bridges with steel bars and Spectra[®] cables, under combined yielding and buckling constraints (B), for different complexities n .

4.5 Numerical Results

4.5.1 Minimal Mass Design

In this section we show the minimal masses and the optimal angles of tensegrity bridges with several complexities n . The numerical results are presented in terms of μ_B^* and β_B^* denoting respectively the minimal masses and the optimal aspect angles under combined yielding and buckling constraints. The results are obtained numerically applying Theorem 4.4.1.

4. OPTIMAL DESIGN OF SOLAR ENERGY HARVESTING BRIDGE STRUCTURES

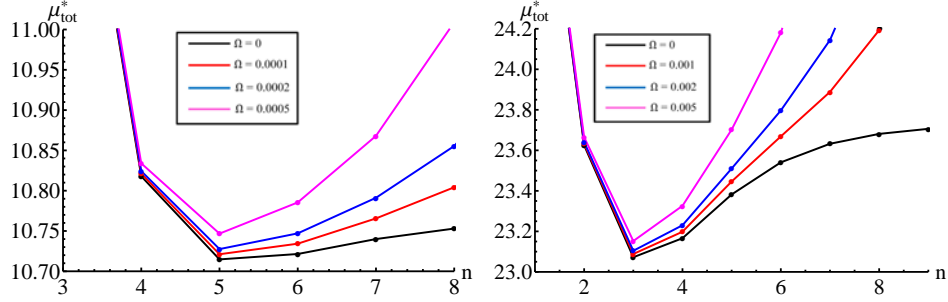


Figure 4.7: Dimensionless total mass μ_{tot}^* (4.30) vs. complexity n for: solution with steel bars and cables (left, $\eta = 238.65$), steel bars and Spectra cables (right, $\eta = 7569.04$) and different joint factors Ω .

The optimization problems are solved assuming $L = 30.48$ m, $F = 12$ kN, $w = 4.88$ m, $\alpha_d = 1$ deg and the material properties in Table 4.1. We present a first set of numerical results without joint mass in Table 4.2, in which we make use steel for bars and cables, and a second set of results in Table 4.3, in which we use steel for bars and Spectra[®] for cables. The cables placed on the deck are needed to stabilize the structure in the horizontal plane.

For each optimized structure note that, if η is close to 1, the total masses of cables, given in (4.25), is comparable to the mass total mass of the bars, given in (4.26).

The results of the first optimizations (steel bars and cables) are presented in Table 4.2 and in the left sides of Figs. 4.6 and 4.7. The optimal angles β_B^* can be obtained from (4.21) or from the left plot of the structural masses (4.27) in Fig. 4.6. We obtained optimal angles β_B^* approximately 7 deg, slightly increasing with complexity n . The structural masses μ_B^* (4.20) reported in Table 4.2 increase with n and have a minimum value for $n = 1$. Anyway, if we focus our attention on the minimization of the total masses μ_{tot}^* (4.30), we obtain a finite optimal complexity $n = 5$ ($\mu_{tot}^* \cong 10.72$), also for increasing joint mass factors Ω , as illustrated in the left plot of Fig. 4.7.

The results of the second optimizations (steel bars and Spectra[®] cables)

4. OPTIMAL DESIGN OF SOLAR ENERGY HARVESTING BRIDGE STRUCTURES

<i>cables</i>							
i	$n_{s,i}$	s_i	$A_i [m^2]$	$V_i [m^3]$	$t_i [N]$	$m_i [kg]$	μ_i
0	32	0.9525	2.6707×10^{-5}	2.5439×10^{-5}	1.8428×10^4	0.2000	0.0480
1	2	15.354	3.6244×10^{-5}	5.5651×10^{-4}	2.5009×10^4	4.3753	1.0498
2	4	7.6772	1.8122×10^{-5}	1.3913×10^{-4}	1.2504×10^4	1.0938	0.2625
3	8	3.8386	9.0611×10^{-6}	3.4782×10^{-5}	6.2521×10^3	0.2735	0.0656
4	16	1.9193	4.5305×10^{-6}	8.6955×10^{-6}	3.1261×10^3	0.0684	0.0164
5	32	0.9597	2.2653×10^{-6}	2.1739×10^{-6}	1.5630×10^3	0.0171	0.0041
<i>bars</i>							
i	$n_{b,i}$	b_i	$A_i [m^2]$	$V_i [m^3]$	$f_i [N]$	$m_i [kg]$	μ_i
1	1	1.8712	3.6321×10^{-4}	6.7965×10^{-4}	6.0955×10^3	5.3434	1.2821
2	2	0.9356	1.2841×10^{-4}	1.2015×10^{-4}	3.0478×10^3	0.9446	0.2267
3	4	0.4678	4.5401×10^{-5}	2.1239×10^{-5}	1.5239×10^3	0.1670	0.0401
4	8	0.2339	1.6052×10^{-5}	3.7546×10^{-6}	7.6194×10^2	0.0295	0.0071
5	16	0.1170	5.6751×10^{-6}	6.6372×10^{-7}	3.8097×10^2	0.0052	0.0013

Table 4.4: Properties of the members for the minimal mass design of the *sub-structure* bridge with steel bars and cables and complexity $n = 5$, ($\beta = 7.00 \text{ deg}$).

are presented in Table 4.3 and in the right sides of Figs. 4.6 and 4.7. In this case, the optimal angles β_B^* (4.21) are approximatively of 2 *deg* (see also right plot of Fig. 4.6). The minimum of the total masses μ_{tot}^* (4.30) is obtained for $n = 3$ ($\mu_{tot}^* \cong 23.15$), also for increasing factors Ω , as illustrated in the right plot of Fig. 4.7.

From the comparison of the numerical data in Table 4.2 with the data in Table 4.3, we compare steel versus Spectra[®] cables. Spectra[®] makes a more streamlined structure, with $\beta_B^* \ll 7 \text{ deg}$. It is worth noting that from steel to Spectra[®] we increasing the factor η (4.8) from 238.65 to 7569.04 and we are reducing the ratio ρ_s/σ_s from $1.14 \times 10^{-5} \text{ s}^2/\text{m}^2$ to $3.59 \times 10^{-7} \text{ s}^2/\text{m}^2$. Note that the ratio $(\rho_s/\sigma_s)^{-1}$ increases with the efficiency of a material, if one imagines that the efficiency increases with σ_s and decreases with ρ_s . Of course, the Spectra[®] design is much more efficient then steel, since the mass is ZZZ times than steel.

4. OPTIMAL DESIGN OF SOLAR ENERGY HARVESTING BRIDGE STRUCTURES

<i>cables</i>							
i	$n_{s,i}$	s_i	$A_i [m^2]$	$V_i [m^3]$	$t_i [N]$	$m_i [kg]$	μ_i
0	8	3.8100	5.4117×10^{-5}	2.0619×10^{-4}	1.4612×10^5	0.2000	1.5220
1	2	15.2510	2.9228×10^{-5}	4.4576×10^{-4}	7.8916×10^4	0.4324	3.2905
2	4	7.6255	1.4614×10^{-5}	1.1144×10^{-4}	3.9458×10^4	0.10810	0.8226
3	6	3.8128	7.3070×10^{-6}	2.7860×10^{-5}	1.9729×10^4	0.0270	0.2057
<i>bars</i>							
i	$n_{b,i}$	b_i	$A_i [m^2]$	$V_i [m^3]$	$f_i [N]$	$m_i [kg]$	μ_i
1	1	0.5801	1.1175×10^{-4}	6.4832×10^{-5}	6.0038×10^3	0.5097	3.8790
2	2	0.2901	3.9511×10^{-5}	1.1461×10^{-5}	3.0019×10^3	0.0901	0.6857
3	4	0.1450	1.3969×10^{-5}	2.0260×10^{-6}	1.5009×10^3	0.0159	0.1212

Table 4.5: Properties of the members for the minimal mass design of the *substructure* bridge with steel bars and Spectra[®]cables and complexity $n = 3$, ($\beta = 2.18$ deg).

4.6 Remarks

We present the optimal complexity of the *substructure* bridge that minimizes the sum of structural mass, deck mass and joint mass. Making better joints (less joint mass) results in higher optimal complexity and less mass. So the economic tradeoff between material cost of the truss structure and costs of making better joints will lead to the proper trade between mass and labor costs.

We define a 3D deployable tensegrity structure made of repetitive planar *substructure* bridges (spanning the canal in the transversal direction) conveniently stabilized out of plane with a set of cables, in both the transversal and the longitudinal direction of the canal. Each planar structure has a self-similar fractal type of topology generated by the complexity parameter n . The minimal mass solution yields complexity n^* which depends upon material properties. Moreover, the topology of the 3D structure is function of canal width L , aspect angle (β) of the *substructures* bridges, longitudinal aspect angle (α) governing the deploy-ability of the structure, the distance between consecutive

4. OPTIMAL DESIGN OF SOLAR ENERGY HARVESTING BRIDGE STRUCTURES

repetitive structures in the longitudinal direction (w_d).

Using steel bars, we derived an optimal design for two choices of cable material, steel and Spectra[®]. The Spectra[®] design produced an optimal structure that was much more streamlined (requiring much less volume) and much less mass, than the optimized steel design. In either material case, the design is substantially less mass than previous bridge designs. The design occupies much less volume and mass than the designs for the most advanced attempts at energy production and shading over water canals (Gujarata, India, 2012). Formulas are given which will allow economic tradeoffs between material costs of the structure, the labor cost (assuming price per joint is inversely proportional to mass of the joint) of making more refined joints, and the choice of material (steel, Spectra[®], or other). Implicit in these tradeoffs, the optimized complexity n^* of the structure is derived to allow economic decisions on the number of components (bars and cables) that will minimize mass for the given choice of material and joint costs.

5

On the Continuum Limits of Tensegrity Structures

5.1 Introduction

Over recent years, several researchers have focused their attention on the modeling of continuous media such as plates, walls, membranes, vaults and domes with "equivalent" truss and/or tensegrity structures (refer, e.g., to [86, 87, 15, 88, 89, 90, 91, 92, 93, 94, 95, 96, 97, 98], and therein references). Numerous up-to-date contributions to such a longly debated topic of structural mechanics deal with 'non-conforming' or 'mixed' finite element methods, also referred to as Lumped Stress Methods (LSMs) [87, 15, 93, 94]; the so-called Thrust Network Analysis (TNA), reciprocal force diagrams and limit analysis approaches [86, 90, 92, 91, 95, 96], as well as Discrete Exterior Calculus (DEC) [97, 98]. A common trait of the above methods consists of looking at the approximating truss structure as the support of uniaxial singular (or lumped) stresses, which approximate the stress field of the background medium. Studies regarding the convergence of a singular discrete stress network to its continuum limit have been carried out through Gamma-Convergence [88], and mixed finite element methods [99]. Particular attention has been devoted to masonry structures described through the no-tension constitutive model [100], since for such structures the singular stress approach allows one to linearize the no-tension constraint, and to make use of form-finding approaches based on convex-hull techniques and weighted Delaunay triangulations [86, 90, 91, 93, 94, 95, 96, 98]. Remarkable is the use of polyhedral Airy stress functions in 2D elasticity problems, and Pucher's approaches to the membrane theory of shells [101], which leads to an effective characterization of internally self-equilibrated frameworks associated with simply connected domains [87, 15, 99, 93, 94].

Force networks are also employed within 'atomistic' models and discrete - continuum approaches to mechanical systems, to represent the state of stress of solids, fluids and biomechanical systems. Coupled discrete-continuum approaches combine force networks and continuous stress fields (refer, e.g., to [102] for an extensive review), in order to circumvent scaling limitations of fully atomistic models, which are particularly suited to describe small pro-

cess zones (interested, e.g., by dislocation and fracture nucleation, nanoin-dentation, marked atomic rearrangements, etc.). Areas of research involving discrete models of mechanical systems include bio- and nano-structures [103, 104, 105, 106, 107, 108, 109, 110]; tensegrity models of engineering and biological systems [111, 112, 113, 27, 114]; structural optimization and form-finding methods [93, 94, 115, 116, 117, 118], and strut and tie models of discontinuous regions in reinforced-concrete structures [119], just to name a few examples. Key aspects of scale-bridging approaches to discrete systems regard the estimation of the Cauchy stress at the meso-scale, to be carried out via statistical mechanics, variational approaches, and/or homogenization methods. Several discrete (or ‘microscopic’) definitions of the Cauchy stress have been proposed in the literature, such as, e.g., the *virial stress*, the *Tsai traction* and the *Hardy stress* (cf., e.g., [120, 121], and therein references). Different studies have highlighted issues related to the kinetic terms of such stress definitions [120], and spatial fluctuations of the discrete stress (cf. Sect. 6 of [121]).

The present Chapter deals with the correspondence between polyhedral (Airy) stress functions, internally self-equilibrated tensegrity structures, and discrete notions of the Cauchy stress in two-dimensions. We extend previous research on such topics [87, 15, 99, 93, 94], on examining two new subjects: *(i)* the computation of the Airy stress function associated with a given, internally self-equilibrated framework; *(ii)* the formulation of convergent estimates of the Cauchy stress associated with unstructured force networks. Our previous studies in this field were instead focused on the derivation of force networks from a given polyhedral stress function (inverse problem with respect to *(i)*, cf. [87, 15, 93, 94]), and the convergence of stress measures associated with structured force networks [15, 99]. By examining a simply connected domain in two dimensions, we here develop and discuss an algebraic equation relating polyhedral stress functions and internally self-equilibrated frameworks associated with arbitrary triangulations. Further on, we formulate a regularization technique that is devoted to generate a convergent notion of the Cauchy stress

of the discrete system in the continuum limit.

5.2 Internally self-equilibrated tensegrity structures and polyhedral stress functions

We refer to a triangulation Π_h of a polygonal and simply-connected domain Ω of the two-dimensional Euclidean space, which shows M non-degenerate triangles $\Omega_1, \dots, \Omega_M$ and features the following size: $h = \sup_{m \in \{1, \dots, M\}} \{diam(\Omega_m)\}$. We name ‘*physical*’ the edges of Π_h that do *not* belong to the boundary of Ω .

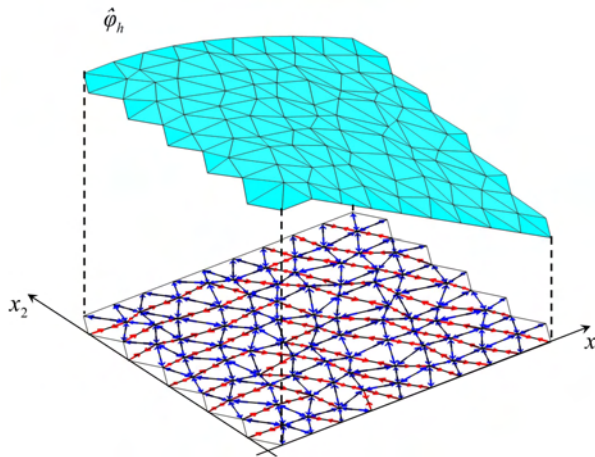


Figure 5.1: Illustration of a triangulated force network and the associated polyhedral stress function $\hat{\varphi}_h$ (red: tensile forces, blue: compressive forces).

5.2.1 Internally self-equilibrated framework associated with a given polyhedral stress function

Let us introduce Cartesian coordinates x_1 and x_2 in the plane of Ω and the polyhedral function defined as follows

$$\hat{\varphi}_h(\mathbf{x}) = \sum_{n=1}^N \hat{\varphi}_n g_n(\mathbf{x}) \quad (5.1)$$

where $\mathbf{x} = [x_1, x_2]^T$; N is the total number of nodes of the triangulation Π_h ; $\hat{\varphi}_n$ is the value taken by $\hat{\varphi}_h$ at the node \mathbf{x}_n ; and g_n is the piecewise linear basis function associated with such a node ('umbrella' basis function). We agree to denote the coordination number of \mathbf{x}_n by \mathcal{S}_n , and the edges attached to such a node by $\Gamma_n^1, \dots, \Gamma_n^{\mathcal{S}_n}$. The unit vectors perpendicular and tangent to $\Gamma_n^1, \dots, \Gamma_n^{\mathcal{S}_n}$ will be hereafter indicated by $\hat{\mathbf{h}}_n^1, \dots, \hat{\mathbf{h}}_n^{\mathcal{S}_n}$, and $\hat{\mathbf{k}}_n^1, \dots, \hat{\mathbf{k}}_n^{\mathcal{S}_n}$, respectively (Fig. 5.2). By interpreting $\hat{\varphi}_h$ as a *generalized (Airy) stress function*, we associate a set of N_Γ forces with such a function, where N_Γ indicates the total number of physical edges of Π_h . The generic of such forces is given by

$$P_n^s = \left[\left[\nabla \hat{\varphi}_h \cdot \hat{\mathbf{h}}_n^s \right]_n \right]^s \quad (5.2)$$

where $\left[\left[\nabla \hat{\varphi}_h \right]_n \right]^s$ indicates the jump of the gradient of $\hat{\varphi}_h$ across the edge Γ_n^s [15, 99]. The gradient $\nabla \hat{\varphi}_h$ is computed as follows over the generic triangle $\mathbf{x}_n, \mathbf{x}_n^s, \mathbf{x}_n^t$ (refer, e.g., to [122])

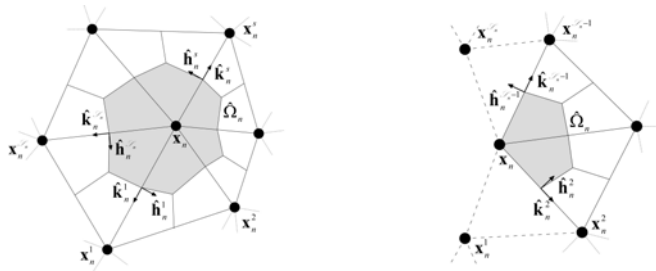


Figure 5.2: Details of an inner node (left) and a boundary node (right) of Π_h .

$$\nabla \hat{\varphi}_h = \frac{1}{2A} \begin{bmatrix} \{\hat{\varphi}_n(\mathbf{x}_n^s - \mathbf{x}_n^t) + \hat{\varphi}_n^s(\mathbf{x}_n^t - \mathbf{x}_n) + \hat{\varphi}_n^t(\mathbf{x}_n - \mathbf{x}_n^s)\} \cdot \hat{\mathbf{e}}_2 \\ \{\hat{\varphi}_n(\mathbf{x}_n^t - \mathbf{x}_n^s) + \hat{\varphi}_n^s(\mathbf{x}_n - \mathbf{x}_n^t) + \hat{\varphi}_n^t(\mathbf{x}_n^s - \mathbf{x}_n)\} \cdot \hat{\mathbf{e}}_1 \end{bmatrix} \quad (5.3)$$

where A is the area of the above triangle, and $\hat{\mathbf{e}}_\alpha$ is the unit vector in the direction of the x_α -axis. Equation (5.2) shows that the forces P_n^s are associated with the ‘folds’ of the graph of $\hat{\varphi}_h$. In particular, *convex folds* of $\hat{\varphi}_h$ correspond with *tensile forces*, while *concave folds* correspond with *compressive forces* (Fig. 5.1). It is useful to recast (5.2) in matrix form, by proceeding as follows. Let us sort the $\mathbf{x}_n^1, \dots, \mathbf{x}_n^{\mathcal{S}_n}$ nodes connected to \mathbf{x}_n in counterclockwise order, as shown in Fig. 5.2, and denote the values taken by $\hat{\varphi}_h$ at such nodes by $\hat{\varphi}_n^1, \dots, \hat{\varphi}_n^{\mathcal{S}_n}$, respectively. Said $\mathcal{P}_n \leq \mathcal{S}_n$ the number of physical edges attached to \mathbf{x}_n , we collect the forces associated with such a node into the \mathcal{P}_n -dimensional vector $\hat{\mathbf{P}}_n = [P_n^1, \dots, P_n^{\mathcal{P}_n}]^T$, and the values of $\hat{\varphi}$ at $\mathbf{x}_n^1, \dots, \mathbf{x}_n^{\mathcal{S}_n}$ and \mathbf{x}_n into the $(\mathcal{S}'_n = \mathcal{S}_n + 1)$ -dimensional vector $\hat{\boldsymbol{\varphi}}_n = [\hat{\varphi}_n^1, \dots, \hat{\varphi}_n^{\mathcal{S}_n}, \hat{\varphi}_n]^T$. Straightforward calculations show that the substitution of (5.3) into (5.2) leads to the following algebraic equation

$$\hat{\mathbf{P}}_n = \hat{\mathbf{C}}_n \hat{\boldsymbol{\varphi}}_n \quad (5.4)$$

where $\hat{\mathbf{C}}_n$ is the $\mathcal{P}_n \times \mathcal{S}'_n$ matrix defined through

$$(C_n)_{jk} = \begin{cases} a = \hat{\mathbf{h}}_n^{j'''} \cdot \hat{\mathbf{h}}_n^{j'} / (\ell_n^{j'} (\hat{\mathbf{h}}_n^{j'''} \cdot \hat{\mathbf{k}}_n^{j'})) \\ \quad - \hat{\mathbf{h}}_n^{j''} \cdot \hat{\mathbf{h}}_n^{j'} / (\ell_n^{j'} (\hat{\mathbf{h}}_n^{j''} \cdot \hat{\mathbf{k}}_n^{j'})), & k = j', \\ b = -\hat{\mathbf{h}}_n^{j'} \cdot \hat{\mathbf{h}}_n^{j'} / (\ell_n^{j''} (\hat{\mathbf{h}}_n^{j'} \cdot \hat{\mathbf{k}}_n^{j''})), & k = j'', \\ c = \hat{\mathbf{h}}_n^{j'} \cdot \hat{\mathbf{h}}_n^{j'} / (\ell_n^{j'''} (\hat{\mathbf{h}}_n^{j'} \cdot \hat{\mathbf{k}}_n^{j'''})), & k = j''', \\ d = -a - b - c, & k = \mathcal{S}'_n, \\ 0, & \text{otherwise,} \end{cases} \quad (5.5)$$

In (5.5), ℓ_n^s denotes the length of Γ_n^s , and it results

$$\begin{array}{ll} \textit{inner node} & \textit{boundary node} \\ j' = j & j' = j + 1 \\ \text{if } j' > 1 \text{ then } j'' = j' - 1, \text{ else } j'' = \mathcal{S}_n & j'' = j' - 1 \\ \text{if } j' < \mathcal{S}_n \text{ then } j''' = j' + 1, \text{ else } j''' = 1 & j''' = j' + 1 \end{array} \quad (5.6)$$

By using standard matrix assembling techniques, we finally obtain the following ‘global’ equation

$$\hat{\mathbf{P}}_h = \hat{\mathbf{C}}_h \hat{\varphi}_h \quad (5.7)$$

which relates the vector $\hat{\mathbf{P}}_h$ collecting all the forces P_n^s to the vector $\hat{\varphi}_h$ collecting all the nodal values of φ_h . In (5.7), $\hat{\mathbf{C}}_h$ is the $N_\Gamma \times N$ matrix obtained by assembling the nodal matrices (5.5). It can be shown [98] that the forces $\hat{\mathbf{P}}_h$ computed through (5.7) automatically satisfy the equilibrium equations of the internal nodes of Π_h with zero external forces, for any given $\hat{\varphi}_h \in \mathbb{R}^N$. This

implies that $\hat{\mathbf{P}}_h$ and the graph structure associated with Π_h form an *internally self-equilibrated framework* [123, 92].

5.2.2 Polyhedral stress function associated with a given, internally self-equilibrated framework

We now pass to examine the problem of finding a polyhedral stress function $\hat{\varphi}_h$ associated with a given, internally self-equilibrated framework $\hat{\mathbf{P}}_h$ in two-dimensions. The latter may arise e.g. from pair-interactions in a particle system [121], or a lumped stress/tensegrity approach to the equilibrium problem of a continuous medium [15, 27]. As anticipated, we assume that $\hat{\mathbf{P}}_h$ is associated with the (physical) edges of a planar (non-degenerate) triangulation Π_h of simply-connected domain Ω . It is clear that the current problem is related to the inversion of the linear system of algebraic equations (5.7). Let us refer to the illustrative example represented in Fig. 5.3, which shows a triangulated force network with a total of $N = 115$ nodes; 77 inner nodes; and 266 physical edges. We have observed in the previous section that the forces $\hat{\mathbf{P}}_h$ computed through (5.7) satisfy the equilibrium equations of the inner nodes of Π_h (with zero applied forces), for any given $\hat{\varphi}_h \in \mathbb{R}^N$. This proves that the rank of $\hat{\mathbf{C}}_h$ is equal to 112 ($r = \text{rank}(\hat{\mathbf{C}}_h) = 266 - 2 \times 77 = 112$), and that the nullity of the same matrix is equal to 3 ($n = \text{nullity}(\hat{\mathbf{C}}_h) = 115 - 112 = 3$, cf., e.g., [124]), in the case under examination. Given an arbitrary internally self-equilibrated force network $\hat{\mathbf{P}}_h \in \mathbb{R}^r$, we therefore conclude the following: (i) the linear system (5.7) actually admits solutions $\hat{\varphi}_h \in \mathbb{R}^N$; (ii) such solutions are determined up to three arbitrary constants; (iii) two solutions differ by linear functions associated with zero axial forces along the edges of Π_h . It is not difficult to realize that the above results (i), (ii) and (iii), which generalize analogous ones concerned with smooth Airy functions [125], can be extended to arbitrary triangulations of simply-connected domains. Consider, e.g., that the insertion of an additional (inner) node into the triangulation in Fig. 5.3 leads to a new triangulation carrying 116 nodes; 269 forces: and $2 \times 28 = 156$ equilibrium constraints ($\text{rank}(\hat{\mathbf{C}}_h) = 269 - 156 = 113$). It is easily shown that

such an insertion leaves the nullity of $\hat{\mathbf{C}}_h$ equal to 3. The indeterminacy of system (5.7) can be resolved by prescribing $\hat{\varphi}_h$ at three non-collinear nodes of Π_h (e.g., prescribing the values of $\hat{\varphi}_h$ at the vertices of a given triangle). A particular solution of (5.7) is given by

$$\hat{\varphi}_h = \hat{\mathbf{C}}_h^+ \hat{\mathbf{P}}_h \quad (5.8)$$

where $\hat{\mathbf{C}}_h^+$ denotes the Moore-Penrose inverse of $\hat{\mathbf{C}}_h$. We address the special case of a multiple-connected domain to the Appendix.

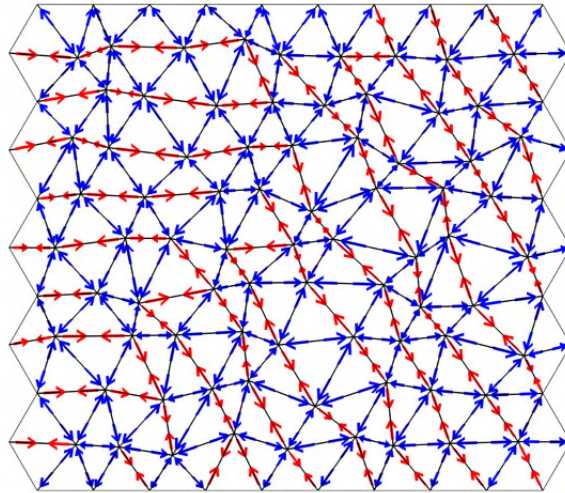


Figure 5.3: 2D view of the force network in Fig. 5.1 (red: tensile forces, blue: compressive forces).

5.3 Stress field associated with a tensegrity structure

It is not difficult to realize that a scale bridging approach to the stress field associated with a self-equilibrated force network $\hat{\mathbf{P}}_h$ describing a tensegrity structure can be obtained by introducing a suitable regularization of the corresponding stress function $\hat{\varphi}_h$. Consider, indeed, that the stress field associated with a smooth Airy stress function φ_0 corresponds with the hessian of φ_0 (under a suitable rotation transformation, see, e.g., [126, 125]), i.e. the second-order tensor with Cartesian components $\partial^2\varphi_0/\partial x_\alpha\partial x_\beta$ ($\alpha, \beta = 1, 2$). Since the second-order derivatives of a polyhedral function $\hat{\varphi}_h$ exist only in the distributional sense, the definition of a stress field associated with $\hat{\varphi}_h$ calls for the introduction of a generalized notion of the hessian of such a function [88, 99]. A convergent stress measure has been defined in [99], on considering sequences of polyhedral stress functions associated with structured triangulations. The latter match the \mathcal{P}_Σ property defined in Sect. 5 of [99], and consist, e.g., of triangulations associated with rectangular or hexagonal Bravais lattices (cf. Figs. 2 and 3 of [99]). Let us define a 'dual mesh' $\hat{\Pi}_h$ of Ω , which is formed by polygons connecting the barycenters of the triangles attached to the generic node \mathbf{x}_n to the mid-points of the edges $\Gamma_n^1, \dots, \Gamma_n^{S_n}$ ('barycentric' dual mesh, cf. Fig. 5.1). The stress measure defined in [99] is a piecewise constant stress field $\hat{\mathbf{T}}_h$ over $\hat{\Pi}_h$, which takes the following value in correspondence with the generic dual cell $\hat{\Omega}_n$

$$\hat{\mathbf{T}}_h(n) = \frac{1}{|\hat{\Omega}_n|} \sum_{j=1}^{\mathcal{P}_n} \frac{\ell_n^{j'}}{2} P_n^{j'} \hat{\mathbf{k}}_n^{j'} \otimes \hat{\mathbf{k}}_n^{j'} \quad (5.9)$$

Here, $|\hat{\Omega}_n|$ denotes the area of $\hat{\Omega}_n$, and j' is defined as in (5.6). Under the assumption that Π_h is a structured triangulation, it has been shown in [99] that the discrete stress (5.9) strongly converges to the stress field associated

with the limiting stress function, as the mesh size approaches zero (cf. Lemma 2 of [99]). It is worth observing that $\hat{\mathbf{T}}_h(n)$ is obtained by looking at the quantity $P_n^s \hat{\mathbf{k}}_n^s \otimes \hat{\mathbf{k}}_n^s$ as a ‘lumped stress tensor’ acting in correspondence with the edge Γ_n^s , and that Eqn. (5.9) spatially averages the lumped stress tensors competing to \mathbf{x}_n , over the corresponding dual cell $\hat{\Omega}_n$ (averaging domain). We also note that the stress measure (5.9) corresponds with the virial stress of statistical mechanics at zero temperature (cf. [121], Sect. 2.2 and Appendix A). Unfortunately, the error estimate given in Lemma 2 of [99] does not cover unstructured triangulations, as we already noticed. We hereafter handle the case of an unstructured polyhedral stress function $\hat{\varphi}_h$ by employing the regularization procedure formulated in [127] to predict the curvatures of polyhedral surfaces. Let us consider an arbitrary vertex \mathbf{x}_n of $\hat{\varphi}_h$, and a given set K_n of selected neighbors of \mathbf{x}_n (such as, e.g., the nearest neighbors, second nearest neighbors, etc., cf. Fig. 5.4). We first construct a smooth fitting function $\hat{\Phi}_{K_n}(\mathbf{x})$ of the values taken by $\hat{\varphi}_h$ at the node set K_n . Next, we evaluate $\hat{\Phi}_{K_n}(\mathbf{x})$ at the vertices $\tilde{\mathbf{x}}_1, \dots, \tilde{\mathbf{x}}_{\tilde{N}}$ of a second, structured triangulation $\tilde{\Pi}_h$, which is built up around \mathbf{x}_n (Fig. 5.4). We finally construct the following ‘regularized’ polyhedral stress function

$$\tilde{\varphi}_h = \sum_{n=1}^{\tilde{N}} \hat{\Phi}_{K_n}(\tilde{\mathbf{x}}_n) \tilde{g}_n \quad (5.10)$$

where \tilde{N} is the number of nodes of $\tilde{\Pi}_h$, and \tilde{g}_n denotes the piecewise linear basis function associated with $\tilde{\mathbf{x}}_n \in \tilde{\Pi}_h$. Useful fitting models are offered by interpolation polynomials, local maximum entropy shape function, Moving Least Squares (MLS) meshfree approximations, and B-Splines, just to name a few examples (refer, e.g., to [128] for a comparative study of such methods). Let us focus now on Eqns. (5.2) and (5.9). The replacements of all the quantities relative to Π_h with the analogous ones referred to $\tilde{\Pi}_h$ in such equations, leads us to (structured) ‘regularizations’ $\tilde{\mathbf{P}}_h$ and $\tilde{\mathbf{T}}_h$ of the force network and

stress field associated with the unstructured mesh Π_h , respectively.

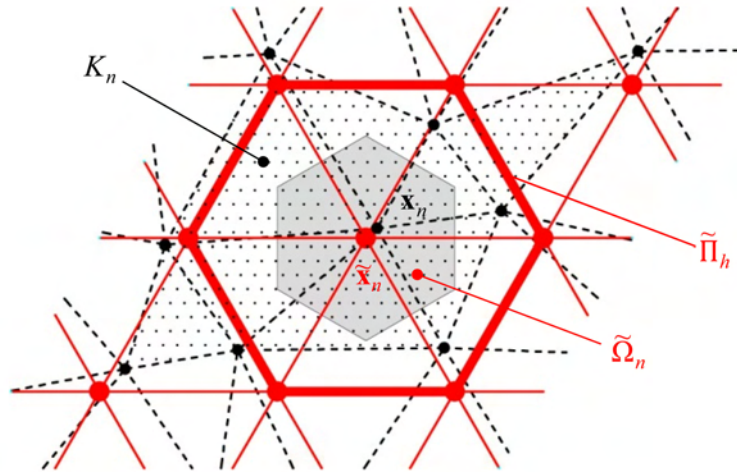


Figure 5.4: Illustration of K_n and $\tilde{\Omega}_n$.

5.4 Numerical results

The present section provides a collection of numerical applications of the procedures described in the sections 5.2 and 5.3. We deal with the Flamant solution to the stress field of a half-plane loaded by a normal force, and tensegrity models of a cantilever beam and an elliptical dome. In all the given examples, we analyze both structured and unstructured force networks describing the problem under examination, and study the properties of the associated stress fields. Given a source triangulation Π_s , and a polyhedral function $\hat{\varphi}_h$ associated with Π_s , we name *smooth projection* of $\hat{\varphi}_h$ over a target triangulation Π_t the polyhedral function defined through: (i) the construction a smoothing of $\hat{\varphi}_h$ through local quintic polynomials around each node of Π_s [129]; (ii) the sampling the fitting function $\hat{\Phi}$ at the vertices of Π_t . We assume that the fitting patch K_n associated with such a projection coincides with the entire source mesh Π_s (cf. Sect. 5.3).

5.4.1 Convergence Study

Let us study the convergence behavior of the regularized stress measure introduced in Sect. 5.3 by considering the well known Flamant solution for the problem of a half plane loaded by a perpendicular point load. Such a problem has been analyzed in [15] through a lumped stress approach based on structured meshes. We examine the Flamant solution in terms of the Airy stress function, which reads

$$\varphi_0 = -\frac{F}{\pi} r \theta \sin\theta \quad (5.11)$$

where r and θ are polar coordinates with origin at the point of application of the load F (cf., e.g., [15]). The above stress function generates the following radial stress distribution in the loaded half-plane (Fig. 5.5).

$$T_{rr}^{(0)} = -\frac{2 F \cos\theta}{\pi r} \quad (5.12)$$

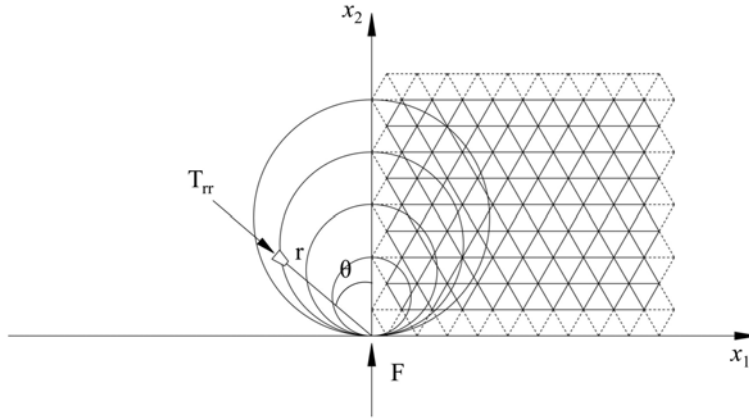


Figure 5.5: Flamant solution for for the problem of a half plane loaded by a perpendicular point load (left), and examined simulation region (right).

We consider approximations to φ_0 associated with four structured and unstructured triangulations of a 1.6×1.4 rectangular domain placed on one side of the loading axis (‘simulation region’, cf. Fig. 5.5). The analyzed structured triangulations $\tilde{\Pi}^{(1)}, \dots, \tilde{\Pi}^{(4)}$ are supported by hexagonal Bravais lattices, and show equilateral triangles with the following edge lengths: $\tilde{h}_1 = 0.20$ (mesh # 1); $\tilde{h}_2 = 0.10$ (mesh # 2); $\tilde{h}_3 = 0.05$ (mesh # 3); and $\tilde{h}_4 = 0.025$ (mesh # 4), respectively. The unstructured triangulations $\Pi^{(1)}, \dots, \Pi^{(4)}$ are instead obtained through random perturbations of the positions of the nodes of $\tilde{\Pi}^{(1)}, \dots, \tilde{\Pi}^{(4)}$.

We first examine the projections $\hat{\varphi}^{(1)}, \dots, \hat{\varphi}^{(4)}$ of the Flamant solution (5.11) over the unstructured meshes $\Pi^{(1)}, \dots, \Pi^{(4)}$. Each of such stress functions generates an unstructured force network $\hat{\mathbf{P}}^{(i)}$ (cf. Sect. 5.2), and a piecewise constant approximation $\hat{T}_{rr}^{(i)}$ to the Flamant stress field (Sect. 5.3). Next, we construct a smooth projection $\tilde{\varphi}^{(i)}$ of the generic $\hat{\varphi}^{(i)}$ over the structured trian-

gulation $\tilde{\Pi}^{(i)}$ (*unstructured to structured regularization*). We let $\tilde{\mathbf{P}}^{(i)}$ and $\tilde{T}_{rr}^{(i)}$ respectively denote the force network and the discrete stress field associated with such a ‘regularized’ stress function.

The accuracy of each examined approximation to the radial stress field (5.12) is measured through the following Root Mean Square Deviation

$$\text{err}(T_{rr}^{(i)}) = \sqrt{\left(\sum_{n=1}^N \left((T_{rr}^{(i)})_n - (T_{rr}^{(0)})_n\right)^2\right) / N} \quad (5.13)$$

where N denotes the total number of nodes of the current mesh; $(T_{rr}^{(i)})_n$ denotes the value at node n of $T_{rr}^{(i)}$; and $(T_{rr}^{(0)})_n$ denotes the value at the same node of the exact stress field (5.12). In (5.13), we let $T_{rr}^{(i)}$ denote either $\hat{T}_{rr}^{(i)}$ (unstructured approximation to $T_{rr}^{(0)}$), or $\tilde{T}_{rr}^{(i)}$ (structured approximation to $T_{rr}^{(0)}$).

Fig. 5.6 graphically illustrates the force networks $\hat{\mathbf{P}}^{(i)}$ and $\tilde{\mathbf{P}}^{(i)}$ computed for some selected meshes, while Fig. 5.7 plots the approximation error (5.13) against the mesh size \tilde{h} , for each of the analyzed approximation schemes. Finally, Fig. 5.8 depicts 3D density plots of $\hat{T}_{rr}^{(i)}$ and $\tilde{T}_{rr}^{(i)}$ for meshes #3 and #4. As the mesh size \tilde{h} approaches zero, we observe from Fig. 5.7 that the approximation errors of the unstructured approximations to $T_{rr}^{(0)}$ show rather low reduction rate, while those of the structured approximations instead feature slightly super-linear convergence to zero. The results shown in Fig. 5.8 confirm the higher degree of accuracy of the structured approximations $\tilde{T}_{rr}^{(i)}$, as compared to the unstructured approximations $\hat{T}_{rr}^{(i)}$. In this figure, we marked selected contour lines of the exact radial stress $T_{rr}^{(0)}$ by white circles (cf. Fig. 5.5).

5.4.2 Cantilever Tensegrity Structure

The current example is aimed to show how the procedures presented in Sects. 5.2 and 5.3 can be applied to determine the Airy stress function and the stress field associated with two different tensegrity models of a cantilever beam. We examine a truss structure $\tilde{\Pi}$ that has the same topology as the minimum

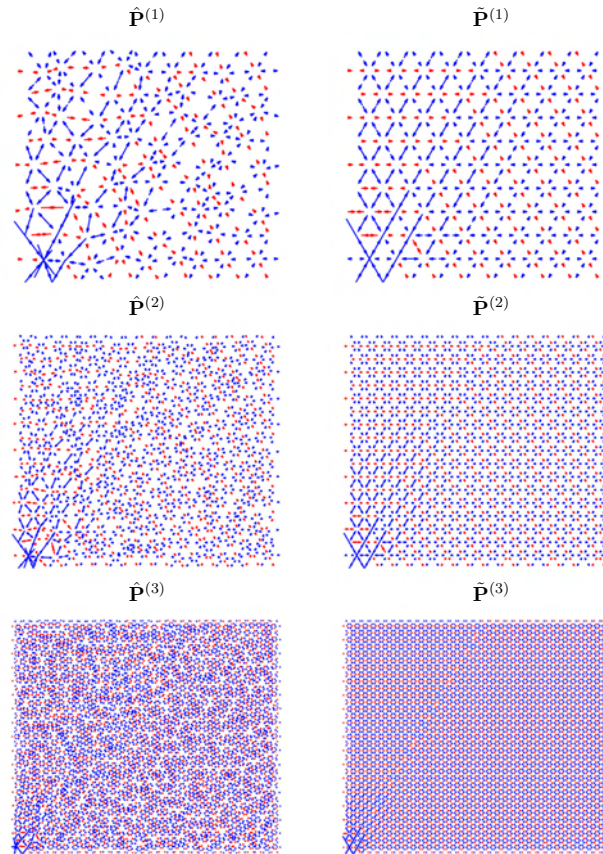


Figure 5.6: Illustrations of selected unstructured (left) and structured (right) force networks approximating the Flamant problem in Fig. 5.5 (blue: compressive forces; red: tensile forces).

volume frames analyzed in a famous study by A.G.M. Michell [20] (see also [27], Chap. 4). Such a truss is composed of a system of orthogonal and equiangular spirals, which carries a force F at a given point A , and is rigidly anchored in correspondence with a small circle centered at the origin B of the spirals (refer to Fig. 5.9, and [20, 27, 131]). We assume that the length of the AB segment is 10; the opening angle of the truss is π ; the radius of the anchoring circle is 2; and it results $F = 10$ (in abstract units). We complete the Michell truss with the insertion of diagonal edges connecting the two orders of spirals, obtaining an enriched truss model supported by a triangulation with

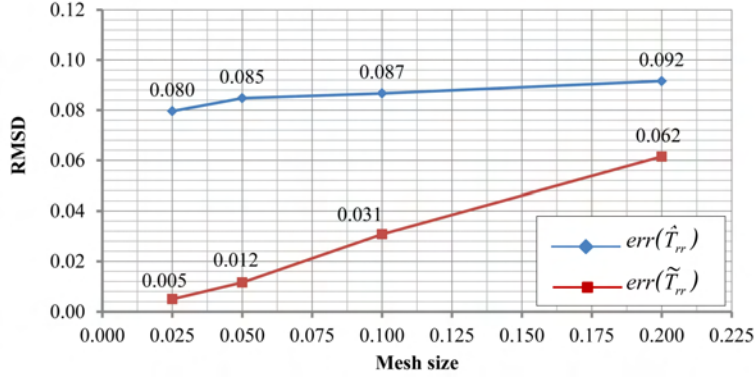


Figure 5.7: Root Mean Square Deviations of the examined approximations to the radial stress $T_{rr}^{(0)}$ of the Flamant problem.

589 nodes and 1578 physical edges (cf. Fig. 5.9). We also consider a perturbed configuration Π of the Michell truss, which is obtained by randomly moving the inner nodes of the regular configuration (Fig. 5.9).

We initially follow Michell’s approach to the equilibrium problem of $\tilde{\Pi}$, by computing the axial forces in the spiral members through the nodal equilibrium equations of the structure (refer to [27], Chap. 4), and setting the forces in the remaining edges to zero (‘Michell truss’). Next, we associate an Airy stress function $\tilde{\varphi}$ to such a force network $\tilde{\mathbf{P}}$, through Eqn. (5.8) of Sect. 5.2.2 (cf. Fig. 5.9). On proceeding in reverse order with respect to the previous example, we then construct a smooth projection $\hat{\varphi}$ of $\tilde{\varphi}$ over the perturbed configuration Π , and let $\hat{\mathbf{P}}$ denote the associated force network (Fig. 5.9). Let us focus our attention on the Cartesian components T_{11} and T_{12} of the stress fields associated with $\tilde{\mathbf{P}}$ and $\hat{\mathbf{P}}$ (x_1 denoting the longitudinal axis). The results in Fig. 5.10 highlight that the ‘structured stress’ $\tilde{\mathbf{T}}$ (associated with $\tilde{\mathbf{P}}$) smoothly describes the stress field associated with the background domain of the Michell truss, while the ‘unstructured stress’ $\hat{\mathbf{T}}$ (associated with $\hat{\mathbf{P}}$), on the contrary, provides a fuzzy description of such a stress field.

A different approach to the truss $\tilde{\Pi}$ is obtained by looking at the 2D elastic problem of the background domain Ω (here supposed to be homogeneous),

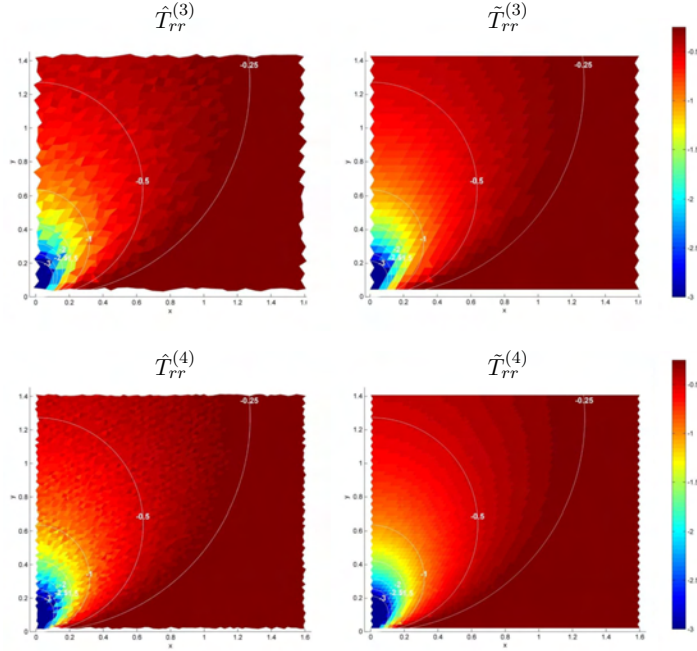


Figure 5.8: Density plots of the examined approximations to the radial stress $T_{rr}^{(0)}$ of the Flamant problem for different meshes and interpolation schemes.

under the given boundary conditions. We now interpret $\tilde{\Pi}$ as a lumped stress model of Ω , i.e., a non-conventional elastic truss having the strain energy computed per nodes (i.e., per dual elements) and not per elements (‘LSM truss’, cf. [15]). Accordingly, we determine the forces in its members by solving the elastic problem presented in Sect. 5 of [15]. As in the previous case, we also consider the smooth projection of the Airy function associated with the regular truss $\tilde{\Pi}$ over the perturbed configuration Π . We show in Fig. 5.11 the force networks and the stress fields corresponding to the LSM trusses $\tilde{\Pi}$ (Fig. 5.11, left), and Π (Fig. 5.11, right). By comparing the results in Figs. 5.9 and 5.10 with those in Fig. 5.11, we realize that the LSM truss $\tilde{\Pi}$ shows non-zero forces in the non-spiral members, differently from the Michell truss (Fig. 5.9, left). The results in Figs. 5.10 and 5.11 point out that averaging

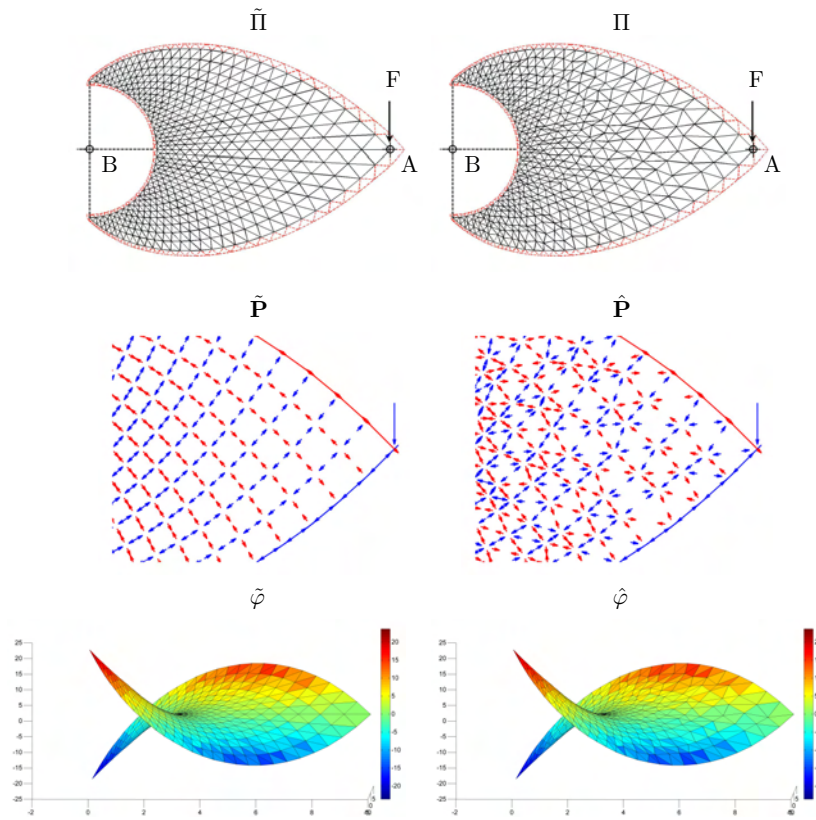


Figure 5.9: Michell truss example. Top: ordered (right) and unstructured (left) configurations. Center: details of the force networks near the tip (blue: compressive forces; red: tensile forces). Bottom: Airy stress functions associated with ordered (left) and unstructured (right) force networks.

techniques based on unstructured force networks do not generally produce smooth descriptions of the Cauchy stress field, as we already observed in Sect. 5.3.

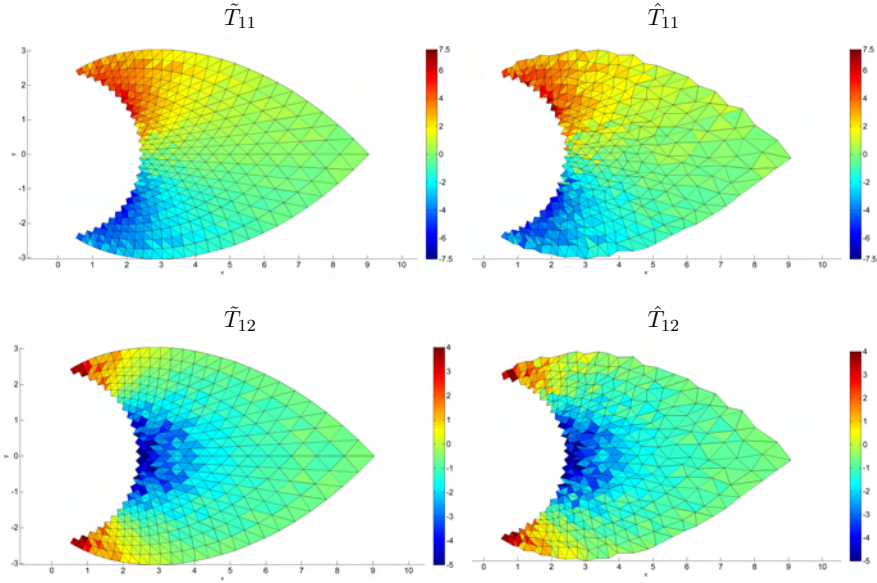


Figure 5.10: Density plots of different approximations to the stress components T_{11} (top:longitudinal normal stresses) and T_{12} (bottom:tangential stresses) associated with the Michell truss.

5.4.3 Tensegrity bridges

Let us now apply the Airy stress function approach to predict the stress field associated with a particular topology of the *nominal* tensegrity bridge illustrated in Fig. 2.3. As in the case of the structure analyzed in Sect. 5.4.2, we complete the tensegrity topology by adding a number of edges that allow us to fully triangulate the design domain covered by the bridge. We load the deck with the forces defined in Eq. (2.93), and we prescribe the aspect angles of *superstructure* and *substructure* to 30 deg.

We analyze the bridge model corresponding to the complexity $(n, p, q) = (3, 3, 3)$ (featuring 51 nodes and 134 edges, cf. Figs. 5.12, 5.13), and the model corresponding to the complexity $(n, p, q) = (5, 5, 5)$ (343 nodes and 998 edges, cf. Figs. 5.14, 5.15). It is worth noting that the analyzed bridge structure

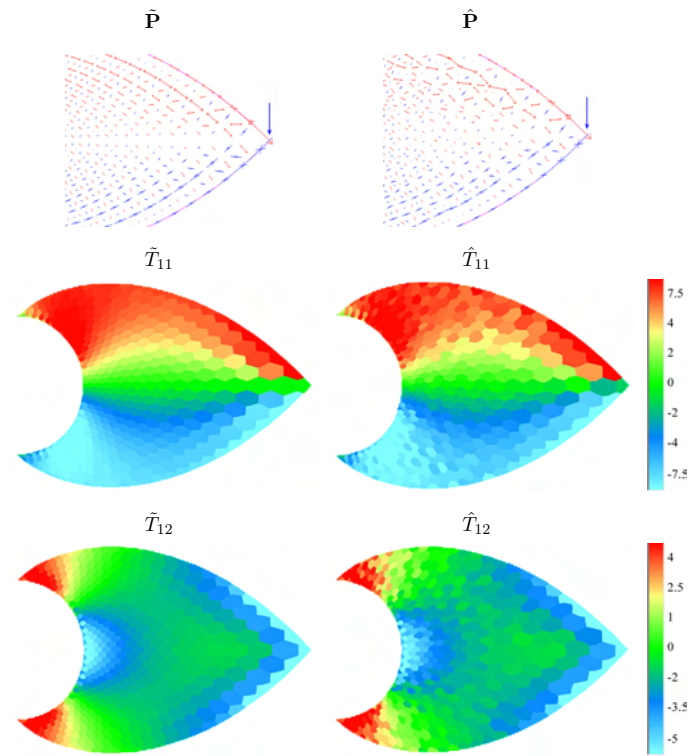


Figure 5.11: LSM truss example. Top: ordered (left) and unstructured (right) force networks (blue: compressive forces; red: tensile forces). Center and bottom: ordered and unstructured approximations to the stress field of the background domain.

tends to completely fill the design domain, i.e. converging to a continuum medium, as the complexity parameters n , p and q tend to infinity.

The plots of the deformed shapes, force networks and Cartesian stress components T_{11} , T_{22} and T_{12} associated with analyzed bridge structures are shown in Figs. 5.12, 5.13, 5.14 and 5.15. Such results graphically illustrate the discrete-to-continuum process that descends by increasing the complexity of the analyzed bridge topology. The force networks supported by the structure and the density plots of the Cartesian stress component T_{11} shown in Figs. 5.12(c), 5.13(a), 5.14(c) and 5.15(a) graphically illustrate the arch resistant

mechanisms diffusely discussed in Chap. 2. In particular, the force networks in Figs. 5.12(c) and 5.14(c), as well as the density plots of the longitudinal stresses T_{11} illustrated in Figs. 5.13(a) and 5.15(a) highlight the presence of compressed arches at the boundary of the *superstructure*, and tensile arches at the boundary of the *substructure*. The density plots of the shear stresses T_{12} show that such stress components grow in magnitude by moving towards the extremities of the bridge, as it was to be expected (cf. Figs. 5.13(c) and 5.15(b)). Finally, the density plots of the transverse stresses T_{22} show that such stress components change sign by moving from the superstructure to the substructure (cf. Fig. 5.13(b)).

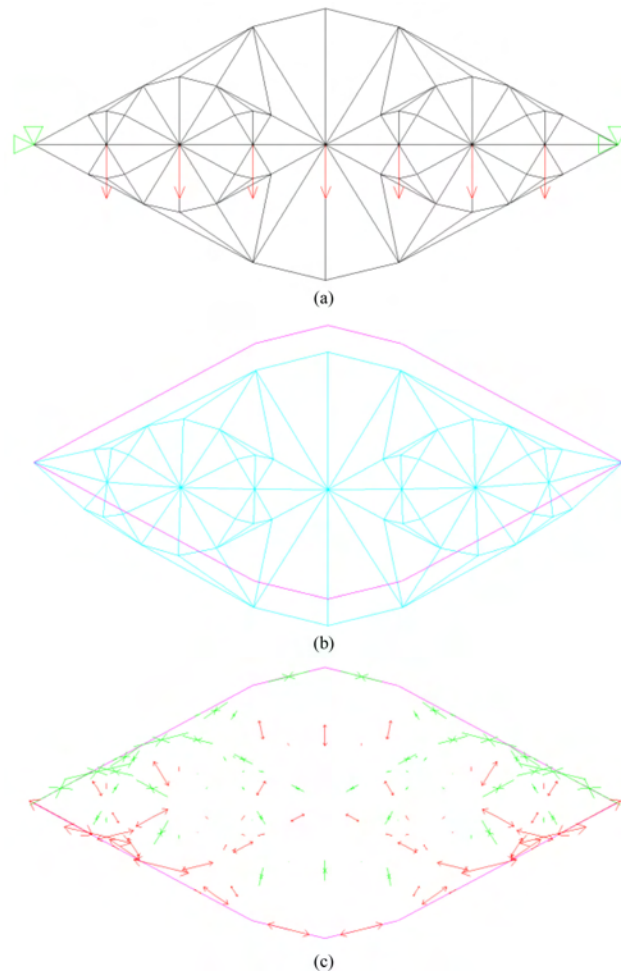


Figure 5.12: LSM bridge with complexities $n = p = q = 3$: (a) structural scheme, (b) deformed shape, (c) force network.

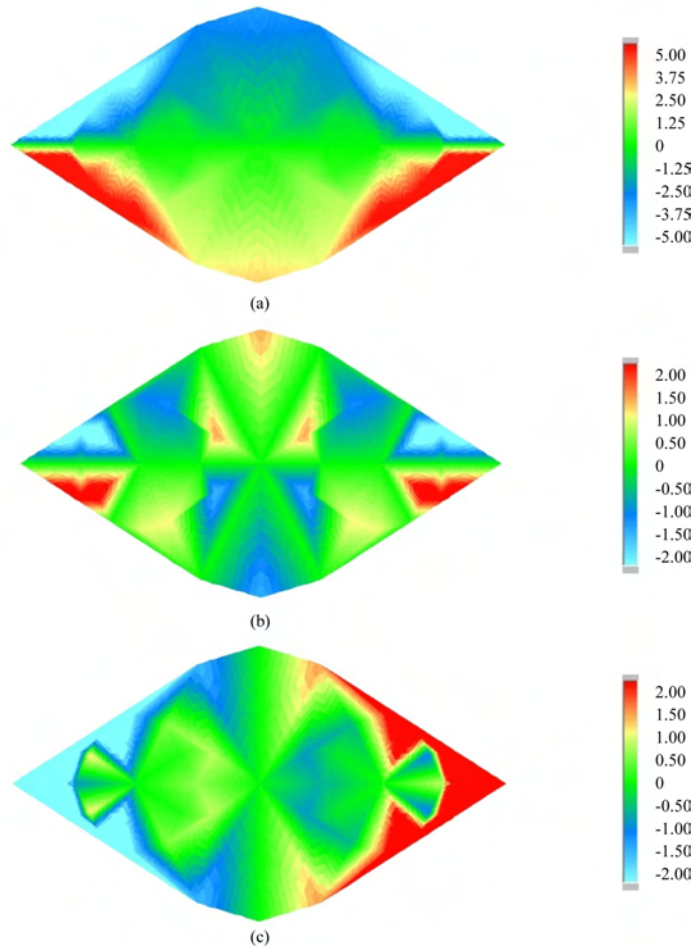


Figure 5.13: LSM bridge with complexities $n = p = q = 3$: (a) T_{11} stresses, (b) T_{22} stresses, (c) T_{12} stresses.

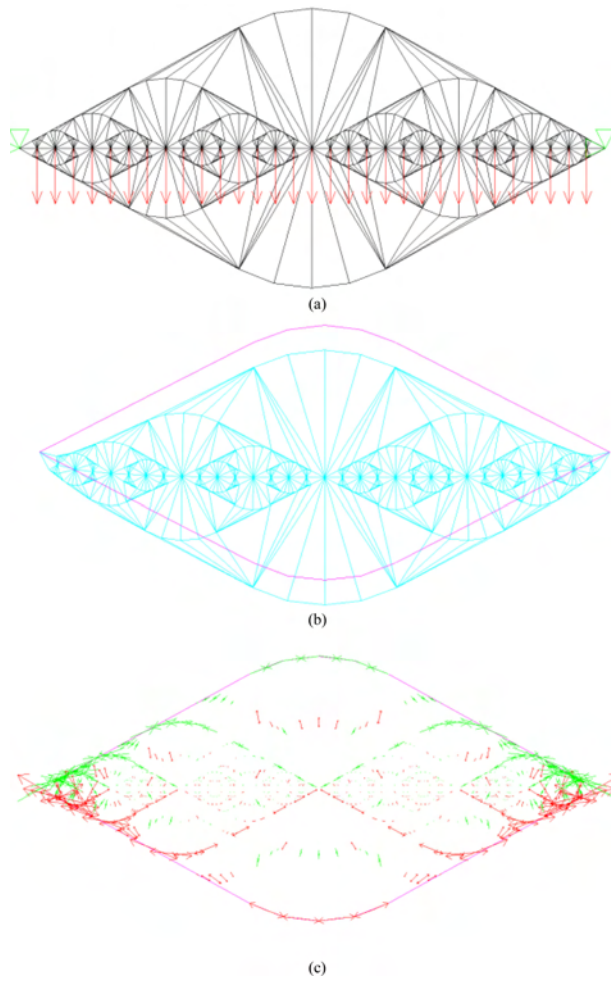


Figure 5.14: LSM bridge with complexities $n = p = q = 5$: (a) structural scheme, (b) deformed shape, (c) force network.

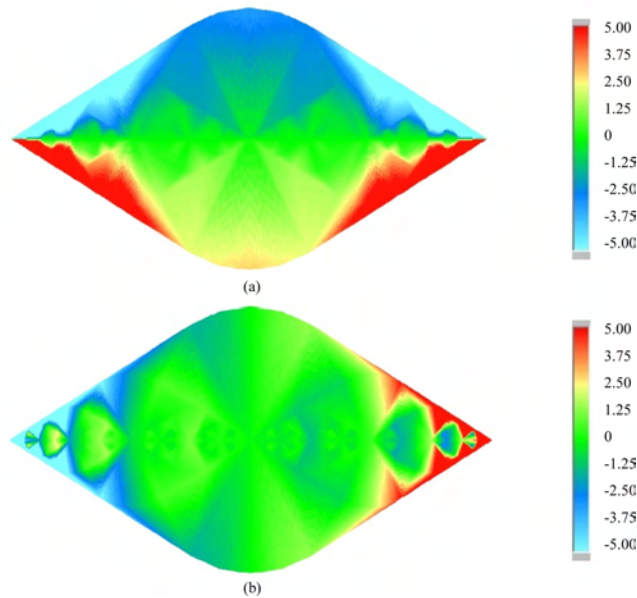


Figure 5.15: LSM bridge with complexities $n = p = q = 5$: (a) T_{11} stresses, (b) T_{12} stresses.

5.5 Discussion

The results of the present chapter highlight that the smooth projection of an unstructured stress function over a structured triangulation is able to generate a convergent discrete notion of the Cauchy stress associated with tensegrity structures in the continuum limit. Such a stress measure can be usefully employed to smoothly predict the stress field associated with tensegrity models of flat and curved membranes [86, 87, 15, 88, 89, 90, 91, 92, 93, 94, 95, 96, 97, 98], and to formulate concurrent discrete-continuum approaches based on the lumped stress method [87, 99, 93, 94, 15]. Due to its ability in generating unstructured and structured force networks over a given design domain, the proposed regularization technique can also be used in association with structural optimization procedures and form-finding methods [93, 94, 115, 116, 117, 118].

Several aspects of the study illustrated in the present chapter pave the

way to relevant further investigations and generalizations that we address to future work. First, the inclusion of body forces calls for specific attention, since network structures are usually loaded by nonzero forces at all nodes. Such a generalization of our current results could be carried out by deriving explicit formulae for the passage from unstructured to structured force networks, which do not require polyhedral stress functions. A second modification of the procedure described in Sect. 5.3 relates to the use of mesh-free interpolation schemes, such as, e.g., the local maximum-entropy approach presented in [108]. Finally, another relevant generalization of the present research regards the prediction of the stress fields associated with fully 3D tensegrity structures. In principle, such a challenging extension might be accomplished by making use of Maxwell or Morera stress functions [132], and applying the present procedures in correspondence with three different planes. However, the application of this approach to the development of provably convergent numerical schemes for 3D stress field remains at present an open question, which we look forward to analyze in future studies.

6

Concluding Remarks and Future Work

6. CONCLUDING REMARKS AND FUTURE WORK

This thesis provides closed form solutions (analytical expressions) and numerical results for minimal mass tensegrity bridge designs. The tensegrity paradigm used for bridges in this paper allows the marriage of composite structures within the design. Our tensegrity approach creates a network of tensile and compressive members distributed throughout the system at many different scales (using tensegrity fractals generates many different scales).

Moreover, the choice of materials for each member of the network can form a system with special electrical, acoustic properties, and/or mechanical properties (stiffness, etc). The mathematical tools of this thesis can be used therefore to design metamaterials and composite materials with unusual and very special properties not available with normal design methods. Analytic and numerical approaches to the parametric design of tensegrity bridges have been respectively presented in Chap. 2 and Chap. 3, obtaining a collection of minimum mass shapes as a function of the adopted design strategy. The numerical results of Chap. 3 confirm the theoretical predictions given in Chap. 2.

Tensegrity bridge structures have been employed as deployable roofs for water canals. The forces, locations, and number of members have been optimized to minimize mass subject to buckling (for bars) and yielding (for cables) constraints for a planar structure with fixed-hinge/fixed-hinge boundary conditions.

The relationship between polyhedral Airy stress function and the stress field associated with tensegrity structures in two dimensions has also been discussed, by generalizing classical results of plane elasticity [126, 125]. Such a relationship allows for determining the continuum limit of the parametric designs presented in Chaps. 2, 3, as the complexity parameters tend to infinity. A two-mesh technique has been proposed for the definition of the Cauchy stress associated with unstructured triangulations corresponding to the topologies of arbitrary tensegrity bridges.

The dynamics of tensegrity bridges will follow as future work to impose further design constraints on stiffness issues (vibrational frequencies, mode

6. CONCLUDING REMARKS AND FUTURE WORK

shapes, displacements for high winds conditions, etc). It is worth noting, however, that the capability all of these choices and adjustments are within the free parameters of the designs in this thesis. The subsequent dynamics approach will evaluate the value (economics and performance tradeoffs) the use of feedback control for the deployable and service functions, or to adjust the stiffness of the structure (varying the prestress of the cables) to modify stiffness or damping after storm damage.

7

Appendix

Multiple connected domains

We examine in the present Appendix the case of a force network defined over a triangulation of a multiple-connected domain. Without loss of generality, we focus our attention on the illustrative example shown in Fig. 7.1, which deals with a doubly-connected domain Ω . The generalization of the arguments presented in Sects. 5.2 and 5.3 to such a domain is pretty straightforward, when Ω is suitably discretized into a collection of simply-connected domains. Fig. 7.2 illustrates a subdivision of the current domain into two simply-connected subdomains Ω_1 and Ω_2 . Let us apply the approximations schemes formulated in Sects. 5.2 and 5.3 to each of such subdomains, on introducing two different stress functions $\hat{\varphi}_h^{(1)}$ and $\hat{\varphi}_h^{(2)}$; two force networks $\hat{\mathbf{P}}_h^{(1)}$ and $\hat{\mathbf{P}}_h^{(2)}$; and two piecewise constant stress fields $\tilde{\mathbf{T}}_h^{(1)}$ and $\tilde{\mathbf{T}}_h^{(2)}$. We obtain an overall approximation of the Airy stress function that is doubly-valued in correspondence with the separation between Ω_1 and Ω_2 . It is easily shown that such an indeterminacy in terms of the Airy stress function does not affect the overall prediction of the Cauchy stress of Ω . As a matter of fact, the stress fields $\tilde{\mathbf{T}}_h^{(1)}$ and $\tilde{\mathbf{T}}_h^{(2)}$ pertain to complementary tessellations Ω_1 and Ω_2 of Ω , which have null intersection and are such that $\Omega = \Omega_1 \cup \Omega_2$ (Fig. 7.2).

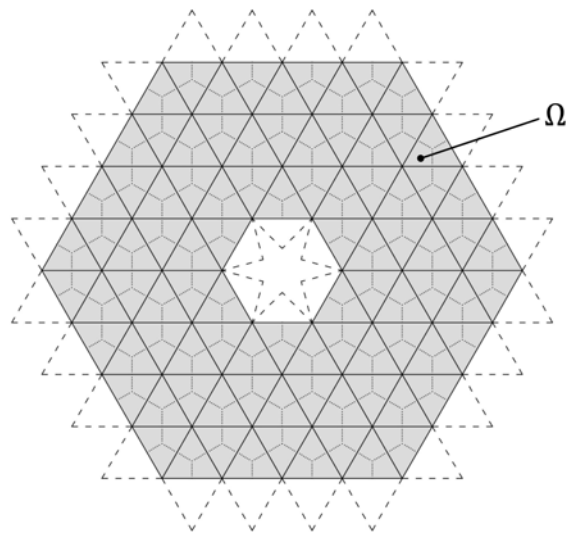


Figure 7.1: Illustration of a doubly-connected domain Ω .

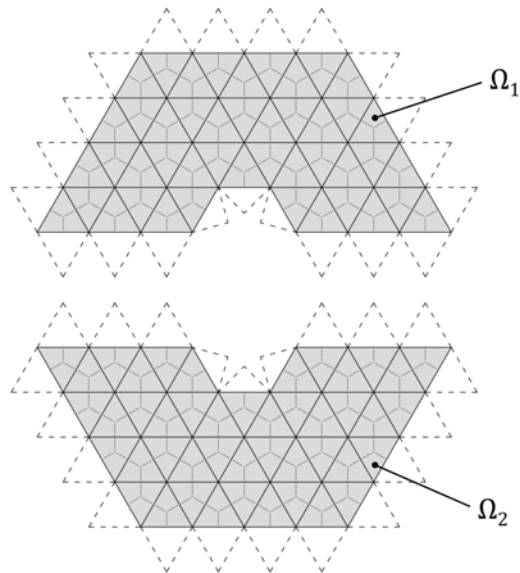


Figure 7.2: Subdivision of a doubly-connected domain Ω into two simply-connected domains Ω_1 and Ω_2 .

Bibliography

Bibliography

- [1] Boeck, J. D., 2013. Tensegrity bridges, Concept design of pedestrian bridges using tensegrity as load carrying system. Delft University of Technology, De Boeck Jan MSc. 19, 65, 67 p.
- [2] Micheletti, A. 2012. Modular tensegrity structures: the TorVergata footbridge, Mechanics, Models and Methods in Civil Engineering, LNACM 61: 375-384.
- [3] Beck, H.; Cooper, J. 2012. Kurilpa Bridge. The Image Publishing Group, Australia. 24 p.
- [4] ARUP. 2010. Kurilpa Bridge, Brisbane. Available from internet: < http://steel.org.au/media/File/Kurilpa_Bridge_case_study.pdf >.
- [5] Briseghella, B. et al., 2010. Tensegrity footbridges with arch deck: static and dynamic behavior. In Proceedings of the ARCH'10 - 6th International Conference on Arch Bridges, 287-294.
- [6] Paradiso, S.; Mucedola, M. 2010. Suspended bridge by Paradiso. Available from internet: < <http://tensegrity.wikispaces.com/Suspended+Bridge+by+Paradiso> >.
- [7] Tyler, T. 2012. Twisting hexagonal bridge. Available from internet: < <http://hexdome.com/bridges> >.

BIBLIOGRAPHY

- [8] T. Iori, S. Poretti, 2014. Storia dell'ingegneria strutturale in Italia. Gangemi Editore, Roma. ISBN: 978-88-492-7830-9.
- [9] Petrangeli, M.P., 1996. Progettazione e costruzione di ponti con cenni di patologia e diagnostica delle opere esistenti, IV edizione, Casa Editrice Ambrosiana, Milano, ISBN: 88-408-1159-1.
- [10] Raithel, A., 1977. Costruzioni di ponti, Liguori Editore, Napoli, ISBN: 88-207-0564-8.
- [11] Rhode-Barbarigos, L., Bel Hadj Ali, N., Motro, R. and Smith, I.F.C., 2010. Designing tensegrity modules for pedestrian bridges, *Engineering Structures*, Vol.32, No.4, pp 1158-1167.
- [12] Baker, W.F., Beghini, L.L., Mazurek, A., Carrion, J., Beghini, A., 2013. Maxwell's reciprocal diagrams and discrete Michell frames. *Struct Multidisc Optim.*, Online first, DOI 10.1007/s00158-013-0910-0.
- [13] Bel Hadj Ali, N., Rhode-Barbarigos, L., Pascual Albi, A. A., Smith, I. F. C., 2010. Design optimization and dynamic analysis of a tensegrity-based footbridge. *Eng. Struct.*, 32(11),3650–3659.
- [14] Bouchittè, G., Gangbo, W., Seppecher, P., 2008. Michell trusses and lines of principal action. *Math. Mod. Meth. Appl. S.*, 18,1571–1603.
- [15] Fraternali, F., Angelillo, M., Fortunato, A., 2002. A lumped stress method for plane elastic problems and the discrete-continuum approximation. *Int. J. Solids Struct.*, 39,6211–6240.
- [16] Fraternali, F., Carpentieri, G., 2013. Continuum limits of 2D force networks associated with discrete systems and tensegrity structures. *In press*.
- [17] Fraternali, F., Marino, A., El Sayed, T., Della Cioppa, A., 2011. On the Structural Shape Optimization through Variational Methods and Evolutionary Algorithms. *Mech. Adv. Mater. Struc.*, 18,224–243.

BIBLIOGRAPHY

- [18] Fraternali, F., Senatore, L., Daraio, C., 2012. Solitary waves on tensegrity lattices. *J. Mech. Phys. Solids*, 60,1137–1144.
- [19] Koohestani, K., 2012. Form-finding of tensegrity structures via genetic algorithm. *Int. J. Solids Struct.*, 49,739–747.
- [20] Michell, A.G.M., 1904. The limits of economy of material in frame-structures. *Philos. Mag.*, 8,589–597.
- [21] Phocas, M.C., Kontovourkis, O., Matheou, M., 2012. Kinetic hybrid structure development and simulation. *Int. J. Archit. Comput.*, 10(1),67–86.
- [22] Rhode-Barbarigos, L., Jain, H., Kripakaran, P., Smith, I. F. C., 2010. Design of tensegrity structures using parametric analysis and stochastic search. *Eng. Comput.*, 26(2),193–203.
- [23] Sakamoto, T., Ferrè, A., Kubo, M. (Eds.), 2008. *From Control to Design: Parametric/Algorithmic Architecture*. Actar.
- [24] Skelton, R. E., 2002. Structural systems: a marriage of structural engineering and system science. *J. Struct. Control*, 9,113–133.
- [25] Skelton, R. E., de Oliveira, M. C., 2010a. Optimal complexity of deployable compressive structures. *J. Franklin I.*, 347,228–256.
- [26] Skelton, R. E., de Oliveira, M. C., 2010b. Optimal tensegrity structures in bending: the discrete Michell truss. *J. Franklin I.*, 347,257–283.
- [27] Skelton, R. E., de Oliveira, M. C., 2010c. *Tensegrity Systems*. Springer.
- [28] Skelton, R. E., Nagase, K., 2012. Tensile tensegrity structures. *Int. J. Space Struct.*, 27,131–137.
- [29] Sokóf, T., Rozvany, G.I.N., 2012. New analytical benchmarks for topology optimization and their implications. Part I: bi-symmetric trusses with two point loads between supports. *Struct Multidisc Optim.*, 46,477–486.

BIBLIOGRAPHY

- [30] Tilbert, A.G., Pellegrino, S., 2011. Review of form-finding methods for tensegrity structures. *Int. J. Space Struct.*, 18,209–223.
- [31] Yamamoto, M., Gan, B. S., Fujita, K., Kurokawa, J., 2011. A genetic algorithm based form-finding for tensegrity structure. *Procedia Engineering*, 14,2949–2956.
- [32] Amendola, A., Fraternali, F., Carpentieri, G., de Oliveira, Skelton, R.E., 2014. Experimental investigation of the softening-stiffening response of tensegrity prisms under compressive loading. E-print, arXiv:1406.1104 [cond-mat.mtrl-sci], 2014.
- [33] Fraternali, F., Carpentieri, G., Amendola, A., 2015. On the mechanical modeling of the extreme softening/stiffening response of axially loaded tensegrity prisms. *JOURNAL OF THE MECHANICS AND PHYSICS OF SOLIDS*, 74, 136-157. ISSN: 0022-5096. DOI: 10.1016/j.jmps.2014.10.010.
- [34] Fraternali, F., Carpentieri, G., Amendola, A., Skelton, R.E., Nesterenko, V. F., 2014. Multiscale tunability of solitary wave dynamics in tensegrity metamaterials. *APPLIED PHYSICS LETTERS*, 105, 201903. ISSN: 0003-6951, DOI: 10.1063:1.4902071.
- [35] Fraternali, F., Farina, I., Polzone, C., Pagliuca, E., Feo, L., 2013. On the use of R-PET strips for the reinforcement of cement mortars. *COMPOSITES. PART B, ENGINEERING*, 46, 207-210. ISSN: 1359-8368, DOI: 10.1016/j.compositesb.2012.09.070.
- [36] Bertoldi, K., Boyce, M. C., 2008. Wave propagation and instabilities in monolithic and periodically structured elastomeric materials undergoing large deformations. *Phys. Rev. B* 78(18), 184107.
- [37] Bigoni, D., Guenneau, S., Movchan, A. B., Brun, M., 2013. Elastic metamaterials with inertial locally resonant structures: Application to lensing and localization. *Phys. Rev. B* 87(174303), 1–6.

BIBLIOGRAPHY

- [38] Brunet, T., Leng, J., Mondain-Monva, O., 2013. Soft acoustic metamaterials. *Science* 342, 323–324.
- [39] Casadei, F., Rimoli, J. J., 2013. Anisotropy-induced broadband stress wave steering in periodic lattices. *Int. J. Solids Struct.* 50(9), 1402–1414.
- [40] Daraio, C., Nesterenko, V. F., Herbold, E., Jin, S., 2006. Energy trapping and shock disintegration in a composite granular medium. *Phys. Rev. Lett.* 96, 058002.
- [41] Daraio, C., Ngo, D., Nesterenko, V.F. and Fraternali, F.. (2010). Highly nonlinear pulse splitting and recombination in a two-dimensional granular network. *Phys. Rev. E.*, 82:036603.
- [42] Daraio, C., Fraternali, F., 2013. Method and Apparatus for Wave Generation and Detection Using Tensegrity Structures. US Patent No. 8,616,328, granted on December 31, 2013.
- [43] Engheta, N., Ziolkowski, R. W., 2006. *Metamaterials: Physics and engineering explorations*. J. Wiley and Sons, Philadelphia.
- [44] Fang, N., Xi, D., Xu, J., Muralidhar, A., Weryut, S., Cheng, S. and Xiang, Z., 2006. Ultrasonic metamaterials with negative modulus. *Nat. Mater.* 5, 452–456.
- [45] Fraternali, F., Porter, M., and Daraio, C., 2010. Optimal design of composite granular protectors. *Mech. Adv. Mat. Struct.* 17, 1–19.
- [46] Fraternali, F., Spadea, S., Ascione, L., 2013. Buckling behavior of curved composite beams with different elastic response in tension and compression. *Compos. Struct.*, 100, 280–289.
- [47] Friesecke, G. and Matthies, K., 2002. Atomic-scale localization of high-energy solitary waves on lattices. *Physica D* 171, 211–220.

BIBLIOGRAPHY

- [48] Gonella, S., Ruzzene, M., 2008. Analysis of In-plane Wave Propagation in Hexagonal and Re-entrant Lattices. *J. Sound Vib.* 312(1-2), 125–139.
- [49] Herbold, E. B. and Nesterenko, V. F., 2012. Propagation of rarefaction pulses in discrete materials with strain-softening behavior. *Phys. Rev. Lett.* 110, 144101.
- [50] Herbold, E. B., Nesterenko, V. F., 2013. Propagation of rarefaction pulses in particulate materials with strain-softening behavior. *AIP Conf. Proc.* 1426, 1447–1450.
- [51] Kadic, M., BÄ¼ckmann, T., Stenger, N., Thiel, M. and Wegener, M., 2012. On the practicability of pentamode mechanical metamaterials. *Appl. Phys. Lett.* 100(19).
- [52] Kashdan, L., Seepersad, C. C., Haberman, M., Wilson, P. S., 2012. Design, fabrication, and evaluation of negative stiffness elements using SLS. *Rapid Prototyping J.* 18(3), 194–200.
- [53] Kochmann, D. M., and Venturini, G. N., 2013. Homogenized mechanical properties of auxetic composite materials in finite-strain elasticity. *Smart mater. Struct.*, 22(8), 084004.
- [54] Kochmann, D. M., 2014. Stable extreme damping in viscoelastic two-phase composites with non-positive-definite phases close to the loss of stability. *Mech. Res. Commun.*, 58, 36–45.
- [55] Lakes, R. S., 1987. Foam Structures with a Negative Poisson’s Ratio. *Science* 235, 1038–1040.
- [56] Lee, H., Zhang, J., Jiang, H., and Fang, N. X., 2012. Prescribed pattern transformation in swelling gel tubes by elastic instability. *Phys. Rev. Lett.*, 108, 214304.

BIBLIOGRAPHY

- [57] Leonard, A. and Fraternali, F. and Daraio, C., 2013. Directional Wave Propagation in a Highly Nonlinear Square Packing of Spheres. *Exp. Mech.* 53(3), 327–337.
- [58] Raney, J.R., Fraternali, F., Daraio, C., 2013. Rate independent dissipation and loading direction effects in compressed carbon nanotube arrays. *NANOTECHNOLOGY*, 24, 255707 (10pp). ISSN: 0957-4484. DOI: 10.1088/0957-4484/24/25/255707.
- [59] Thevamaran, R., Fraternali, F., Daraio, C., 2014. Multi-scale mass-spring model for high-rate compression of vertically aligned carbon nanotube foams. *JOURNAL OF APPLIED MECHANICS*, 81(12), 121006. ISSN:0021-8936, DOI: 10.1115/1.4028785.
- [60] Fraternali, F., Ciancia, V., Checchile, R., Rizzano, G., Feo, L., Incarnato, L., 2011. Experimental Study of the Thermo-Mechanical Properties of Recycled PET Fiber Reinforced Concrete. *COMPOSITE STRUCTURES*, 93, 2368-2374. ISSN: 0263-8223, DOI: 10.1016/j.compstruct.2011.03.025.
- [61] Spadea, S., Farina, I., Berardi, V.P., Dentale, F., Fraternali, F., 2014. Energy dissipation capacity of concretes reinforced with R-PET fibers. *INGEGNERIA SISMICA/INTERNATIONAL JOURNAL OF EARTHQUAKE ENGINEERING*, 2, 61-70, 2014. ISSN: 0393-1420.
- [62] Spadea, S., Farina, I., Carrafiello, A, Fraternali, F., 2014. On the use of recycled nylon fibers as cement mortar reinforcement. *CONSTRUCTION AND BUILDING MATERIALS*, In press, 2014. E-print: arXiv:1409.7258 [cond-mat.mtrl-sci]
- [63] Li, J., Chan, C. T., 2004. Double-negative acoustic metamaterial. *Phys. Rev. E* 70 (5 2), 055602-1–055602-4.
- [64] Liu, Q., 2006. Literature Review: Materials with Negative Poisson’s Ratios and Potential Applications to Aerospace and Defence. DTIC Docu-

BIBLIOGRAPHY

- ment. No. DSTO-GD-0472. Defence science and technology organization Victoria (Australia) Air Vehicles DIV.
- [65] Liu, Z., Zhang, X., Mao, Y., Zhu, Y. Y., Yang, Z., Chan, C. T., Sheng, P., 2000. Locally Resonant Sonic Materials. *Science* 289(5485), 1734–1736.
- [66] Lu, M.H., Feng, L., Chen, Y.F., 2009. Phononic Crystals and Acoustic Metamaterials. *Mater. Today* 12(12), 34–42.
- [67] Manktelow, K.L., Leamy, M.J., and Ruzzene, M., 2013. Topology design and optimization of nonlinear periodic materials. *J. Mech. Phys. Solids* 61(12), 2433–2453.
- [68] Milton, G. W., 1992. Composite materials with Poisson’s ratios close to -1. *J. Mech. Phys. Solids* 40(5), 1105–1137.
- [69] Milton, G. W., 2002. *The theory of composites*. Cambridge University Press, Salt Lake City.
- [70] Milton, G. W., 2013. Adaptable nonlinear bimode metamaterials using rigid bars, pivots, and actuators. *J. Mech. Phys. Solids* 61, 1561–1568.
- [71] Milton, G. W. and Cherkaev, A. V., 1995. Which Elasticity Tensors are Realizable? *J. Eng. Mater. Technol.* 117(4), 483–493.
- [72] Nesterenko, V.F., 2001. *Dynamics of Heterogeneous Materials*. Springer, New York.
- [73] Ngo, D. and Fraternali, F. and Daraio, C. (2012). Highly nonlinear solitary wave propagation in Y-shaped granular crystals with variable branch angles. *Phys. Rev. E.*, 85:036602.
- [74] Nicolaou, Z. G., Motter, A. E., 2012. Mechanical metamaterials with negative compressibility transitions. *Nat. Mater.* 11, 608–613.
- [75] Oppenheim, I. and Williams, W., 2000. Geometric effects in an elastic tensegrity structure. *J. Elast.* 59, 51–65.

BIBLIOGRAPHY

- [76] Porter, M.A., Daraio, C., Szelengowicz, I., Herbold, E.B., Kevrekidis, P.G., 2009. Highly nonlinear solitary waves in heterogeneous periodic granular media. *Physica D* 238, 666–676.
- [77] Riks, E., 1984. Some computational aspects of the stability analysis of non-linear structures. *Int. J. Solids Struct.*, 47, 219–259.
- [78] Ruzzene, M., Scarpa, F., 2005. Directional and band gap behavior of periodic auxetic lattices. *Phys. Status Solidi B* 242(3), 665–680.
- [79] Spadoni, A. and Daraio, C., 2010. Generation and control of sound bullets with a nonlinear acoustic lens. *Proc. Natl. Acad. Sci. U.S.A.* 107(16), 7230–7234.
- [80] Spadoni, A., Ruzzene, M., 2012. Elasto-static micropolar behavior of a chiral auxetic lattice. *J. Mech. Phys. Solids* 60, 156–171.
- [81] Wang, P., Shim, J., Bertoldi, K., 2013. Effects of geometric and material nonlinearities on tunable band gaps and low-frequency directionality of phononic crystals. *Phys. Rev. B* 88(014304), 1-15.
- [82] Wriggers, P., Simo, J.C., 1990. A general procedure for the direct computation of turning and bifurcation points. *Int. J. Numer. Meth. Eng.*, 30, 155–176.
- [83] Zhang, S., Yin, L., Fang, N., 2000. Focusing Ultrasound with an Acoustic Metamaterial Network. *Phys. Rev. Lett.* 102(194301), 1–4.
- [84] Zhang, S., 2010. Acoustic metamaterial design and application. Ph.D. dissertation, University of Illinois at Urbana-Champaign, http://web.mit.edu/nanophotonics/projects/Dissertation_Shui.pdf.
- [85] Zheng, X., Deotte, J., Alonso, M. P., Farquar, G. R., Weisgraber, T. H., Gemberling, S., Lee, H., Fang, N., and Spadaccini, C. M., 2012.

BIBLIOGRAPHY

- Design and optimization of a light-emitting diode projection micro-stereolithography three-dimensional manufacturing system. *Rev. Sci. Instrum.*, 83, 125001.
- [86] O'Dwyer, D., Funicular analysis of masonry vaults, *Comput Struct*, 1999, 73, 187–197.
- [87] Fraternali, F., Complementary energy variational approach for plane elastic problems with singularities, *Theor. Appl. Fract. Mech.*, 2001, 35, 129–135
- [88] Davini, C., and Paroni, R., Generalized hessian and external approximations in variational problems of second order, *J. Elast.*, 2003, 70, 149–174.
- [89] Kilian, A. and Ochsendorf, J., Particle-spring systems for structural form finding, *IASS J.*, 2005, 46(2), 77–85
- [90] Block, P. and Ochsendorf, J., Thrust Network Analysis: A new methodology for three-dimensional equilibrium, *IASS J.*, 2007, 48(3), 167–173.
- [91] Block, P., Thrust Network Analysis: Exploring Three-dimensional equilibrium, *Ph.D. dissertation, Massachusetts Institute of Technology, Cambridge, USA*, 2009.
- [92] Micheletti, A., On generalized reciprocal diagrams for internally self-equilibrated frameworks, *Int. J. Space Struct.*, 2008, 23, 153–166.
- [93] Fraternali, F., A thrust network approach to the equilibrium problem of unreinforced masonry vaults via polyhedral stress functions, *Mech. Res. Commun.*, 2010, 37, 198–204.
- [94] Fraternali, F., A mixed lumped stress–displacement approach to the elastic problem of masonry walls. *Mech. Res. Commun.*, 2011, 38, 176–180
- [95] Block, P., and Lachauero, L., Closest-fit, compression-only solutions for free form shells, In: *IABSE/IASS London Symposium, Int. Assoc. Shell Spatial Structures*, 2011.

BIBLIOGRAPHY

- [96] Angelillo, M., Babilio, E., and Fortunato, A., Singular stress fields for masonry-like vaults, *Continuum Mech. Therm.*, 2012, 25, 423-441.
- [97] Desbrun, M., Donaldson, R., and Owhadi, H., Modeling across scales: Discrete geometric structures in homogenization and inverse homogenization, In: Multiscale analysis and nonlinear dynamics: from genes to the brain, Pesenson, M.Z., Ed., Vol. 8 of *Reviews of Nonlinear Dynamics and Complexity*. Wiley, 2013.
- [98] De Goes, F., Alliez, P., Owhadi, H. and Desbrun, M., On the equilibrium of simplicial masonry structures, *ACM Transactions on Graphics*, 2013, 32(4), 93.
- [99] Fraternali, F., Error estimates for a lumped stress method for plane elastic problems, *Mech. Adv. Matl. Struct.*, 2007, 14(4), 309–320.
- [100] Giaquinta, M., and Giusti, E., Researches on the equilibrium of masonry structures, *Arch. Ration. Mech. An.*, 1985, 88, 359–392.
- [101] Mansfield, E.H., The Bending and Stretching of Plates, *Pergamon Press*, 1964.
- [102] Miller, R. E., and Tadmor, E. B., A unified framework and performance benchmark of fourteen multiscale atomistic/continuum coupling methods, *J. Model. Simul. Mater. Sc.*, 2009, 17, 053001.
- [103] Liu, B., Huang, Y., Jiang, H., Qu, S., and Hwang, K. C., The atomic-scale finite element method, *Comput. Methods Appl. Mech. Engrg.*, 2004, 193:1849–1864.
- [104] Tu, Z.C., and Ou-Yang Z.C., Elastic theory of low-dimensional continua and its application in bio- and nano-structures, *J. Comput. Theor. Nanosci.*, 2008, 5, 422–448.

BIBLIOGRAPHY

- [105] Fraternali, F., Blesgen, M., Amendola, A., and Daraio, C., Multiscale mass-spring models of carbon nanotube foams, *J. Mech. Phys. Solids*, 2010, 59(1), 89–102.
- [106] Raney, J.R., Fraternali, F., Amendola, A., and Daraio, C., Modeling and in situ identification of material parameters for layered structures based on carbon nanotube arrays, *Compos. Struct.*, 2011, 93, 3013–3018.
- [107] Blesgen, T., Fraternali, F., Raney, J.R., Amendola, A., and Daraio, C., Continuum limits of bistable spring models of carbon nanotube arrays accounting for material damage, *Mech. Res. Commun.*, 2012, 45, 58–63.
- [108] Fraternali, F., Lorenz, C., and Marcelli, G., On the estimation of the curvatures and bending rigidity of membrane networks via a local maximum-entropy approach, *J. Comput. Phys.*, 2012, 231, 528–540.
- [109] Schmidt, B., and Fraternali, F., Universal formulae for the limiting elastic energy of membrane networks, *J. Mech. Phys. Solids*, 2012, 60, 172–180.
- [110] Fraternali, F., and Marcelli, G., A multiscale approach to the elastic moduli of biomembrane networks, *Biomech Model Mechanobiol*, 2012, 11, 1097–1108.
- [111] Skelton, R.E., Structural systems: a marriage of structural engineering and system science, *J. Struct. Control*, 2002, 9, 113–133.
- [112] Vera, C., Skelton, R.E., Bossens, F., Sung, L.A., 3-D nanomechanics of an erythrocyte junctional complex in equibiaxial and anisotropic deformations, *Ann. Biomed. Eng.*, 2005, 33(10), 1387–1404.
- [113] Mofrad, M.R.K., and Kamm, R.D., (Eds.), Cytoskeletal Mechanics: Models and Measurements, *Cambridge University Press*, 2006.
- [114] Fraternali, F., Senatore, L., and Daraio, C., Solitary waves on tensegrity lattices, *J. Mech. Phys. Solids*, 2012, 60, 1137–1144.

BIBLIOGRAPHY

- [115] Linhard, J., and Bletzinger, K.-U., "Tracing" the Equilibrium – Recent Advances in Numerical Form Finding, *International Journal of Space Structures*, 2010, 25(2), 107–116.
- [116] Ohmori, H., Computational Morphogenesis: Its Current State and Possibility for the Future, *International Journal of Space Structures*, 2011, 26(3), 269–276.
- [117] Wang, H., and Ohmori, H., Truss optimization using genetic algorithm, considering construction process, *International Journal of Space Structures*, 2010, 25(4), 202–215.
- [118] Baldassini, N., Pottmann, H., Raynaud, J., and Schiftner, A., New strategies and developments in transparent free-form design: From faceted to nearly smooth envelopes, *International Journal of Space Structures*, 2010, 25(3), 185–197.
- [119] Schlaich, J., Schäfer, K., and Jennewein, M., Toward a Consistent Design of Structural Concrete. *Journal of Prestressed Concrete Institute (PCIJ)*, 1987, 32, 74–150.
- [120] Shen, S. and Atluri, S.N., Atomic-level stress calculation and continuum-molecular system equivalence, *CMES - Comp Model. Eng.*, 2004, 6, 91–104.
- [121] Admal, N. C., and Tadmor, E. B., A unified interpretation of stress in molecular systems, *J. Elast.*, 2010, 100, 63–143
- [122] Glowinski, R., *Approximations Externes, par Elements Finis de Lagrange d'Ordre Un en Deux, du Problème de Dirichlet pour l'Opérateur Biharmonique. Methodes Iteratives de Resolution des Problemes Approches*, In: Miller, J.J.H. (Ed.), Topics in Numerical Analysis. Academic Press, 123–171, 1973.

BIBLIOGRAPHY

- [123] De Guzmán, M., and Orden, D., From graphs to tensegrity structures: Geometric and symbolic approaches, *Publ. Mat*, 2006, 50, 279–299.
- [124] Strang, G., *Introduction to Linear Algebra*, 4th Edition, Cambridge University Press, 2009.
- [125] Gurtin, M. E., *The Linear Theory of Elasticity*, In Handbuch der Physik (Encyclopedia of Physics). VIa/2, Springer-Verlag, 1–295, 1972.
- [126] Green, A., and Zerna, W., *Theoretical Elasticity*, Dover, 2002.
- [127] Fraternali, F., Farina, I., and Carpentieri, G., A discrete-to-continuum approach to the curvature of membrane networks and parametric surfaces, *Mech. Res. Commun.*, *in press*, 2013.
- [128] Cyron, C.J., Arrojó, M., and Ortiz, M., Smooth, second-order, non-negative meshfree approximants selected by maximum entropy, *Int. J. Num. Meth. Eng.*, 2009, 79, 1605–1632.
- [129] Akima, H., and Ortiz, M., Algorithm 526: Bivariate Interpolation and Smooth Surface Fitting for Irregularly Distributed Data Points [E1], *ACM T. Math. Software*, 1978, 4, 160–176.
- [130] Baratta, A., and Corbi, O., On the equilibrium and admissibility coupling in NT vaults of general shape, *Int. J. Solids Struct.*, 2010, 47, 2276–2284.
- [131] Hegemier, G.A., and Prager, W. On Michell trusses, *Int. J. Mech. Sci.*, 1969, 11, 209–215.
- [132] Sadd, M. H., 2005. *Elasticity: Theory, Applications, and Numerics*, Elsevier.
- [133] Alzoubi, H.H., Al-Zoubi, A.H., 2010 Baker, W.F., Beghini, L.L., Mazurek, A., Carrion, J., Beghini, A., 2013. Assessment of building façade

BIBLIOGRAPHY

- performance in terms of daylighting and the associated energy consumption in architectural spaces: Vertical and horizontal shading devices for southern exposure facades. *Energ. Convers. Manage.*, 51, 1592–1599.
- [134] Alzoubi, H.H., Al-Zoubi, A.H., 2010 Baker, W.F., Beghini, L.L., Mazurek, A., Carrion, J., Beghini, A., 2013. Responsive shading |Intelligent façade systems. In: *ACADIA 2010 life in:formation*, Proceedings of the 30th annual conference of the Association for Computer Aided Design in Architecture, New York, N.Y. ; *ACADIA*, 263–269.
- [135] Carpentieri, G., Skelton, R.E., 2014. On the Minimum Mass and Optimal Complexity of Planar Tensegrity Bridges. Internal Report of the University of California, San Diego, Mechanical and Aerospace Engineering, No. 1-2014. available at url: gcarpentieri.altervista.org (last accessed: Nov. 11, 2014).
- [136] Carpentieri, G., Skelton, R.E., Fraternali, F., 2014. Minimum mass and optimal complexity of planar tensegrity bridges. *THE SCIENTIFIC WORLD JOURNAL*, In press.
- [137] Carpentieri, G., Skelton, R.E., Fraternali, F., 2014. Parametric design of minimal mass tensegrity bridges under yielding and buckling constraints. In press, 2014. Eprint: [arXiv:1411.7966](https://arxiv.org/abs/1411.7966) [cond-mat.mtrl-sci]. DOI: 10.13140/2.1.3224.2248.
- [138] European Commission, 2014. HORIZON 2020 Work Programme 2014-2015, PART 5.ii, Leadership in Enabling and Industrial Technologies: Nanotechnologies, Advanced Materials, Biotechnology and Advanced Manufacturing and Processing. <http://ec.europa.eu/>, 93–103.
- [139] Kuhn, T.E., Herkel, S., Henning, H.-M., 2010 Active solar facades (PV and solar thermal). In: *PALENC 2010*, Proceedings of the 3rd International Conference on Passive & Low Energy Cooling for the Built Environment, <http://publica.fraunhofer.de/documentsN-161087.html>.

BIBLIOGRAPHY

- [140] Lombard, L.P., Ortiz, J., Pout, C., 2010. A review on buildings energy consumption information. *Energ. Buildings*, 40,394–398.
- [141] Skelton, R. E., Fraternali, F., Carpentieri, G., Micheletti, A., 2014. Minimum mass design of tensegrity bridges with parametric architecture and multiscale complexity. *Mechanics Research Communications*, 58, 124–132, ISSN 0093-6413, doi: 10.1016/j.mechrescom.2013.10.017.
- [142] Kahn, M., Longcore, T., 2014. A Feasibility Analysis of Installing Solar Photovoltaic Panels Over California Water Canals. UCLA Institute of the Environment and Sustainability, Los Angeles, CA.
- [143] [<http://motherboard.vice.com/read/indias-ingenious-plan-to-cover-1000-miles-of-canals-with-solar-power-plants>], [accessed: 22.07.2014].
- [144] Gere, J. M., Timoshenko, S.P., 1997 *Mechanics of Materials*, PWS Publishing Company.
- [145] Nagase, K., Skelton, R. E., 2014. Minimal mass tensegrity structures. *Journal of the International Association for Shell and Spatial Structures*, 55(1), 37–48.
- [146] Fraternali, F., Spadea, S., Berardi, V.P., 2014. Effects of recycled PET fibers on the mechanical properties and seawater curing of Portland cement-based concretes. *CONSTRUCTION AND BUILDING MATERIALS*, 61, 293-302. ISSN: 0950-0618, DOI: 10.1016/j.conbuildmat.2014.03.019.
- [147] Fraternali, F., Carpentieri, G., 2014. On the correspondence between 2D force networks and polyhedral stress functions. *INTERNATIONAL JOURNAL OF SPACE STRUCTURES*, 29(3), 145-159. ISSN 0266-3511.